Doctoral theses at NTNU, 2022:159

Ellen Synnøve Skilbred

Corrosion, hydrogen uptake and environmentally assisted cracking of flexible pipe steel armour wires

Doctoral thesis

NTNU
Norwegian University of Science and Technology
Thesis for the Degree of Philosophiae Doctor
Faculty of Engineering
Department of Mechanical and Industrial Engineering

NTNU
Norwegian University of Science and Technology

Ellen Synnøve Skilbred

Corrosion, hydrogen uptake and environmentally assisted cracking of flexible pipe steel armour wires

Thesis for the Degree of Philosophiae Doctor

Trondheim, May 2022

Norwegian University of Science and Technology
Faculty of Engineering
Department of Mechanical and Industrial Engineering

NTNU
Norwegian University of
Science and Technology

NTNU
Norwegian University of Science and Technology

Thesis for the Degree of Philosophiae Doctor

Faculty of Engineering
Department of Mechanical and Industrial Engineering

ISBN 978-82-326-6609-6 (printed ver.)
ISBN 978-82-326-6279-1 (electronic ver.)
ISSN 1503-8181 (printed ver.)
ISSN 2703-8084 (online ver.)

Doctoral theses at NTNU, 2022:159

Printed by NTNU Grafisk senter

Preface

This thesis describes the work conducted to fulfil the requirements for the degree of Philosophiae Doctor (Ph.D) at The Norwegian University of Science and Technology (NTNU). The research was mainly conducted at The Department of Mechanical and Industrial Engineering at NTNU from October 2018 to December 2021. Experiments were also conducted at The Institute for Energy Technology (IFE) where the candidate worked for three weeks in June and August 2020. Professor Roy Johnsen was the main supervisor and Dr. Arne Dugstad was co-supervisor.

The work was part of the project "Environmental Cracking of Flexible Pipe Armour Wires", Research Council of Norway project no. 280760 within the PETROMAKS 2 program. The project participants were The Research Council of Norway, Equinor, Shell, Chevron, Petrobras, OKEA, TechnipFMC, NOV, Baker Hughes and 4Subsea.

Abstract

Flexible pipes are widely used in oil and gas applications. They consist of several metallic and polymeric layers, including a layer of tensile armour wires made from high-strength carbon steels. The armour wires are closely packed and the environment in the annulus contains gases that have permeated from the bore such as CO_2, CH_4, H_2S and H_2O. This creates a corrosive environment in the flexible pipes, but the large surface area of steel compared to the free volume of the annulus promotes formation of protective films of iron carbonate or sulphides. Corrosion may however cause damage if there are actively corroding areas in the steels or if the annulus is flooded with seawater due to outer sheath damage. The retrieval of damaged pipes have shown features consistent with hydrogen damage, and hydrogen embrittlement is therefore considered a possible failure mechanism, either by cathodic polarization from a corrosion protection system when the outer sheath is breached, or from hydrogen produced in the corrosion processes.

In this PhD project the environmentally assisted cracking of tensile steel armour wires was investigated by measuring hydrogen uptake in six flexible pipe steel armour wires with different microstructures in simulated environments and by mechanical tests on smooth and notched samples exposed to air and simulated environments. The wires were characterized to link the hydrogen uptakes and effect of hydrogen on mechanical properties to microstructural properties. The wires had pearlitic-ferritic microstructures with carbon contents from 0.28 to 0.83 wt% and were plastically deformed to different degrees. Two of the materials with higher carbon contents had almost completely pearlitic microstructures, with lamellar pearlite, while the other materials had globular or partly globular carbides. The shape and distribution of carbide affects the tortuosity of the hydrogen diffusion path, and a tortuosity factor was estimated to distinguish this effect on the effective diffusion coefficients from the effect of hydrogen trapping on the effective diffusion coefficients. The interface between cementite and ferrite is a well-known hydrogen trap, and to investigate whether this is a significant factor on the hydrogen uptake and diffusion, the interfacial area between ferrite and cementite was also estimated for each material.

Electrochemical permeation tests were conducted under cathodic polarization to -12 mA cm^{-2} while exposed to deaerated NaOH. The permeability to hydrogen was highest for the materials with finest grain size and lowest for the materials with largest grains, which is an indication of enhanced permeability of hydrogen on grain boundaries. The diffusion coefficients showed a tendency to decrease with the increase of ferrite-cementite interfacial area, thus confirming the occurence of trapping on the ferrite-cementite interfaces. The overall uptake of hydrogen in lattice and reversible traps was calculated

using the permeation flux of hydrogen and the diffusion coefficients, but the hydrogen uptakes did not show a strong correlation with the grain size nor ferrite-cementite interfacial area. A clear difference in hydrogen uptake was observed between the two less deformed materials compared to the materials with a more deformed microstructure.

Electrochemical permeation tests were also conducted in a simulated flexible pipe annulus environment, where the wire materials were exposed to artificial seawater with H_2S and CO_2 on the hydrogen entry side of the permeation cell. The hydrogen permeability did not increase with finer grain size in these conditions. Protective film formation was prevented by continuous pumping of electrolyte in and out of the corrosion compartment, which kept the iron content low ($<$ 10 ppmw). Ferrite dissolved preferentially, leaving retained carbides on the surface. As the retained carbide area increased, the corrosion rates increased while the hydrogen uptake decreased. The proposed mechanism for the decreasing hydrogen uptakes with increasing carbide area is that the hydrogen adsorbed far from ferrite will be prevented from absorbing in ferrite due to the low solubility and diffusivity of hydrogen in cementite. The material with the lowest carbon content and very fine carbide distribution had relatively stable corrosion rate and relatively high hydrogen uptake. For the other materials, the rank of hydrogen uptake followed the rank in corrosion rate and carbon contents. Whether the hydrogen uptakes were directly increasing with the carbon contents or the corrosion rates could not be concluded.

Tensile tests were conducted for both smooth and notched samples in air and in 3.5% NaCl while polarised to -1.4 V vs. Ag/AgCl, sat. KCl. The samples had increasing susceptibility to hydrogen embrittlement with increasing carbon content, but the notched samples showed a particular increase in hydrogen embrittlement susceptibility for the lamellar materials. It was seen that the presence of hydrogen lead to more crack initiation points, when comparing the fracture surfaces of samples tested under cathodic polarisation to samples tested in air. For the notched samples, the maximum load and crack-tip opening displacement at maximum load decreased for most of the materials when exposed to cathodic polarisation compared to testing in air. The material with lowest carbon content and highest ductility did not have significantly reduced properties in the hydrogen charged environment.

Acknowledgements

This work could not have been done without the help and support of supervisors, co-workers, friends and family.

First of all, I would like to thank Professor Roy Johnsen for granting me this Ph.D. position and providing support on both a scientific and motivational level. Your optimism, trust and ability to find good solutions for all situations were essential for my motivation and progress. I would also like to thank my co-supervisor Arne Dugstad for many good discussions and important insights to corrosion and flexible pipes. I thank Simona Palencsár for great support and collaboration, especially with the hydrogen permeation experiments conducted at IFE and writing of journal paper on that work. I would like to thank everyone at IFE who took well care of me during my two short stays, and who joined in on several of our internal NTNU and IFE meetings.

I would like to thank all my co-authors. Mariano Kappes and Mariano Iannzzi were crucial for the interpretation of hydrogen permeation tests and my development in writing scientific papers. Thank you for your thorough revisions and explanations, and for your patience. I would like to thank Antonio Alvaro, Luigi Viespoli and Aleksander Omholt Myhre for collaboration on the experiments and journal paper with tensile tests of notched samples. I have learned so much about fracture mechanics from you. My first insight to the materials of this work was during the master of Signe Aarthun Lootz, who conducted several tests and provided a useful guide to the world of flexible pipes through her master thesis. I appreciate all the hard work you did.

This work involved many experiments and many people supported me by teaching me how to use equipment and helping me when things went wrong. I would like to thank Cristian Torres Rodriguez, Seyed Mohammad Javad Razavi, Øyvind Haave, Børge Holen, Ann-Karin Kvernbråten, Hans Husby and Mats Ingdal. I thank Shabnam Karimi for measuring hydrogen uptakes with TDS for conditions similar to the tensile tests.

I would like to thank my friends and family, who have been enthusiastic supporters through my studies and my time as a PhD candidate. I would like to thank all my close colleagues at NTNU for all the good moments we shared. Finally, I would like to thank my partner, Jake Lamb, for your support through these years.

Contents

Preface i

Abstract iii

Acknowledgements v

List of Figures ix

List of Tables xi

Nomenclature xiii

1 Introduction 1
- 1.1 Background . . . 1
- 1.2 Objectives and scope . . . 3
- 1.3 Thesis overview . . . 4

2 Corrosion in aqueous CO_2 and H_2S environment 7
- 2.1 CO_2 corrosion in aqueous environments . . . 7
  - 2.1.1 Corrosion mechanism . . . 7
  - 2.1.2 Effect of microstructure . . . 9
- 2.2 H_2S corrosion in aqueous environments . . . 11
- 2.3 Corrosion in aqueous environments with both H_2S and CO_2 . . . 12

3 Environmentally assisted cracking 15
- 3.1 Hydrogen damage mechanisms . . . 16
- 3.2 Hydrogen embrittlement of steels . . . 17
  - 3.2.1 Hydrogen entry from aqueous solutions . . . 17
  - 3.2.2 HE mechanisms . . . 18
  - 3.2.3 Hydrogen solubility in lattice . . . 20
  - 3.2.4 Trapping of hydrogen . . . 21
  - 3.2.5 Hydrogen diffusion . . . 22
- 3.3 Hydrogen uptake from CO_2 and H_2S corrosion . . . 24

4 Materials and characterization 27
- 4.1 Phase morphology and grain size . . . 27
- 4.2 Chemical composition . . . 29

4.2.1 Sample preparation . . . 29
4.2.2 Calibration . . . 30
4.2.3 Results . . . 30
4.3 Mechanical properties . . . 31
4.4 Metallographic study of phases . . . 31

5 Experimental methods **35**
5.1 Electrochemical hydrogen permeation test . . . 35
5.1.1 Embedding samples . . . 37
5.1.2 Hydrogen uptake in corrosive environment . . . 39
5.2 Macro-scale slow strain rate tensile test . . . 42

6 Summary of papers **47**
6.1 Paper I . . . 47
6.2 Paper II . . . 48
6.3 Paper III . . . 49
6.4 Paper IV . . . 51

7 Conclusions and further work **53**
7.1 Conclusions . . . 53
7.2 Further Work . . . 55

Bibliography **57**

Appended papers **69**
Paper I . . . 71
Paper II . . . 93
Paper III . . . 109
Paper IV . . . 137

List of Figures

1.1 Structure of a flexible pipe. 1
1.2 Damaged flexible pipe. 2
1.3 Damaged flexible pipe armour wires. 3

2.1 Iron carbonate and retained carbides formed by CO_2 corrosion of a ferritic-pearlitic steel. 9

3.1 Hydrogen damage mechanisms illustrated. 17
3.2 HELP mechanism illustrated. 19
3.3 HEDE mechanism illustrated. 19
3.4 Permeation transients of Armco iron in specific cold deformed conditions (0-70%). 23
3.5 Permeation transients for an iron carbonate enriched surface, an iron carbide enriched surface and a wet-ground surface of the same material. . 25
3.6 Permeation transients for an API X65 carbon steel with and without iron carbonate scales on the surface. The transients were measured in a H_2SO_4 containing solution under cathodic charging to -8 mA cm^{-2}. 26

4.1 SEM images of the wire materials. 28
4.2 Carbon contents in decarburized layers of the six materials A-F. 31
4.3 Cementite intercepts per length test line. 33
4.4 Example of line drawn to estimate the tortuosity of the hydrogen diffusion path. 33

5.1 Sketch of the electrochemical hydrogen permeation test cell. 36
5.2 Example of rising and decay hydrogen permeation transients. 37
5.3 Pd-coated and embedded permeation test sample. 38
5.4 Sketch of the electrochemical hydrogen permeation tests used in Paper II. 40
5.5 Effect of stabilisation time on hydrogen permeation results, illustrated by two permeation curves with different stabilization times for the same material. 41
5.6 Electrochemical hydrogen permeation tests with and without short stops in the gas supply (Material E). 42
5.7 Sketch and photograph of a notched sample installed in the tensile rig with the environmental chamber attached. 43
5.8 Image of crack from a tensile test. The crack mouth opening and crack tip opening are indicated by the arrows. 44

5.9 Reduction of ductility in ASTM G129 and NACE TM0198. 45

List of Tables

2.1 Properties of iron sulphide compounds. 12

4.1 Cementite morphology and extent of deformation in the wire materials. . 27
4.2 Grain size of the wire materials. 28
4.3 Particle size of grinding papers. 29
4.4 Composition of wire materials used in the Ph.D. work based on GD-OES measurements. 30
4.5 Mechanical properties of the wire materials. 31
4.6 Metallographic study of the six wire materials. 33

Nomenclature

λ_p	Mean free path between cementite particles
σ_0	Mean true spacing for lamellar materials
τ	Tortuosity of the hydrogen diffusion path
$a_{CO_3^{2-}}$	Activity of carbonate ions
$a_{Fe^{2+}}$	Activity of iron ions
c_i	Specie concentration
C_o	Hydrogen solubility
D	The hydrogen diffusion coefficient
D_{eff}	Effective diffusion coefficient
D_L	Lattice diffusion coefficient
f	Volume fraction of cementite
I	Ionic strength
J	Hydrogen permeation flux
K	Threshold stress intensity
$K_{\text{sp,FeCO}_3}$	Solubility product of $FeCO_3$
K_I	Plane strain threshold stress intensity
L	Length of the diffusion path between two parallel planes
L_0	Distance between two parallel planes
N	The number of cementite intercepts per test line
n	Number of cementite platelets intersected per unit length
N_p	Number of particles intercepted by a test line
P	H_2 gas fugacity at the metal/electrolyte interface

Q	Hydrogen diffusion activation energy
R	Gas constant
S_v	Ferrite-cementite interfacial area
S_{FeCO_3}	Saturation ratio of $FeCO_3$
T	Absolute temperature
V^*	Molar partial volume of hydrogen
z_i	Specie charge
AIDE	Adsorption-induced dislocation emission
bcc	Body centered cubic
CE	Counter electrode
CF	Corrosion fatigue
CMOD	Crack mouth opening displacement
CTOD	Crack tip opening displacement
DIC	Digital image correlation
EAC	Environmentally assisted cracking
Ep	Plastic strain-to-failure
GD-OES	Glow-discharge optical emission spectroscopy
HAC	Hydrogen-assisted cracking
HE	Hydrogen embrittlement
HEDE	Hydrogen enhanced decohesion
HELP	Hydrogen enhanced localized plasticity
HESIV	Hydrogen enhanced strain-induced vacancies
HIC	Hydrogen induced cracking
HSC	Hydrogen stress cracking
HV_{10}	Vickers hardness measurement with 10 kgf load
LME	Liquid metal embrittlement

LPR	Linear polarisation resistance
NTS	Notch tensile strength
OCP	Open circuit potential
REF	Reference electrode
RNTS	Notch tensile strength ratio
SCC	Stress corrosion cracking
SEM	Scanning electron microscopy
SOHIC	Stress oriented hydrogen induced cracking
SSC	Sulphide stress cracking
SWC	Stepwise cracking
UTS	Ultimate tensile strength
WE	Working electrode
XRD	X-ray diffraction
YS	Yield strength

1 Introduction

1.1 Background

Flexible pipes are used both as risers and flow lines in oil and gas production. In 2016, there were more than 3500 dynamic un-bonded flexible risers in operation worldwide with design service lives of 15-20 years and an average age of 10 years [1]. A flexible pipe consists of several polymer and metallic layers, as shown in Figure 1.1. The layer structure is determined according to the specific conditions that are expected to arise during the pipe's lifetime. Most flexible pipes consist of the following layers [2, 3].

- **Carcass:** The innermost layer is made of a corrosion resistant alloy with interlocked parts. It protects the pipe from external crushing.
- **Polymer sheath:** This polymer is placed outside the carcass to limit the transport of chemical components from the bore to the outer layers.
- **Pressure armour:** This layer is applied to resist internal pressure, but can be excluded when the tensile armour wires are wound at a 55° angle [1].
- **Tensile armour:** High-strength carbon steel wires wound at a 25-55° angle to the longitudinal direction [4]. The armour consists of two layers wound in opposite directions. Anti-wear tape is often placed in between layers.
- **Outer polymer sheath:** The outer layer is a polymer sheath that protects the pipe from the corrosive seawater outside.

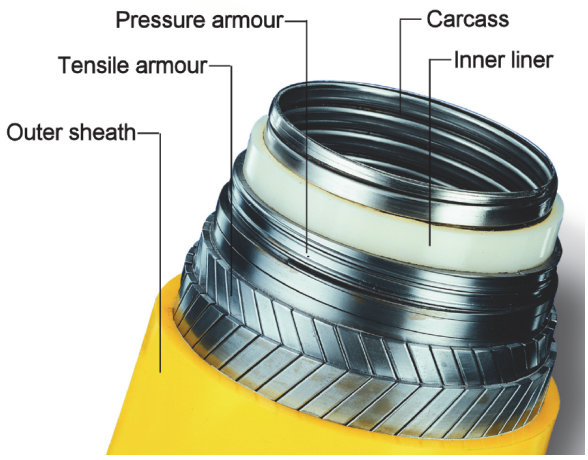

Figure 1.1: Structure of a flexible pipe. Figure from [3].

This work focuses on the tensile armour wires. In deep-water applications the tensile armour must withstand both static and dynamic loading with high alternating stresses [5], and the yield strength of the tensile armour is typically in the range of 700 to 1400 MPa [1]. The environment in the annulus, where the tensile armour wires are positioned, is confined and rich in dissolved species. The free volume to steel surface area ratio is typically between 0.005 and 0.1 ml cm^{-2} [2, 3, 6]. The annulus can contain gases such as CO_2, CH_4, H_2S and H_2O that have permeated from the bore through the polymer sheath into the annulus. When the outer sheath is damaged, substantial amounts of seawater and oxygen may also enter the annulus and affect the environment [7, 8]. The accumulation of gases and water in the annulus is dependent on the permeation through internal and external polymer sheaths, draining systems at the end fittings, the structure of the flexible pipe, the polymer sheaths, conditions in the bore (e.g. pressure, temperature and bore fluid composition) and external conditions (e.g. seawater temperature and depth) [9]. The H_2S content in the bore is often low, with partial pressures less than 100 mbar, and the diffusion from bore to annulus is slow, resulting in low flow rates of H_2S [6]. The amount may be so small compared to the exposed steel area that all the gas is consumed in production of FeS. The temperature in the annulus is typically between 20 and 80°C, depending on the temperature in the bore and the thermal properties of the structure [2]. Uniform corrosion rates below 10 μm y^{-1} have been reported for typical annulus environments [3]. The low corrosion rates have been attributed to the precipitation of protective iron carbonate films. The films are formed by super-saturation of iron ions in the presence of CO_2 that leads to increased pH and accelerated precipitation [3]. When H_2S is present, the corrosion films also contain FeS [10]. However, the protective films may be weakened or prevented from forming in the event of oxygen or seawater ingress, continuous water condensation or partial inhibition.

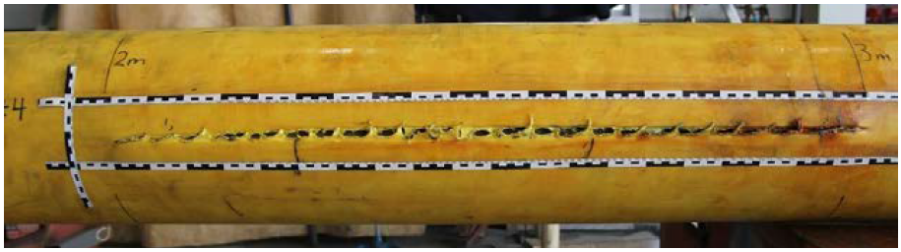

Figure 1.2: Damaged flexible pipe. Image from [11].

The integrity of a flexible pipe is determined by the cross-section design, global system design and fabrication quality [12]. The complexity of the pipe design makes repairs difficult. The degradation and failure mechanisms must be well understood to make good pipe designs with adequate margins against failure. Several failures have occurred due to integrity issues that were not predicted [8]. Investigations of recovered pipes have sometimes shown severe unexpected degradation, but there have also been occasions where satisfactory pipe conditions for continued operation were found [12]. Possible

failure mechanisms for the tensile armour wires include failure by rupture, compression failure, torsional failure, fatigue or corrosion from seawater exposure or exposure to diffused species [13]. Figure 1.2 shows burst damage on a flexible pipe that had been in operation for 15 years. See also Figure 1.3, which shows corroded tensile armour wires in the same pipeline. The required performance of flexible pipes is continuously expanded as the oil and gas production occurs at deeper waters and higher temperatures [14], and the H_2S content in the well-fluid is increasing [6]. This creates a conflict of interest, since high strength steels generally have a lower resistance to hydrogen embrittlement.

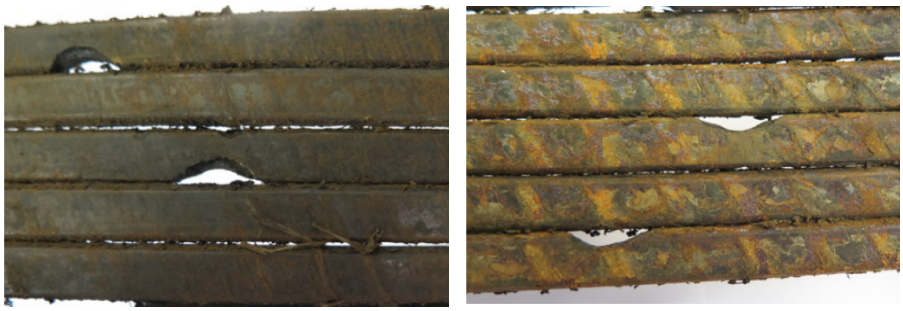

(a) Outer surface of wires (b) Inner surface of wires

Figure 1.3: Damaged flexible pipe armour wires. Image from [11].

1.2 Objectives and scope

Acquiring knowledge about the possible failure mechanisms of flexible pipes will both improve new pipe designs and increase the knowledge basis for evaluation of lifetime extension. In this PhD project the environmentally assisted cracking of six types of steel tensile armour wires was investigated by measuring the hydrogen uptake in the wires in simulated environments and by tensile tests on smooth and notched samples in air and during hydrogen exposure from cathodic polarisation. Two types of environments were used in the experimental work. When the materials were exposed to cathodic polarisation, the samples were free from corrosion products and the electrolyte was a 3.5 % NaCl solution. For hydrogen uptake measurements in a corrosive environment at open circuit potential (OCP), artificial seawater containing CO_2, and sometimes H_2S, was used while the iron content was kept low by replacing the electrolyte continuously. This environment is much more aggressive than the environment inside the flexible pipe annulus and is simulating more actively corroding areas without a protective film. The aggressive environment was chosen since tensile wires normally do not fail under normal operating conditions. The scope was limited to testing at room temperature or 25°C and ambient pressures. The effects of lubricants, inhibitors and anti-wear tape were not included in the scope.

The main objectives of this work are given below:

- Investigate how the microstructure of steel armour wires for flexible pipes affects the relative hydrogen uptake during cathodic polarisation.
- Quantify the diffusible hydrogen uptake in steel armour wires for flexible pipes during exposure to simulated corrosive CO_2 environments with and without H_2S.
- Investigate the interplay between corrosion, hydrogen uptake and microstructure of steel armour wires for flexible pipes.
- Investigate the effect of hydrogen on the mechanical properties of steel armour wires for flexible pipes on a macro scale.

1.3 Thesis overview

This thesis is based on four research papers that resulted from the Ph.D. work. Three of the papers are journal papers, while the last paper is a peer-reviewed conference paper. These are given in the appendix. The details of the papers and contributions of each author are presented below. The chemical composition of the wires, which is included in all the papers, was estimated by glow-discharge optical emission spectroscopy and conducted by Sergey Khromov at the Department of Materials Science and Engineering at The Norwegian University of Science and Technology.

Paper I

Ellen S. Skilbred, Mariano Kappes, Mariano Iannuzzi and Roy Johnsen. Hydrogen uptake and diffusivity in steel armor wires with different chemical composition, carbide distribution, grain size, and degree of deformation. *Materials and Corrosion* (2021). Doi: 10.1002/maco.202112615. Published online 08.11.2021.

Contributions:

- Ellen Synnøve Skilbred planned and executed the experimental work, analysed the data and prepared the manuscript.
- Mariano Kappes, Mariano Iannuzzi and Roy Johnsen, contributed with intellectual discussions, data analysis and editing of the manuscript.

Paper II

Ellen S. Skilbred, Simona Palencsár, Arne Dugstad and Roy Johnsen. Hydrogen uptake during active CO_2-H_2S corrosion of carbon steel wires in simulated annulus fluid. *Corrosion Science* (2022). Doi: 10.1016/j.corsci.2022.110172.

Contributions:

- Ellen Synnøve Skilbred planned and executed parts of the experimental work, analysed the data and prepared the manuscript.
- Simona Palencsár executed parts of the experimental work, and contributed also with planning experiments, intellectual discussions, data analysis and writing of the manuscript.
- Arne Dugstad and Roy Johnsen contributed with planning experiments, intellectual discussions, data analysis and editing of the manuscript.

Paper III

Ellen S. Skilbred, Aleksander Myhre, Luigi Viespoli, Antonio Alvaro and Roy Johnsen. Correlation between microstructure and hydrogen embrittlement susceptibility of flexible pipe steel armor wires measured by slow strain rate testing of notched samples. *To be submitted.*

Contributions:

- Ellen Synnøve Skilbred planned and executed the experimental work, analysed the data, extracted data from the finite element models and prepared the manuscript.
- Aleksander Myhre contributed with preparation of the experimental rig, analysis of data, intellectual discussions and editing of the manuscript.
- Luigi Viespoli created finite element models and contributed with intellectual discussions and editing of the manuscript.
- Antonio Alvaro and Roy Johnsen contributed with intellectual discussions and the planning and execution of experiments including data analysis as well as editing of the manuscript.

Paper IV

Ellen S. Skilbred, Signe A. Lootz and Roy Johnsen. Hydrogen embrittlement susceptibility of steel armour wires for flexible pipes. *CORROSION 2020*, physical event cancelled but the paper was published, June 2020. Paper no. C2020-14489.

Contributions:

- Ellen Synnøve Skilbred planned and executed some of the experimental work, analysed the data and prepared the manuscript.

- Signe Aarthun Lootz conducted most of the experimental work as part of her Master's degree and contributed with analysis of data and editing the manuscript.
- Roy Johnsen contributed with intellectual discussions and the planning and execution of experiments including data analysis as well as editing of the manuscript.

2 Corrosion in aqueous CO_2 and H_2S environment

When the flexible pipe annulus is wet, the liquid inside is highly saturated with corrosion products due to the low free volume in the annulus compared to the area of the steel armour wires. The annulus contains species that have diffused from the bore, e.g. CO_2, H_2S and H_2O, and can also contain seawater and oxygen if the outer sheath is damaged.

This chapter describes the mechanisms of aqueous CO_2 and H_2S corrosion for carbon steels, with focus on conditions that are relevant for corrosion in flexible pipe annulus.

2.1 CO_2 corrosion in aqueous environments

2.1.1 Corrosion mechanism

CO_2 forms carbonic acid, H_2CO_3, when dissolved in water [15]

$$CO_2 + H_2O \longrightarrow H_2CO_3 \tag{2.1}$$

Carbonic acid is a weak acid which partially dissociates in two steps [16]

$$H_2CO_3 \Leftrightarrow H^+ + HCO_3^- \tag{2.2}$$

$$HCO_3^- \Leftrightarrow H^+ + CO_3^{2-} \tag{2.3}$$

The most likely cathodic reactions during pure CO_2 corrosion include [15, 17]

$$2H^+ + 2e^- \longrightarrow H_2 \tag{2.4}$$

$$H_2CO_3 + 2e^- \longrightarrow H_2 + 2HCO_3^- \tag{2.5}$$

H^+ is continuously provided by water dissociation as well as the dissociation steps of H_2CO_3. The main anodic reaction is the dissolution of iron

$$Fe \longrightarrow Fe^{2+} + 2e^- \tag{2.6}$$

The presence of CO_2 is known to increase the corrosion rate of pipeline steel, but the mechanism is not completely understood. A recent study [18] showed that the increased corrosion rates of mild steel in acidic CO_2 solutions occurred mainly due to enhanced iron dissolution rates (Equation (2.6)). The cathodic limiting currents increased with

the CO_2 partial pressure, but the charge-transfer was not affected, and the observation was linked to the buffering ability of dissolved CO_2 and H_2CO_3.

When the concentrations of Fe^{2+} and CO_3^{2-} exceed their solubility limits, iron cabonate can be formed, and the overall reaction for CO_2 corrosion is

$$Fe + CO_2 + H_2O \longrightarrow FeCO_3 + H_2 \tag{2.7}$$

The driving force for $FeCO_3$ precipitation is the supersaturation or saturation ratio, S_{FeCO_3}, defined as

$$S_{FeCO_3} = \frac{a_{Fe^{2+}} a_{CO_3^{2-}}}{K_{sp,FeCO_3}} \tag{2.8}$$

where $a_{Fe^{2+}}$ and $a_{CO_3^{2-}}$ are the activities of iron and carbonate ions, respectively, and $K_{sp,FeCO_3}$ is the solubility product of $FeCO_3$. Precipitation usually occurs close to the steel surface since the concentration of Fe^{2+} is highest there. Several models have been proposed for the relation between $K_{sp,FeCO_3}$ and temperature. According to a review from 2018 [19], one of the most common models for $K_{sp,FeCO_3}$ was proposed by Greenberg and Tomson [20]:

$$\log(K_{sp,FeCO_3}) = -59.2385 - 0.041377(T) - \frac{2.1963}{T} + 24.5724\log(T) \tag{2.9}$$

where T is the absolute temperature. A constant in the model was modified by [21] and the ionic strength, I, was included to enable the use of concentrations of Fe^{2+} and CO_3^{2-} rather than activities:

$$\begin{aligned} \log(K_{sp,\ FeCO_3}) \quad = \quad & -59.3498 - 0.041377(T) - \frac{2.1963}{T} + 24.5724\log(T) \\ & +2.518(I^{0.5}) - 0.657(I) \end{aligned} \tag{2.10}$$

where I is a function of the specie concentrations in the aqueous solution, c_i, in mol L^{-1}, and the specie charge z_i

$$I = \frac{1}{2}\sum_i c_i z_i = \frac{1}{2}(c_1 z_1 + c_2 z_2 + ...) \tag{2.11}$$

For ferritic-pearlitic steels, the dissolution of iron from the ferrite phase can leave a retained Fe_3C structure on the surface [22–24]. A network of retained carbides is shown in Figure 2.1. Fe_3C is electrically conductive and a main site for cathodic reactions during CO_2 corrosion. Hence, if the retained Fe_3C stays in contact with the steel surface, the cathodic reactions are enhanced and the dissolution of ferrite accelerated [22, 25]. This can result in a higher corrosion rate and increased OCP [24]. The retained Fe_3C can form a thick porous layer, which can act as a barrier to diffusion of Fe^{2+} and hence increase S_{FeCO_3} and promote the formation of $FeCO_3$ within the network [26–28].

Pearlite regions have been observed to anchor the $FeCO_3$ to the surface and improve corrosion protection [29], but it has also been proposed that carbide layers can promote corrosion by internal acidification which prevents $FeCO_3$ precipitation [26, 28, 30].

A well-protecting $FeCO_3$ film acts as a diffusion barrier for the cathodic reactants and can reduce the corrosion rate to below 10 µm y^{-1} [31]. The protection of the $FeCO_3$ film increases with the pH [32] and the supersaturation of iron, which can be facilitated by stagnant conditions [33]. Porous films give less protection, and although the film accumulation may be higher at lower temperatures, the corrosion protection will not be effective if the film is porous. The presence of carbonate-forming cations like Mg^{2+} and Ca^{2+} can affect the composition and protectiveness of carbonate layers formed during CO_2 corrosion, for example by precipitation of mixed Fe, Mg and Ca scales [34], non-protective calcium carbonate ($CaCO_3$) [35] or porous, Ca-enriched $FeCO_3$ [36]. The $FeCO_3$ film can also suffer from localized attacks due to low pH [37], and the presence of O_2 [38, 39].

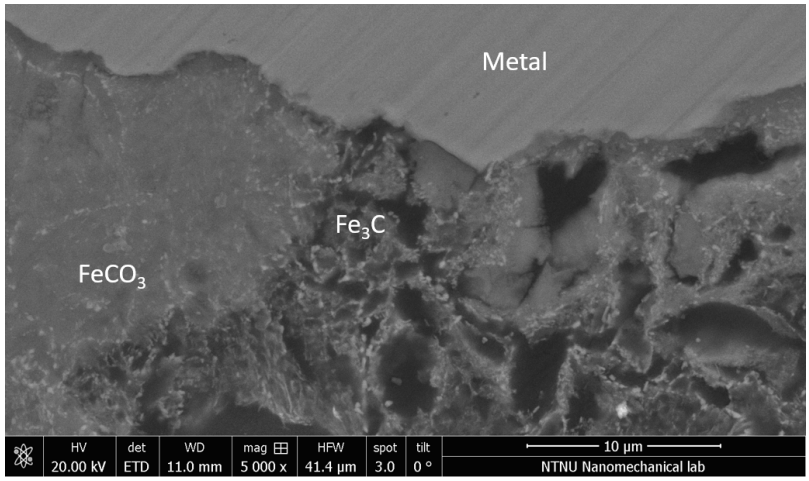

Figure 2.1: Iron carbonate and retained carbides formed by CO_2 corrosion of a ferritic-pearlitic steel.

2.1.2 Effect of microstructure

Both steel composition, thermomechanical processing and microstructure can influence the corrosion rate and mechanism observed in CO_2 environments.

The presence of elements Cr and Mo in solid solution can improve the corrosion resistance of steels in CO_2 environment [26, 40]. Cr improves the corrosion resistance by formation of a stable chromium oxide, and amounts from 0.5 to 3 wt% are considered beneficial.

Mo is considered beneficial in concentrations 0.15-0.25 wt%, typically in combination with Cr [19]. The beneficial effect of Cr and Mo on corrosion depends on their presence in solid solution. Both Cr and Mo are carbide forming elements, and heat treatments can deplete the alloy for these elements and give increased corrosion susceptibility. The addition of stronger carbide formers, like V, Ti and Nb, is considered beneficial for keeping a higher fraction of the Cr and Mo in solid solution.

The effects of carbon content, heat treatments and carbide morphology on CO_2 corrosion have been studied in several publications. Yudin et al. [41] investigated the effect of heat treatment and microstructure in steel 20 (0.17 wt% C) on corrosion rate in 3% NaCl with CO_2 at ambient temperatures and 120 h exposure. The results showed that the samples with martensite had a higher corrosion rate than the ferritic-pearlitic samples, and that shape of pearlite, lamellar vs. granular, did not have a noticeable effect on corrosion rate. Lopez et al. [42] investigated the corrosion properties of a 0.38 wt% carbon steel heat treated to form two different microstructures: An annealed sample with ferrite and lamellar pearlite, and a quenched and tempered sample with an even distribution of globular cementite particles. The test solution was 5 % NaCl saturated with CO_2. The corrosion layer thickness of both samples was up to 25 µm, but the morphology was different, as the lamellar cementite remained un-corroded on the surface.

Al-Hassan et al. [40] investigated the effect of steel microstructure on corrosion rate in aqueous CO_2 environment at temperatures between 38 and 65°C. The steels had carbon contents up to 0.78 wt% and samples with different heat treatments were tested for each of the materials. For iron and the plain carbon steels, the corrosion rate increased with increasing carbon content. The lowest corrosion rates were observed for pure iron, which formed no corrosion scales. Several samples of an X-52 steel were tested after different heat treatments. At temperatures below 51°C, no protective $FeCO_3$ was formed on the X-52 steel samples, and there was a trend of lower corrosion rates for annealed samples, and higher corrosion rates for the as-received material. For the quenched and tempered samples, a higher tempering temperature gave a lower weight loss. This was attributed to the coarsening of carbide particles with tempering temperature, which gives a smaller ferrite-carbide interfacial area. Similarly, higher corrosion rates observed in normalized samples compared to annealed samples were attributed to the increased area of contact between pearlite and ferrite grains in the normalized steel.

Ochoa et al. [43] tested the CO_2 corrosion resistance of an API X42 steel with samples of four different heat-treatments in a 0.5 M NaCl solution bubbled with CO_2. The corrosion resistance increased in the order banded < normalized < quenched and tempered < annealed. It was especially the cathodic current densities that were affected by the microstructural changes. The quantity of $FeCO_3$ on the steel surface was higher for annealed, and quenched and tempered steels than the other samples.

2.2 H_2S corrosion in aqueous environments

H_2S is a weak acid which partly dissociates in two steps [44]

$$H_2S \Leftrightarrow H^+ + HS^- \tag{2.12}$$

$$HS^- \Leftrightarrow H^+ + S^{2-} \tag{2.13}$$

The main mechanism behind H_2S corrosion is much less understood than the mechanism of CO_2 corrosion [45]. A recent review summarised the following anodic reactions for H_2S corrosion [46]

$$Fe + H_2O + H_2S \Leftrightarrow FeSH^-_{ads} + H_3O^+ \tag{2.14}$$

$$FeSH^-_{ads} \Leftrightarrow Fe(SH)_{ads} + e^- \tag{2.15}$$

$$Fe(SH)_{ads} \Leftrightarrow +FeSH^+ + e^- \tag{2.16}$$

$$FeSH^+ + H_3O^+ \Leftrightarrow Fe^{2+} + H_2O + H_2S \tag{2.17}$$

$$2FeSH^+ \Leftrightarrow FeS_{ads} + SH^- + H^+ + Fe^{2+} \tag{2.18}$$

$$2n\ FeS_{ads} \longrightarrow 2n\ Fe_2S_2 \longrightarrow 2n\ FeS_{mackinawite} \tag{2.19}$$

The cathodic reactions are [44]

$$2H^+ + 2e^- \longrightarrow H_2 \tag{2.20}$$

$$H_2S + 2e^- \longrightarrow HS^- + H_2 \tag{2.21}$$

$$2HS^- + 2e^- \longrightarrow 2S^{-2} + H_2 \tag{2.22}$$

The H^+ ions originates from water dissociation and from the dissociation of H_2S in reactions (2.12) and (2.13). In the absence of protective corrosion layers, the corrosion rates in H_2S environment have been shown to increase with the partial pressure of H_2S [47]. H_2S can affect both cathodic reactions and the anodic reactions [47]. For example, Cheng et al. [48] investigated the influence of pH and H_2S concentration on corrosion of iron in acid solutions, and found that the anodic dissolution was accelerated by pH and H_2S until the ratio of H_2S concentration to H_3O^+ concentration exceeded $10^{1.5}$.

The first FeS precipitate is in the form of mackinawite [49]. Mackinawite is expected to be formed on the steel surface from adsorbed FeS, see Equation (2.19), which gives a good adhesion of corrosion products [50]. Mackinawite can precipitate as nano-sized

platelets which are difficult to detect with classical X-ray diffraction (XRD), since this technique relies on many repetitions of a periodic lattice, and this has led to wrongful characterization of mackinawite as amorphous FeS [51]. Mackinawite has also been reported as non-stochiometric, but this has also been disproved [52]. Accoring to Wen et al. [46], the FeS_{ads} is the amorphous FeS and the most common corrosion product formed for carbon steels in H_2S environment, and according to Rickard et al. [51], mackinawite is usually the major constituent of precipitated FeS.

In addition to mackinawite, the other solid phases in the Fe-S system are cubic FeS, troilite, pyrrhotite, smythite, greigite, pyrite and marcasite [51]. Their properties are listed in Table 2.1. Mackinawite is one of the most common corrosion products for H_2S corrosion at temperatures below 100°C [46]. Cubic FeS is mainly found for temperatures below 60°C, while troilite, pyrrhotite and pyrite typically form at high temperature and high H_2S pressure [46]. The iron sulphides are usually reported as conductive or semi-conductive, but the reported conductivities are often deviating [53]. The corrosion product films formed in H_2S environment can consist of several of these phases, which gives a variety of electrochemical behaviours observed [46], for example double layers which have been reported to act as diffusion barriers for electrochemical species [54, 55] and which have been reported to retard the charge transfer kinetics of both anodic and cathodic reactions [56].

Table 2.1: Properties of iron sulphide compounds. From [53] and [51].

Material	**Composition**	**Lattice**	**Stability**
Mackinawite	$Fe_{1-x}S$, x = 0.005-0.025	Tetragonal	Metastable
Cubic FeS	FeS	Cubic	Highly unstable phase
Troilite	FeS	Hexagonal	
Pyrrhotite	$Fe_{1-x}S$	Hexagonal	
	Fe_7S_8	Monoclinic	
Smythite	Fe_9S_{11}, Fe_7S_8	Hexagonal	Metastable
Greigite	Fe_3S_4	Cubic	Metastable
Pyrite	FeS_2	Cubic	Stable iron(II)disulphide
Marcasite	FeS_2	Orthorhombic	Metastable iron(II)disulphide

2.3 Corrosion in aqueous environments with both H_2S and CO_2

The corrosion of steel in aqueous environments containing both H_2S and CO_2 can be affected by all the chemical reactions mentioned in this chapter so far. A low H_2S

concentration in CO_2 environment can increase CO_2 corrosion by promoting anodic dissolution through sulphide adsorption and affecting the pH, but the CO_2 corrosion can also be decreased by the formation of a protective sulphide scales [26]. For oil and gas corrosion in CO_2 and H_2S environment, Smith and Pacheco [57] listed the following species as the main corrosion products: Fe^{2+}, $FeCO_3$, mackinawite, cubic FeS, pyrrhotite and pyrite. Generally, pyrrhotite and pyrite are formed at higher H_2S concentrations than mackinawite and cubic FeS, and cubic FeS is typically found at higher temperatures than mackinawite.

The corrosion mechanism for steels under combined H_2S and CO_2 exposure depends on the H_2S/CO_2 ratio. In experiments where low carbon steels were exposed to NaCl solutions with CO_2 and <3 mbar H_2S, Kvarekvål et al. [58] found that CO_2/H_2S ratios of 1200-1500 resulted in formation of thin iron sulfide films (1-10 μm) but no iron carbonates. For CO_2/H_2S partial pressure ratio of 4500, mixed sulfide/carbonate films were detected on the steel surface. Thermodynamic solubility data were in favour of iron sulfide formation under these conditions, and the coexistence of FeS and $FeCO_3$ was attributed local depletion of sulfide ions within the corrosion product films.

In oil and gas systems, the average corrosion rates are often lower in sour conditions compared to systems with CO_2 and no H_2S (sweet corrosion). However, the corrosion rate can be high in some areas of the surface in the event of localized corrosion. Localized corrosion attacks can act as stress-concentrators and can decrease the load-bearing ability of a component when the attack is deep. Localized corrosion can be difficult to detect since the pits and trenches can be covered beneath un-protective corrosion products. Pessu et al. [59] observed a higher pitting initiation rate for the combined presence of CO_2 and H_2S exposure, compared to the presence of each gas individually. Esmaeely et al. [60] found a threshold H_2 concentration for formation of localized attacks for a mild steel. For H_2 contents below 100 ppm and $p_{H_2}/p_{CO_2} < 10^{-4}$, the mackinawite layer was unstable and the steel suffered from localized corrosion.

One of the characteristics of the flexible pipe annulus environment is the high surface-to-volume ratio which gives a high iron saturation and promotes formation of corrosion products. Dugstad et al. [10] examined how the introduction of H_2S affects protective films and corrosion of flexible pipe steel armour wires. The wires were exposed to a CO_2 solution with high iron concentration, and formed protective $FeCO_3$ films before H_2S was added to the environment. The effect of H_2S was described as follows: When the precipitation of FeS consumes Fe^{2+} at a higher rate than the corrosion produces new Fe^{2+}, the concentration of Fe^{2+} decreases. When $S_{FeCO_3} = 1$, the $FeCO_3$ starts to dissolve. When the majority of the $FeCO_3$ is dissolved, the concentration of Fe^{2+} can decrease further. For a test where 1 kPa H_2S was added to a NaCl solution with 0.02 MPa CO_2 after 150 h of exposure, only traces of $FeCO_3$ was left on the steel surface after 285 h of exposure to H_2S.

Another characteristic of the flexible pipe annulus environment is that the amount of H_2S

can be small and can be consumed in the corrosion processes. Since the presence of H_2S has been responsible for hydrogen damage failures, the depletion of H_2S due to corrosion can be considered positive from an engineering perspective. Several models have been made to predict the annulus environment in flexible pipes [9, 61, 62]. A permeability model calibrated with full scale tests and field cases was developed by Taravel-Condat et al. in 2002 [9, 62]. The model considered the permeation of CH_4, CO_2, H_2S and H_2O from bore, temperature gradient through the structure and its effect on the permeation coefficients, the shielding effect of the steel on the internal plastic sheath, thermodynamic phase equilibrium in the annulus, water condensation and gas release out of the annulus through gas-release valves. The same model was used later to show that, given a small H_2S amount in bore and a large steel surface to electrolyte volume ratio, the H_2S amount in annulus is lower than the amount estimated at steady state because of significant H_2S consumption [6].

3 Environmentally assisted cracking

Environmentally assisted cracking (EAC) is a general term for embrittlement mechanisms caused by a combination of environmental factors and tensile stress [63]. This is often observed as brittle fracture of materials that are normally failing in a ductile manner. EAC is dependent on three types of factors: environmental, metallurgical and mechanical. Temperature, pH and presence of chemical species are examples of environmental factors. The metallurgical factors include microstructure, alloy and phase composition. Mechanical factors can be cyclic or static loading, and residual stresses.

The proposed mechanisms for the environmental enhancement in EAC include [45]:

- Enhanced plastic rupture or decohesion caused by hydrogen or liquid metal adsorption or absorption.
- Crack growth by highly localised corrosion process, which is intensified by local plastic deformation. This is often called slip-dissolution or slip-oxidation.
- Film-induced substrate fracture, also called film-induced cleavage.
- Creep-like mechanisms, e.g. surface mobility and vacancy injection.

Examples of EAC mechanisms are hydrogen embrittlement (HE), liquid metal embrittlement (LME), stress corrosion cracking (SCC), sulphide stress cracking (SSC) and corrosion fatigue (CF) [64]. LME is environmental cracking caused by contact with a liquid metal [63]. SCC is cracking in a material due to combined corrosion and sustained tensile stress. SCC fractures can be driven by anodic dissolution and HE, due to hydrogen ingress from cathodic reactions [65]. In the presence of H_2S, the mechanism is defined as SSC. CF is an EAC mechanism where both a corrosive environment and cyclic loading are influencing the fracture mechanism.

The EAC mechanisms may be labelled differently depending on small changes in the three determining factors. For SCC and HE, there is a sensitivity to strain rate where a too high strain rate gives a fracture mode that is not affected by hydrogen. A very low strain rate can give a failure mechanism controlled purely by corrosion rather than SCC. For CF, a very high load or frequency makes the fracture mechanism manifest as a pure fatigue fracture, while a very low frequency or load in a corrosive environment can lead to a pure corrosion failure mechanism. Another example is the definitions of SCC and SSC in ANSI/NACE standard TM0177-96 [66], which considers the combination of tensile stress and corrosion in aqueous H_2S-containing environments as SSC at room temperature and SCC for higher temperatures.

HE is defined as embrittlement caused by the presence of hydrogen within a metal or alloy [63], but the term can also be used more specifically about embrittlement mechanisms that depend on the presence of atomic hydrogen in the material. HE susceptibility is typically analysed by destructive mechanical tests, but HE does not necessarily lead to failure in the field. In the next section, several hydrogen damage mechanisms are discussed to elaborate the differences between mechanisms relying on atomic hydrogen vs. hydrogen gas, and damage related to applied stress vs. damage related to internal stresses.

3.1 Hydrogen damage mechanisms

Hydrogen can degrade the mechanical properties of materials and cause damage by several mechanisms. Some of these are illustrated in Figure 3.1. The effect of hydrogen on physical and mechanical properties is usually seen in one or more of the following forms [67]

- Internal cracks, pores or blisters resulting from a pressure build-up of hydrogen gas, which can be entrapped from production steps or arise from recombination of atomic hydrogen. This type of failure is associated with the internal pressure theory [68].
- Formation of brittle hydrides. This mechanism was first described by Westlake [69] and only occurs for hydride-forming materials, such as Ti, Zr, Nb and V.
- A change of fracture mechanism due to hydrogen which is not associated with the formation of hydrides or hydrogen gas. Here, we refer to this as hydrogen-assisted cracking (HAC).

This classification describes the appearance of the observed hydrogen damages, but the hydrogen damage mechanisms are also distinguished by the presence or absence of applied stress. Hydrogen stress cracking (HSC) is defined as cracking under the combined action of tensile stress and the presence of hydrogen [63], and can be considered a form of HAC. HSC can be caused by HE, but HE does not necessarily lead to cracking [67].

Failures related to the pressure of H_2 gas are not considered EAC mechanisms, as they do not rely on applied stress. Gaseous hydrogen can cause stepwise cracking (SWC) or individual smaller cracks, called hydrogen induced cracking (HIC). For stress oriented hydrogen induced cracking (SOHIC), the formation of cracks is driven by both atomic and molecular hydrogen [45]. The occurrence of the different types of hydrogen damage mechanisms depends both on environmental factors and on material properties. For example, the hydrogen-related cracking of high strength steels is often in the form of HE, whereas softer steels may suffer from hydrogen pressure induced cracking [45].

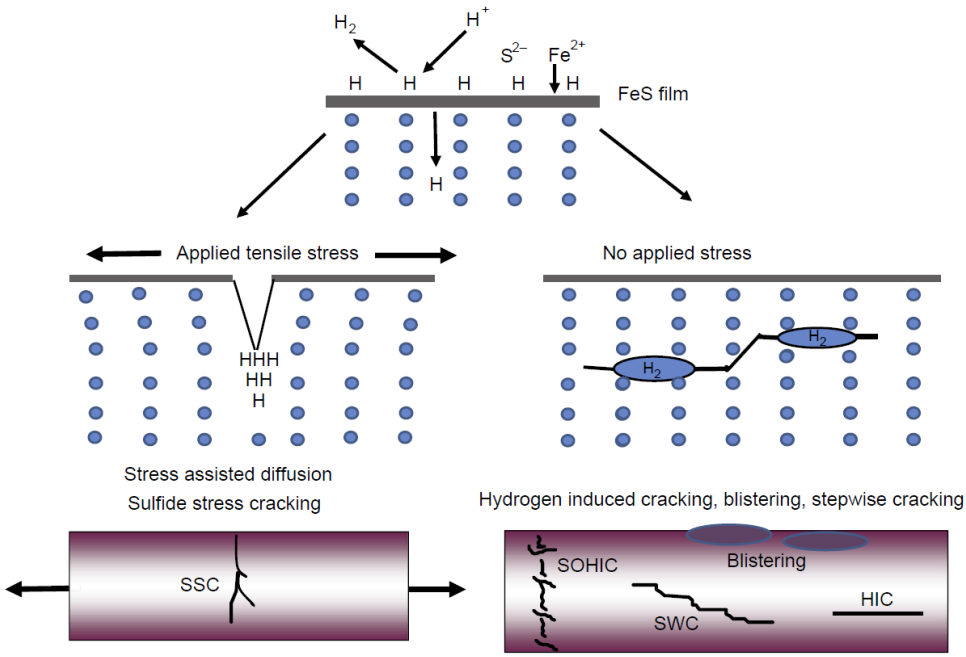

Figure 3.1: Hydrogen damage mechanisms illustrated. Figure from [67].

3.2 Hydrogen embrittlement of steels

Hydrogen has on many occasions been observed to cause brittleness and premature failure in metals. HE happens as a consequence of metallurgical, environmental and mechanical factors, similarly to EAC in general. Among the main sources of hydrogen in steels are welding, acid pickling, degreasing and cleaning, electroplating, phosphating, painting and corrosion in service [70]. For the steel armour wires in flexible pipes, corrosion and cathodic polarisation are the most relevant sources of hydrogen and the following sections focus on hydrogen embrittlement under these conditions.

3.2.1 Hydrogen entry from aqueous solutions

During cathodic polarisation and corrosion of metals in aqueous solutions, hydrogen ions can adsorbe on the surface and recombine to hydrogen gas, see Equation (2.4) and (2.20). The adsorption process is called the Volmer reaction [45] and will happen according to Equation (3.1) in acid solution and Equation (3.2) in neutral and alkaline solutions:

$$H_3O^+ + e^- \longrightarrow H_{ads} + H_2O \quad \text{(acidic solution)} \tag{3.1}$$

$$H_2O + e^- \longrightarrow H_{ads} + OH^- \quad \text{(neutral or alkaline solution)} \tag{3.2}$$

The adsorbed hydrogen can react further by the Tafel reaction in Equation (3.3) and the Heyrovsky reaction in Equation (3.4) and (3.5) [45].

$$H_{ads} + H_{ads} \longrightarrow H_2 \tag{3.3}$$

$$H_{ads} + H_3O^+ + e^- \longrightarrow H_2 + H_2O \quad \text{(acidic solution)} \tag{3.4}$$

$$H_{ads} + H_2O + e^- \longrightarrow H_2 + OH^- \quad \text{(neutral or alkaline solution)} \tag{3.5}$$

Alternatively to forming H_2 gas, the adsorbed hydrogen may absorb into the metal [45].

$$H_{ads} \longrightarrow H_{abs} \tag{3.6}$$

The absorbed hydrogen can then diffuse into the steel and cause embrittlement. There are chemical species that enhance the hydrogen uptake by promoting reaction (3.6) and demoting reactions (3.3)-(3.5). These are called hydrogen recombination poisons and include elements S, P and Pb [71], and H_2S [46].

3.2.2 HE mechanisms

Several theories have been proposed to explain how atomic hydrogen causes embrittlement including hydrogen enhanced localized plasticity (HELP) [72, 73], hydrogen enhanced decohesion (HEDE) [74], adsorption-induced dislocation emission (AIDE) [75], hydrogen enhanced strain-induced vacancies (HESIV) [76] and the defactant theory [77].

The HELP mechanism is based on observations of dissolved hydrogen facilitating dislocation movement [78]. The mechanism is illustrated in Figure 3.2. The enhanced movement of dislocations and higher hydrogen concentration lead to more micro-void formation ahead of the crack-tip than in the absence of hydrogen. Fracture surfaces in the environment will therefore have smaller dimples than the fracture surface of the same material tested in air. Both transgranular and intergranular fracture are possible. The HELP mechanism is supported by experimental observations of enhanced dislocation formation and mobility in the presence of hydrogen [79, 80].

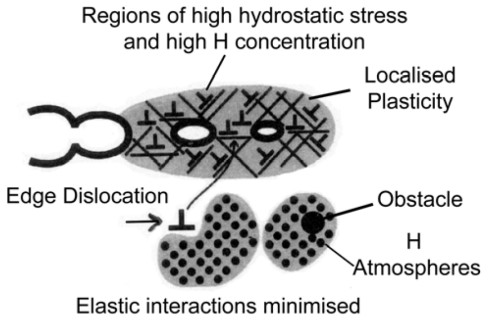

Figure 3.2: HELP mechanism illustrated. Figure from [81].

The HEDE mechanism involves high concentrations of atomic hydrogen weakening interatomic bonds to the extent that tensile separation is easier than slip [78]. The mechanism is illustrated in Figure 3.3. The hydrogen can be adsorbed near the crack-tip or absorbed in the lattice or at trapping sites ahead of the crack-tip. There may be some dislocation activity accompanying the decohesion, but not enough to blunt the crack tip. The HEDE theory is supported mainly by quantum-mechanical calculations which support the concept of hydrogen weakening of interatomic bonds leading to HEDE [82] and modelling of fracture energy in metals when hydrogen is present as a mobile impurity [83].

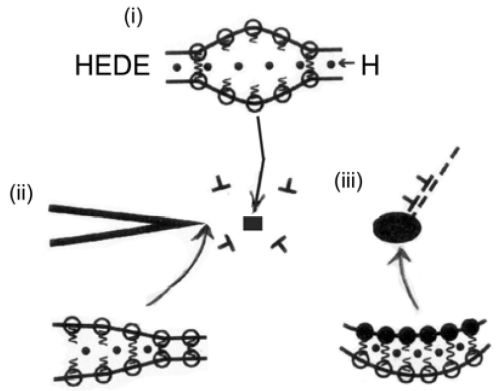

Figure 3.3: HEDE mechanism illustrated. Figure from [81].

During ductile crack growth, dislocations are nucleated in the plastic zone ahead of cracks while dislocation emission at the crack tip is limited. The adsorption-induced dislocation emission (AIDE) theory suggests that hydrogen adsorbed on the crack tip facilitates dislocation nucleation and movement here [78]. Hydrogen is assumed

to promote dislocation formation near the crack-tip by weakening the atomic bonds that must be broken for the dislocation to be formed. Dislocation formation always involves displacement of atoms, and on a surface this requires breaking and reforming of interatomic bonds. This process creates a surface step near the crack tip. The dislocation nucleation is the most critical step of the process, since the dislocation movement is facilitated by the applied stress. Void formation at sites like particles and slip-band intersections require lower stress than dislocation nucleation, and voids are therefore also contributing to the crack propagation in the AIDE theory. The coalescence of cracks with voids occur at lower strains during AIDE than during exposure to inert conditions, and the fracture surface is therefore expected to have shallower and smaller dimples than a fracture surface formed in inert conditions. The AIDE mechanism is supported by atomistic simulations [82, 84] and by observations of hydrogen accumulation on surface ridges in iron-alloys corresponding to slip traces for b.c.c lattice [85].

The HESIV and defactant theories were proposed more recently than the HELP, HEDE and AIDE theories. The HESIV mechanism is based on observations of enhanced formation and agglomeration of vacancies in the presence of hydrogen, and consequently decreased ductile crack growth resistance [76]. It is supported by observations of increased vacancy formation and clustering in the presence of hydrogen [86] and lower formation enthalpy of vacancies in presence of hydrogen [87]. The defactant theory is based on atoms segregating to defects in solids to reduce their formation energy, in a manner analogous to how surfactants reduce surface energies in liquids [77]. The defactants enhance the formation of defects and leads to higher plasticity.

3.2.3 Hydrogen solubility in lattice

The hydrogen solubility, C_o, in body centered cubic (bcc) iron is given by a Sievert-type equation [88].

$$C_o = 0.00185 P^{0.5} \exp\left(-\frac{3440}{T}\right) \tag{3.7}$$

Equation (3.7) gives the hydrogen solubility in unit atom H per atom Fe. P is the H_2 gas fugacity at the metal/electrolyte interface in atm and T is the absolute temperature in K. The behaviour of hydrogen is like an ideal gas until at least 200 atm, which means that pressure can be used instead of fugacity [89].

The hydrogen solubility in lattice increases with triaxial stress due to dilatation of the lattice [90], and the hydrogen concentration can therefore increase significantly during elastic straining. The presence of notches, pits and cracks leads to local areas of high triaxial stress which are often seen as initiation points for cracks. At high stress concentration factors, a systematic loss in fracture stress with increased stress concentration factor has been observed, until the fracture stress becomes relatively constant [91]. This adds complexity to the prediction of hydrogen concentration in

a material during straining, since the formation of cracks gives areas of higher stress concentration and the blunting of cracks and notches gives a lower stress concentration. Ideally, the hydrogen concentration in a strained materials should be estimated with continuous geometry update along with the transient loading [92].

For a quasi-static straining (i.e. slow enough to neglect time effects), the concentration of hydrogen in a position x, $c(x)$, in a sample is a direct function of the hydrostatic stress in the position, $\sigma(x)$ [93]:

$$c(x) = c_0 \exp\left(\frac{V^* \sigma(x)}{RT}\right) \tag{3.8}$$

where V^* is the molar partial volume of hydrogen, R the gas constant and T the absolute temperature.

3.2.4 Trapping of hydrogen

Certain microstructure features have a higher affinity to hydrogen than the lattice sites, making hydrogen more or less temporarily trapped. Traps are usually defined as either reversible or irreversible, according to the residence time of hydrogen in the trap [94] or the binding energy between the hydrogen and the trap [95]. Irreversible traps are microstructural sites where the residence time for a hydrogen atom is extremely long compared to the time-scale for permeation testing, or the binding energy with hydrogen is relatively high. A binding energy of > 60 kJ mol^{-1} has been suggested as a rule of thumb [95]. Reversible traps are microstructural sites where the residence time for a hydrogen atom is longer than the residence time in lattice sites but small in relation to the time to attain steady-state permeation, or the binding energy is relatively low, e.g. $<$60 kJ mol^{-1}. The hydrogen in reversible traps can diffuse to areas of high local stress and is therefore considered more detrimental than hydrogen in irreversible traps, even when a higher hydrogen concentration exists at irreversible traps [96]. Irreversible traps are sometimes considered beneficial due to their ability to attract hydrogen from the lattice and prevent it from diffusing to areas of high stress. However, the effect is limited due to the finite number of irreversible traps, and the benefit will be ineffective for cases where hydrogen is still diffusing into the material after the irreversible traps are filled [97].

The most common trap sites for iron and steels are grain boundaries, phase boundaries, voids, inclusions and dislocations [70]. The interface between ferrite and precipitates like MnS [98, 99] TiC [100, 101], NbC and VC, and complexes of Ti, Nb, C, S and N [102], are all examples of hydrogen traps [103, 104]. Cold working increases trapping substantially due to the formation of dislocations and vacancies which can trap hydrogen. Subsequent heat-treatments like ageing can reduce the hydrogen uptake due to the annihilation of vacancy-clusters and vacancy-carbon pairs [105]. For phase boundaries, the hydrogen binding energy is both dependent on the type of particle and the coherency with the matrix [106, 107]. A low coherency between particles and matrix can give high binding energies for hydrogen trapping, while particles with high coherency with the

matrix have a lower binding energy and are more likely to be classified as reversible traps.

There is a large discrepancy of reported hydrogen trapping energy values for ferrite-cementite interfaces, e.g. 10.85 kJ mol^{-1} [108] and 68.4 kJ mol^{-1} [109]. Kawakami and Matsumiya [110] reported a trap energy of 47 kJ mol^{-1} at the coherent interface between strained ferrite and unstrained cementite. Takai and Watanuki [96] investigated the trapping energy in a cold-drawn eutectoid steel, and found hydrogen trap activation energy peaks of 23.4 kJ mol^{-1} and 65.0 kJ mol^{-1}. The peak with highest energy was associated with hydrogen trapping on strained ferrite-cementite interfaces, and/or the interface dislocations enclosed between cementite lamellae due to cold-drawing. The lower energy peak was associated with trapping on unstrained ferrite-cementite interfaces and other low energy traps, e.g. vacancies, strain field of dislocations, dislocation cores, grain boundaries.

3.2.5 Hydrogen diffusion

The diffusion of hydrogen is controlled by Fick's ficks first and second laws

$$J = -D\frac{\partial C}{\partial x} \tag{3.9}$$

$$\frac{\partial C}{\partial t} = D\frac{\partial^2 C}{\partial x^2} \tag{3.10}$$

The hydrogen diffusion coefficient, D, is often determined in a permeation experiment where a metallic disc-shaped sample is exposed to a source of hydrogen on one side, and the resulting permeation flux of hydrogen, J, is measured on the other side. At room temperature, hydrogen occupies mainly tetrahedral sites in bcc steels and the the activation energy for the movement of hydrogen between tetrahedral sites, Q, has been estimated to 5.69 kJ mol^{-1} [111]. The diffusion of hydrogen between lattice sites is a function of temperature which follows the Arrhenius relation and in the temperature range from -40°C to 80°C, D, is defined by

$$D = D_0 \exp\left(\frac{-Q}{RT}\right) \tag{3.11}$$

where D_0 is 7.23×10^{-8} m^2s^{-1}, R is the gas constant and T is the absolute temperature.

The hydrogen diffusivity in a metallic material is strongly affected by the presence of hydrogen traps and the occupancy of the traps. When the diffusion coefficient of a material is measured under non-steady-state conditions, it is described as an effective diffusion coefficient, D_{eff}. When a hydrogen-free sample is charged with hydrogen, the diffusion may be initially slowed down by the trapping of hydrogen. As more traps are

filled, the diffusivity increases until it reaches the lattice diffusivity of the material, D_L. This can lead to a steeper gradient for the normalised permeation flux than Fick's law [94, 112]. However, the effect of microstructure on permeation is complex. For example, deformed microstructures are observed to have less steep increase in permeation flux from zero hydrogen to steady-state [113, 114], as displayed in Figure 3.4.

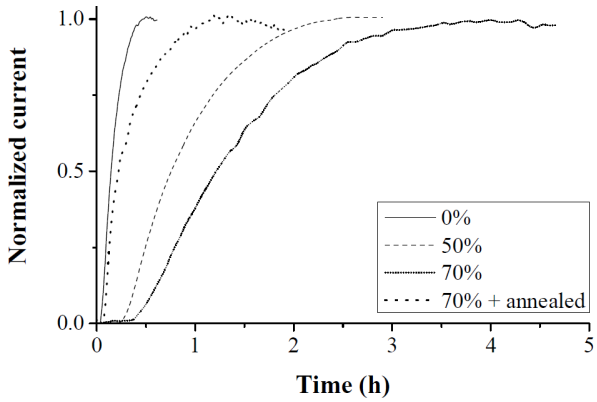

Figure 3.4: Permeation transients of Armco iron in specific cold deformed conditions (0-70%). Figure from [114].

If the trap occupancy is low, the permeation transient can be described by Fick's law, even though the diffusivity is reduced by the trapping. Since both the mobility of hydrogen in lattice and hydrogen release rate from traps is increasing with temperature, trapping is more dominating for diffusion at lower temperature whereas lattice diffusion tends to dominate at very high temperature.

For a material under mechanical stress, the transport of hydrogen is also affected by dislocations. The dislocations create strain fields that can dissolve more hydrogen than the lattice, and the movement of dislocations can therefore interfere with the hydrogen permeation flux [115]. This effect comes in addition to the trapping effect of hydrogen inside the dislocation cores. During straining, the local hydrogen concentration ahead of a crack tip can be influenced by trapping of hydrogen on newly formed dislocations and the transport of both hydrogen trapped in the dislocations and "dragged" with the dislocations. This can give a more or less temporary drop of permeation current upon application of plastic stress [116–118]. The dislocation interactions with the hydrogen permeation flux can lead to an increased sensitivity to the strain rate. For a fast strain rate, the hydrogen can be transported by dislocations away from the areas of highest hydrostatic stress at a higher rate than the diffusion of hydrogen from lattice can compensate for. This can lead to a lower local concentration of hydrogen and observations of lower HE susceptibilities for tests with higher strain rates [102, 119, 120]. At low strain rates, the hydrogen diffusion will compensate for the removal of hydrogen

by dislocations and the HE susceptibility stops being dependent on the strain rate.

In a multi-phase material, the hydrogen diffusivity will be a function of the hydrogen diffusivity in each phase, and the phase fractions, morphologies and orientation with respect to the diffusion direction. This has been considered in several publications both from a theoretical and experimental point of view [121–124]. When the diffusion and solubility of hydrogen inside a phase become negligible compared to the other phase, the phase with low hydrogen uptake can be considered an obstacle to hydrogen diffusion [125]. For ferritic steels, cementite is considered an obstacle to hydrogen diffusion [124, 126, 127]. To account for the effect of a secondary phase with lower hydrogen diffusivity, a tortuosity factor can be estimated to compensate for the increase in diffusion path due to the presence of the secondary phase. Turnbull and Hutchings [121] defined a tortuosity factor, ω, as the ratio between the effective diffusivity in a two-phase alloy to the diffusivity of the main phase, and estimated ω from equations for thermal conductivity in composite media. Forot et al. [124] defined a tortuosity factor, τ as the ratio of the true diffusion path between two parallel planes to the distance between the two planes, and estimated the value of τ by analysing micrographs.

3.3 Hydrogen uptake from CO_2 and H_2S corrosion

Corrosion processes can introduce hydrogen to a metallic material. The absorption of hydrogen is affected by the rate of hydrogen reduction, presence of hydrogen recombination poisons, corrosion products on the surface, and any factor that affects these. The corrosion products can both reduce the hydrogen uptake by making mass-transfer barriers and reducing the corrosion rate by lack of electrical conductivity, but can also increase the hydrogen uptake if cathodic reactions are enhanced on the corrosion products. In addition to supplying hydrogen to the material, the corrosion process can also create pits and trenches that due to their shape act as stress enhancers. This can lead to a higher local hydrogen uptake in these areas. For CO_2 and H_2S corrosion, the dissociation of carbonic acid and H_2S gives an additional source of hydrogen ions, as described in Section 2.1 and 2.2 respectively.

The correlation between corrosion and hydrogen uptake has been studied in several publications. Da Silva et al. [24] investigated the electrochemical hydrogen permeation behaviour of pre-corroded steel samples with $FeCO_3$ or Fe_3C rich layers. Hydrogen was introduced to the sample by the reduction of hydrogen ions at OCP in a CO_2-saturated 3.5 % NaCl solution at room temperature. The resulting permeation curves are shown in Figure 3.5. An $FeCO_3$-rich surface resulted in twice as much hydrogen as a reference wet-ground sample, while an Fe_3C-rich surface gave five times more hydrogen than the wet-ground surface. Cathodic polarisation scans performed in the same test solution showed that the sample with Fe_3C rich surface exhibited higher cathodic current densities than the wet-ground sample, which lead to increased corrosion rate and OCP. The sample with $FeCO_3$ rich surface exhibited lower cathodic current densities than the

wet-ground surface, but the permeation flux was still higher compared to the wet-ground surface.

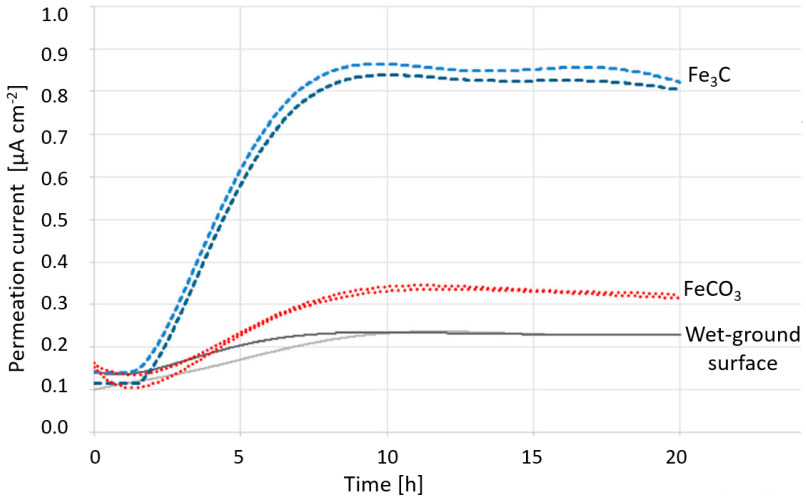

Figure 3.5: Permeation transients for an iron carbonate enriched surface, an iron carbide enriched surface and a wet-ground surface of the same material. Figure adapted from [24].

Alanazi and Al-Enezi [128] also found poor correlation between hydrogen permeation flux and corrosion rate. They studied the hydrogen permeation in a carbon steel exposed to a test solution containing 5 % NaCl and 0.5 % acidic acid, with various partial pressures of H_2S and CO_2. They found no direct correlation between hydrogen permeation flux and corrosion rate, and concluded that the hydrogen permeation flux was more controlled by the partial pressure of H_2S.

The FeS corrosion products have different effects on permeation. For example, Hao et al. [129] observed that mackinawite crystals promoted hydrogen permeation, while pyrrhotite reduced the steady state flux. Huang et al. [130] conducted electrochemical permeation tests on steel samples that were pre-corroded in an H_2S-containing solution. They found that crystalline FeS formed at low pH and low H_2S concentrations, while the formation of mackinawite was promoted with pH (from 3.5 to 5.5) and/or the increase of H_2S concentration (from 0.2 to 20 mM). Interestingly, the hydrogen permeation blocking effect of the surface film increased with increasing H_2S concentration, but was reduced with reducing pH value.

Some studies have shown that corrosion can both give initial hydrogen promoting effects, and contribute to reduced hydrogen permeation with time due to the formation of corrosion products. Wallaert et al. [55] measured the development of hydrogen

concentration in two steels exposed to NACE test TM0284 solution A over a period of four weeks. The diffusible hydrogen concentration peaked within 5 days, then decreased below half the peak value within 20 days, despite increasing corrosion currents. The decreasing hydrogen concentration was attributed the formation of an FeS double layer where S^{2-} and HS^{-} migrate to the steel surface to form the inner layer. Zhou et al. [25] conducted electrochemical hydrogen permeation tests for an X80 pipeline steel exposed to pure CO_2, pure H_2S or a mixture of H_2S and CO_2. Tests were conducted with different H_2S/CO_2 partial pressures. For tests with 1 MPa CO_2 and H_2S partial pressures between 0.001 and 0.1 MPa, the corrosion rate increased with decreasing H_2S partial pressure, and the corrosion products gradually became less rich in FeS and more rich in $FeCO_3$. Regardless of FeS or $FeCO_3$, the corrosion products changed from initially promoting hydrogen permeation to reducing hydrogen permeation as the corrosion progressed.

Yang et al. [131] conducted electrochemical hydrogen permeation experiments in corrosive electrolytes for API X65 carbon steel samples with and without pre-existing corrosion scales. Permeation curves for samples with and without $FeCO_3$ scales are shown in Figure 3.6. The scales were formed in a CO_2 containing solution, and the permeation curves were measured in a H_2SO_4 containing solution under cathodic polarisation to -8 mA cm^{-2}. A sample with loosely attached $FeCO_3$ scales reached higher hydrogen permeation flux than a sample without prior corrosion products. For a sample with compact corrosion scales, the hydrogen permeation flux was lower than the hydrogen permeation flux of the sample without pre-existing corrosion products for the entire test duration.

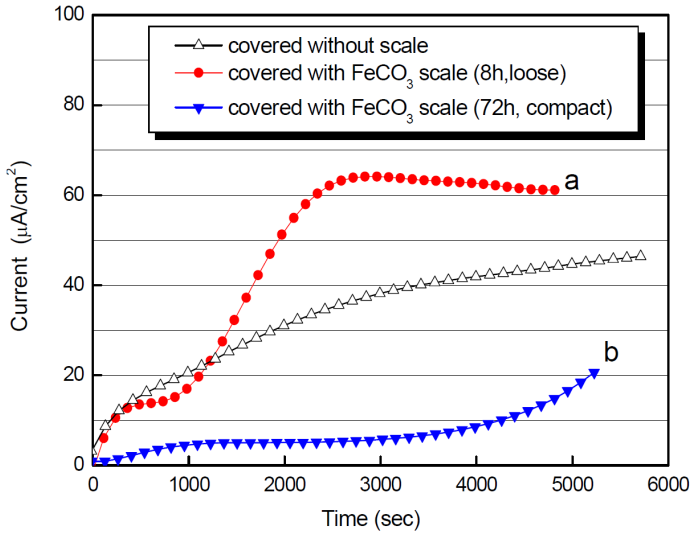

Figure 3.6: Permeation transients for an API X65 carbon steel with and without iron carbonate scales on the surface. The transients were measured in a H_2SO_4 containing solution under cathodic charging to -8 mA cm^{-2}. Figure from [131].

4 Materials and characterization

This chapter describes the methods and results from characterization of the six steel armour wires investigated in the PhD project. The materials were designated letters from A to F. They were taken from coil and were supplied in the same condition as provided for flexible pipes. The production process, chemical composition and mechanical properties of the six wire types were not provided, and a comprehensive characterization of the materials was conducted. The suppliers of the pipes were consulted to ensure that the measured values and properties were within expected range. The following sections describe the materials' chemical composition, phase composition and morphology and mechanical properties, and how the properties and values were determined. In addition, a metallographic analysis was conducted to evaluate the effect of microstructural features on hydrogen uptake and diffusivity.

4.1 Phase morphology and grain size

The materials were examined by Scanning Electron Microscopy (SEM). The samples were hot-mounted in PolyFast, ground to European grit P4000, polished in diamond suspension to 1 µm particles and etched in 2% Nital solution for 5-6 s. The Nital solution was prepared by pouring 2 mL of 67-70 wt% HNO_3 into 100 mL of ethanol. SEM images of the materials are given in Figure 4.1. The materials were deformed ferritic-pearlitic steels with lamellar or spheroidized microstructures. The extent of deformation and description of phase composition is given in Table 4.1. Information about the thermomechanical prosessing of the materials was not provided and the description is therefore based on examination of etched samples in SEM. For the materials with speroidized microstructures, some of the globular cementite had traces of lamellar structure. The microstructures are complex and the grain sizes were not even for cementite-containing grains and ferrite grains. The grain sizes were often hard to determine and the grain size was therefore described by the largest well-defined grains observed in each material, and evaluated for ferrite and cementite-containing grains separately.

Table 4.1: Cementite morphology and extent of deformation in the wire materials.

Material	**Extent of plastic deformation**	**Cementite morphology**
A	Some deformation	Globular
B	Pearlite deformed. Some banding of ferrite.	Globular
C	Some banding and deformation.	Globular
D	Highly deformed grains.	Lamellar
E	Pearlite deformed. Some banding of ferrite.	Globular
F	Ferrite heavily deformed, pearlite less deformed.	Lamellar

Table 4.2: Grain size of the wire materials.

Material	**Grain size ferrite [µm]**	**Grain size cementite [µm]**
A	≤ 14	≤ 36
B	≤ 10	≤ 28
C	≤ 20	≤ 14
D	≤ 7	≤ 24
E	≤ 3	≤ 22
F	≤ 20	≤ 32

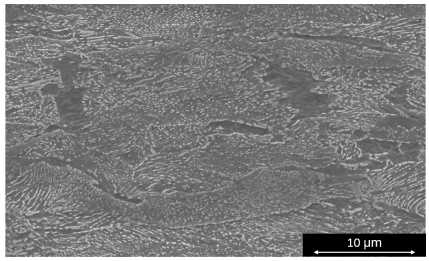

(a) Material A

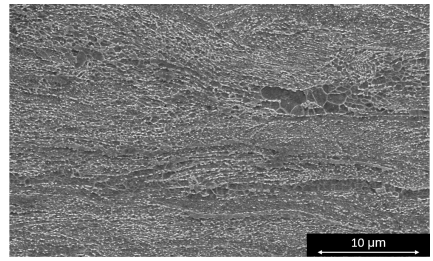

(b) Material B

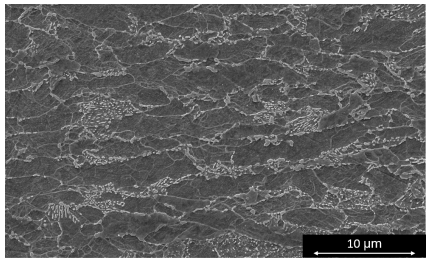

(c) Material C

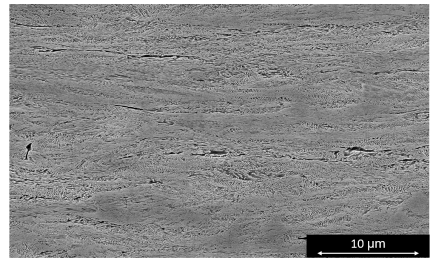

(d) Material D

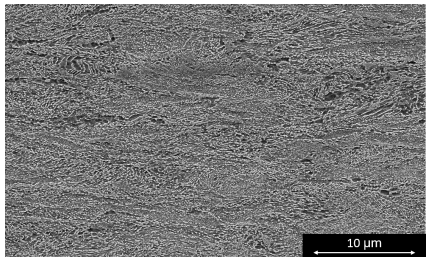

(e) Material E

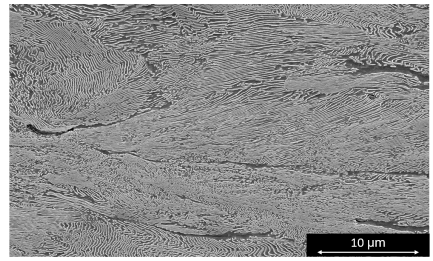

(f) Material F

Figure 4.1: SEM images of the wire materials.

4.2 Chemical composition

The composition of the materials was determined using glow-discharge optical emission spectroscopy (GD-OES). This technique creates a direct current plasma with the surface as cathode and removes the atoms from the surface, layer by layer, by sputtering with argon ions [132]. The removed atoms diffuse into the plasma and are analysed by spectrometry. The instrument GD-Profiler 2™ from Horiba Ltd. was used and the maximum sputtering depth was 150 µm. The GD-OES technique requires vacuum and the minimum sample diameter was 12 mm, where the middle 4 mm was analysed. Since the wires have widths up to 12 mm and bent shape, the samples were embedded and ground before the measurements.

4.2.1 Sample preparation

Samples were made from wire pieces longer than 1 cm that were embedded in a resin. Since the wire materials have a natural curvature they were ground flat to ensure acceptable vacuum conditions for the analysis. The embedded samples were ground with European grit P1000 SiC until an area of at least 4×4 mm^2 was without roughness except from the grinding paper. Then, the samples were ground carefully with European grit P2000 and P4000 SiC paper before polishing in 6 µm diamond suspension. During the grinding steps, the sample was ground until the old grinding lines could not be seen, then turned and ground until only new grinding lines could be seen. A rough estimate of the thickness of material removed was made assuming that a thickness of half the particle size was removed every time new grinding lines were formed. The particle size for the grinding papers are given in Table 4.3. Since the sample was turned once during grinding, the impact can be doubled, and each step is assumed to remove as much material as its particle diameter. This gives a total material thickness reduction of 35 µm.

Table 4.3: Particle size of grinding papers [133].

Step	**Particle diameter [µm]**
P1000	18
P2000	7
P4000	4

After the GD-OES measurements, part of the embedding material was removed to be able to measure the sample thickness to verify the thickness reduction during the grinding process. The samples were either embedded in a non-conducting polymer where the backside was ground to achieve electrical contact for the GD-OES, or embedded in a conductive polymer which was more challenging to remove without grinding the backside. The thickness was measured with a caliper positioned at the transition between un-ground and ground material on the backside of the samples, if possible. The most accurate measurement was conducted for the sample of Material C, which was hardly abraded on the backside. The thickness of this sample was 2.96 mm, i.e. 40 µm

had been removed by grinding, which is in agreement with the estimation made using the particle size of the grinding papers.

4.2.2 Calibration

The accuracy of GD-OES is dependent on calibration with standards of similar composition as the sample, but with limited information about the composition of the wire materials, five steel standards were used for calibration. The standards had carbon contents 0.143, 0.48, 1, 3.29 and 3.408 wt% and varying content of other elements.

4.2.3 Results

The carbon contents measured by GD-OES are shown in Figure 4.2. The materials have decarburized layers, which were also observed in SEM, but the first carbon measurements are high due to contamination. The GD-OES measurements were continued until the carbon content was relatively stable. The average compositions of the last 1 μm measured were considered acceptable estimates for the bulk composition, and are given in Table 4.4. In Paper IV, see Chapter 7.2 Appended papers, the composition was estimated by the average of measurements 99-101 μm from the outer surface.

Table 4.4: Composition of wire materials used in the Ph.D. work based on GD-OES measurements.

Material	**C** [wt%]	**Si** [wt%]	**S** [wt%]	**P** [wt%]	**Mn** [wt%]	**Ni** [wt%]	**Cr** [wt%]	**Al** [wt%]	**V** [wt%]
A	0.501	0.247	0.002	0.003	0.604	0.001	0.011	0.031	0.036
B	0.282	0.223	0.010	0.006	0.733	0.010	0.003	0.035	0.001
C	0.353	0.194	0.007	0.009	0.678	0.013	0.003	0.042	0.002
D	0.830	0.331	0.005	0.005	0.683	0.005	0.002	0.041	0.050
E	0.618	0.225	0.002	0.007	0.729	0.009	0.032	0.037	0.001
F	0.651	0.240	0.009	0.002	0.630	0.060	0.025	0.003	0.001

Material	**Pb** [wt%]	**N** [wt%]	**Ti** [wt%]	**Sn** [wt%]	**Cu** [wt%]	**Co** [wt%]	**Mo** [wt%]	**B** [wt%]
A	0.050	0.009	$<10^{-4}$	N.D.	N.D.	N.D.	0.001	$<10^{-4}$
B	0.065	0.020	0.002	N.D.	$<10^{-4}$	$<10^{-4}$	0.001	$<10^{-4}$
C	0.065	0.219	0.002	$<10^{-3}$	0.001	N.D.	0.001	$<10^{-4}$
D	0.065	0.099	0.004	0.001	$<10^{-4}$	N.D.	0.002	$<10^{-3}$
E	0.050	0.014	$<10^{-4}$	N.D.	N.D.	N.D.	$<10^{-3}$	$<10^{-4}$
F	0.040	0.009	N.D.	N.D.	$<10^{-3}$	0.001	$<10^{-4}$	$<10^{-4}$

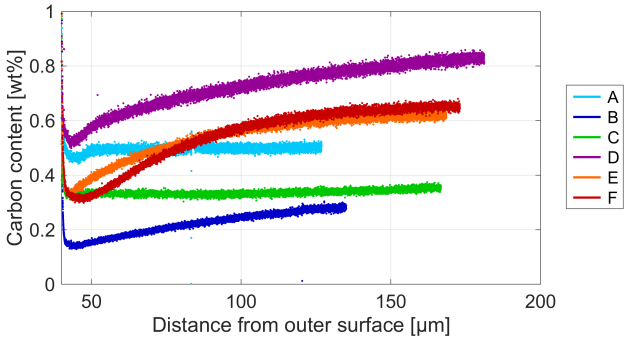

Figure 4.2: Carbon contents in decarburized layers of the six materials A-F.

4.3 Mechanical properties

The mechanical properties were determined by Slow Strain Rate Tests (SSRT) of smooth samples and Vickers hardness measurements (HV_{10}) in the cross-section. The ultimate tensile strength (UTS), yield strength (YS) and plastic strain-to-failure (Ep) were measured with tensile tests at strain rate 10^{-6} s^{-1}. Ep was determined as defined in NACE Standard TM0198-2016 [134]. The stress-strain curves were published in the conference paper found in the Appended papers, Chapter 7.2.

Table 4.5: Mechanical properties of the wire materials.

Material	**Hardness HV_{10}**	**YS [MPa]**	**UTS [MPa]**	**Ep [-]**
A	331 ± 14	871	1009	0.115
B	290 ± 10	805	847	0.157
C	257 ± 4	616	744	0.152
D	453 ± 16	1408	1622	0.094
E	386 ± 8	1097	1260	0.108
F	384 ± 6	1252	1408	0.099

4.4 Metallographic study of phases

For evaluation of diffusivity of hydrogen and the trapping of hydrogen on grain boundaries, the mean free path between cementite particles, λ_p, the mean true spacing for lamellar materials σ_0 and specific interfacial area, or ferrite-cementite interfacial area, S_v, were estimated using the method described by Johnson and Krauss [135]. The calculations depend on the number of particles intercepted by a test line, N_p, or number of cementite

platelets intersected per unit length, n, and the volume fraction of cementite, f. f was calculated with the lever rule, assuming all carbon is located in cementite, Fe_3C. Carbon can also exist in solid solution and in other types of carbides than cementite, and this estimate is therefore considered a maximum value. Since the materials can contain both globular and lamellar cementite, the number of cementite intercepts N per test line was used instead of n and N_p. For each material, N was determined by examination of four images of the middle of the width-length plane of the wires and four images in the middle of cross-sections. Five vertical and five horizontal test lines were measured per image, i.e., 20 lines were used to find the average number of cementite intercepts per test line in the thickness and length directions, and 40 lines were used to find the average number of cementite interceptions in the width direction. The value of N in the three directions and corresponding standard deviation is shown in Figure 4.3. The SEM images used had magnifications from 5000 to 50000 X. For the materials with the finest carbide particles, lamellas, and grain size, the higher magnifications were used in order to see the features clearly. Lower magnifications were used for the materials with larger grain size since the number of carbide particles and platelets varies from grain to grain, and the accuracy of the measurements is improved when more grains are crossed by the test line. All materials were evaluated at 20000 X and at least one other magnification. The S_v, λ_p and σ_0 were then calculated from the following equations [135]

$$S_v = 4N \tag{4.1}$$

$$\lambda_p = \frac{1-f}{N} \tag{4.2}$$

$$\sigma_0 = \frac{2}{S_v} \tag{4.3}$$

The tortuosity of the hydrogen diffusion path, τ was determined by the length of the diffusion path between two planes normal to the thickness direction, L, divided by the distance between the two planes L_0, as defined by Forot et al. [124]

$$\tau = \frac{L}{L_0} \tag{4.4}$$

In the electrochemical hydrogen permeation experiments, hydrogen diffused in the thickness direction of the wires, and the tortuosity was therefore only studied in this direction. The principle of the measurements is shown in Figure 4.4, where the red line represents L and L_0 is the width of the image. The micrograph examination conducted to determine τ is described in detail in Paper I. The results of the metallographic study are given in Table 4.6.

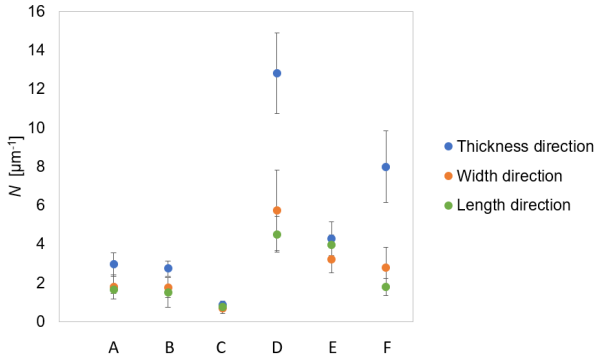

Figure 4.3: Cementite intercepts per length test line with error bars of one standard deviation.

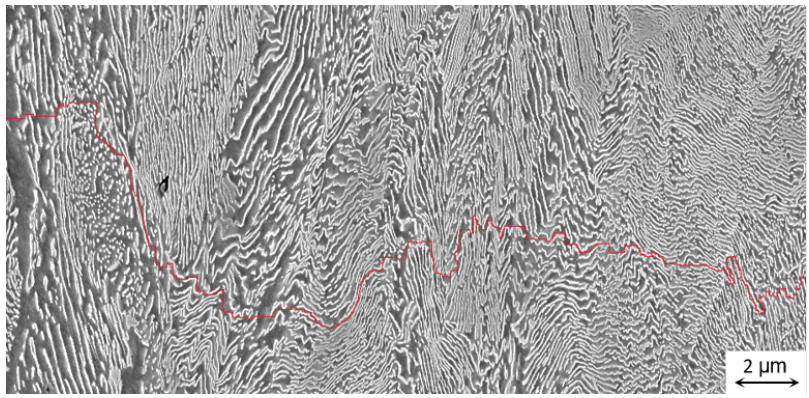

Figure 4.4: Example of line drawn to estimate the tortuosity of the hydrogen diffusion path. The image is cropped and magnified to make the red line more visible.

Table 4.6: Metallographic study of the six wire materials.

Material	τ [-]	S_v [µm^{-1}]	λ_p [µm]	σ_0 [µm]
A	1.122 ± 0.036	8.521 ± 1.901	0.434 ± 0.097	N.A.
B	1.055 ± 0.010	8.022 ± 2.975	0.480 ± 0.178	N.A.
C	1.056 ± 0.022	3.066 ± 2.176	1.239 ± 0.879	N.A.
D	1.669 ± 0.266	30.761 ± 2.421	N.A.	0.065 ± 0.005
E	1.158 ± 0.015	15.237 ± 1.345	0.240 ± 0.021	N.A.
F	2.035 ± 0.344	16.758 ± 3.316	N.A.	0.119 ± 0.024

5 Experimental methods

This chapter presents the experimental methods used for measuring the hydrogen uptake of the materials and investigating the effect of hydrogen on the mechanical properties of the materials. The hydrogen uptake was measured by electrochemical hydrogen permeation tests. One set of tests was conducted with hydrogen entry from cathodic polarisation and another set of tests was conducted with hydrogen produced by corrosion of the sample. The effect of hydrogen on mechanical properties was investigated by slow strain rate tests for macroscopic samples, where the results of tests conducted under cathodic polarisation were compared to the results of tests conducted in air.

The principles of the electrochemical hydrogen permeation tests and slow strain rate tests are described in Section 5.1 and 5.2, respectively. The preparation of samples for electrochemical hydrogen permeation experiments is described in Section 5.1.1, and details particularly considerations regarding using embedded samples. Section 5.1.2 describes specifics related to conducting electrochemical hydrogen permeation tests in the simulated corrosive environment used in Paper II.

5.1 Electrochemical hydrogen permeation test

The hydrogen uptake and diffusion coefficients of the wire materials were measured using an electrochemical hydrogen permeation cell, similar to the design developed by Devanathan and Stachurski [136]. Standards ASTM G148 [112] and ISO 17081 [94] were used as guidelines. The permeation cell consists of two chambers placed on opposite sides of a disc-shaped sample. On one side, the sample is kept in a passive environment to create a low anodic current on the sample surface and ensure that any hydrogen diffusing from the bulk of the sample to this surface is immediately oxidized. This side of the sample and the corresponding chamber are usually called the anodic side, (hydrogen) detection side or (hydrogen) exit side. The oxidation of hydrogen increases the current on the hydrogen exit side and by subtracting the passive current achieved in the absence of hydrogen permeation, the hydrogen permeation flux through the sample is found. The other side of the sample is exposed to the test environment and can be cathodically polarised if desired. This side is usually called the cathodic side, (hydrogen) charging side or (hydrogen) entry side. When hydrogen is introduced by corrosion, it can also be called the corrosion side.

A sketch of the permeation cell is shown in Figure 5.1. The electrolyte on the hydrogen exit side was 0.1 M NaOH purged with N_2 gas to remove oxygen from the compartment. Two potentiostats are used: One for polarising the hydrogen exit side of the sample and one for either polarising the hydrogen entry side or measuring the OCP and corrosion rate (through linear polarisation resistance (LPR)) when hydrogen is introduced by corrosion. For tests with gaseous hydrogen charging, this potentiostat is not needed.

The potentiostats use separate counter electrodes (CE) and reference electrodes (REF), but the sample is the working electrode (WE) for both.

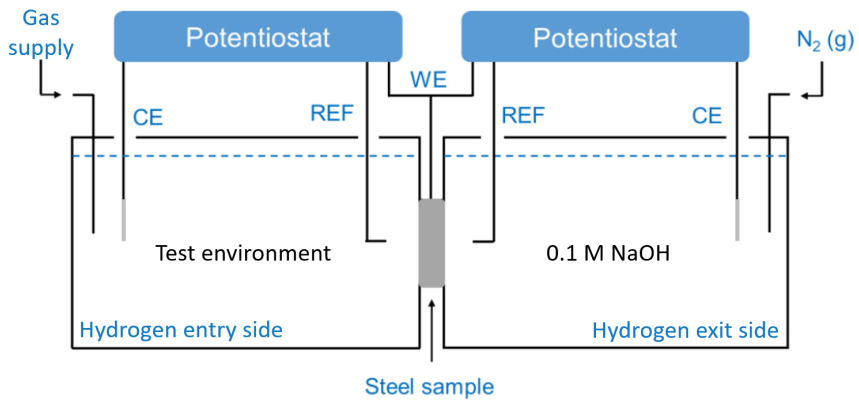

Figure 5.1: Sketch of the electrochemical hydrogen permeation test cell. Figure adapted from [137].

The hydrogen permeation flux is usually recorded in an initially hydrogen-free sample that is charged with hydrogen on the hydrogen entry side until a steady-state permeation flux is achieved. This is referred to as a rising transient. Then, the hydrogen charging can be stopped or altered to create a new transient towards a new steady-state. In the first rising transient of a hydrogen-free sample, the permeation is affected by the presence of both irreversible and reversible traps. For tests where hydrogen is introduced by cathodic polarisation, a rising transient can be followed by anodic polarisation to remove the diffusible hydrogen from the sample. This is called a decay transient. A rising transient and a decay transient are shown in Figure 5.2. When the hydrogen has been removed from the sample, the hydrogen charging can be started to enable the recoding of a new rising transient, which will only be affected by lattice hydrogen and hydrogen in reversible traps. The difference between the first and second transient indicates the presence of irreversible traps. The effective diffusion coefficient and hydrogen uptake are calculated from the permeation flux using Fick's first and second law, see Equation (3.9) and (3.10), with appropriate boundary conditions for the environment chosen. The calculations for effective diffusion coefficient and hydrogen uptake is described in detail in Paper I.

During the electrochemical hydrogen permeation test, hydrogen can be introduced to the sample at OCP or by galvanostatic or potentiostatic polarisation. Using potensiostatic polarisation on the cathode side gives better control of what reactions are occurring on the surface. However, potensiostatic control is more dependent on a stable reference electrode as a fluctuation in reference potential will affect the applied potential of the working electrode. Galvanostatic charging controls that the same current is supplied to

the surface, but some fraction of the current may go to other processes than hydrogen reduction. If the surface on the hydrogen entry side is covered in oxides or contaminants, the reduction of these may compete with the hydrogen reduction reaction. The rate of hydrogen reduction may therefore be low in the beginning and increase as the oxide is removed before it becomes more stable. The build-up of the hydrogen concentration on the hydrogen entry side will be slow at first, then faster as a higher fraction of the current goes to hydrogen reduction. The oxides on the hydrogen entry side can be removed by prolonged hydrogen charging. For cathodic charging in 0.1 M NaOH, Bruzzoni and Garavaglia [138] found that a steel surface needed 100 h charging at -10 mA cm^{-2} to become oxide free, while Zakroczymski and Szklarska-Smialowska [139] found that the effect of oxide on permeation was removed after 90 h of charging at -9 mA cm^{-2}. The hydrogen permeation flux recorded while oxide is removed is not suitable for measuring the hydrogen diffusion coefficient, since the boundary conditions are changing with time, but a following decay transient can be suitable. The main requirement is that the boundary conditions of the systems during the decay must be known.

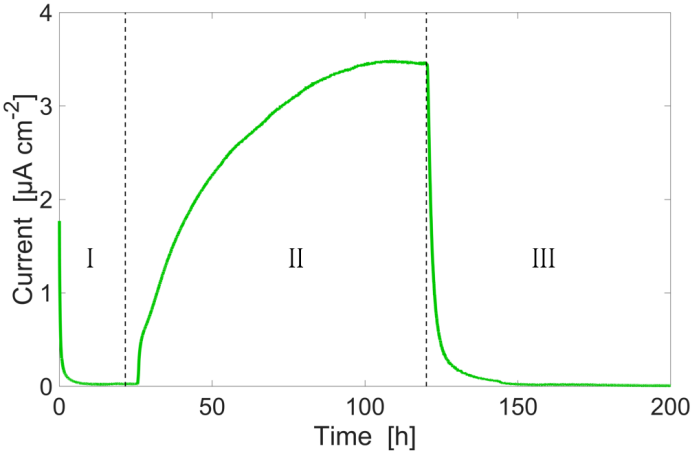

Figure 5.2: Example of rising and decay hydrogen permeation transients. In region I, the anodic current is stabilised. Region II is a rising transient measured while the hydrogen entry side is polarised to -12 mA cm^{-2}. Region III is a decay transient measured while both sides of the sample are anodically polarised.

5.1.1 Embedding samples

The wire materials have complex microstructures and it was desired to conduct the electrochemical hydrogen permeation experiments on samples that keep most of the original wire thickness. Only the decarburized layers were desired removed. Standards ASTM G148 [112] and ISO 17081 [94] recommend minimum 10:1 radius to thickness ratio

for disc-shaped samples, to guarantee one-dimensional diffusion through the thickness. This was un-practical to fulfil without removing most of the thickness and the samples were therefore embedded.

The embedding was required to be well-adhering to the steel surface to avoid any short-cuts for diffusion in the sample, and the adhesion would have to stay satisfactory also after the application of a palladium coating on the steel surface. An embedded and palladium coated sample is shown in Figure 5.3. The palladium coating was applied to ensure that diffusing hydrogen oxidises instantly as it reaches the surface of the hydrogen exit side of the sample. When exposed to 0.1 M NaOH, iron forms oxides that impedes hydrogen diffusion, and the effect is more severe with time as the thickness of oxide increases. The coating was applied by electrodeposition using a procedure proposed by Bruzzoni [140] further developed by Husby et al. [141]. After the samples were coated with palladium, the samples were heated to 120 °C in a heating cabinet for at least 16 h to remove any hydrogen absorbed by the steel during the Pd-coating process. This procedure was conducted after the samples were embedded, since the palladium coating is fragile and was only desired on the hydrogen exit side. Therefore, the embedding was required to withstand the 120 °C temperature.

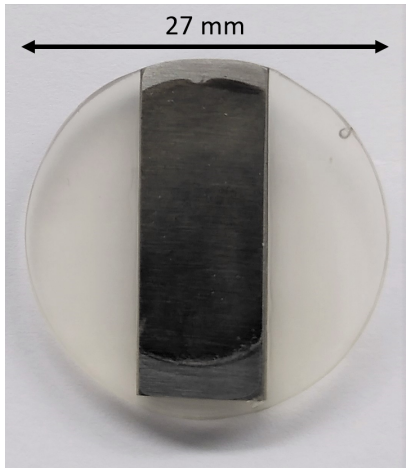

Figure 5.3: Pd-coated and embedded permeation test sample.

The sample preparation started with straightening the most bent wires with a roller straightener before cutting the wires to pieces with about 2.8 cm length. The pieces were ground flat with SiC paper, washed in acetone and sonicated in ethanol. The corners of the wire pieces were ground so the wire pieces fitted a mounting cup with diameter 3 cm. The wire pieces were embedded in the light-curing resin Technovit®LC 2000, mixed with the additive “Inside Cure” to ensure good adhesion between the steel and the polymer. The curing was conducted in a chamber with blue light until the

polymer was cured, ca. 30 min. The exposed area of the sample when installed in the permeation cell was 2.26 cm^2 for the samples made of the widest wire materials and 1.72 cm^2 for the samples made of the narrowest wire materials. This is not in line with the minimum 10:1 radius-to-thickness ratio for circular samples, but this criterion is less stringent for materials with geometrical limitations, e.g. components [112]. After mounting, the two sides of the sample were ground with European grit P1200 SiC paper and the sample heated at 120 °C in a heating cabinet overnight. Sites where the adhesion between the steel and polymer was weak were visible after heating and only defect-free samples were coated with palladium and used for electrochemical permeation tests. The samples with satisfactory embedding after the first heat-treatment were usually also in good condition after the palladium coating process and subsequent heat treatment.

The polymer was verified to be completely dense to ions at ambient temperature by casting a sample of only polymer, inserting it in the Devanathan-Stachurski cell, filling the compartments with 0.1 M NaOH and measuring the lack of electrical contact between the counter electrodes. For permeation tests conducted at 60 °C with hydrogen introduced by cathodic polarisation, the current tended to rise faster than predicted by Fick's law and in some experiments, the two potentiostats lost the ability to polarise the sample independently. Post-examination of the samples showed that cavities were formed in-between the polymer and steel in these tests. Cavities were also sometimes seen on samples that were tested several times or for long periods. The issues with embedding integrity lead to the decision that tests would not be conducted longer than twenty days and the temperature was kept at 25 °C. New samples were made for each experiment, except on one occasion which is detailed in Paper II. This sample displayed a good integrity after the second test and the results were established to be reproducible by repeating the experiment using a sample that had not been used before.

5.1.2 Hydrogen uptake in corrosive environment

The corrosive environment used in the permeation tests of Paper II was designed to avoid extensive corrosion product films on the surface. Flexible pipes are normally covered with protective corrosion products of iron carbonate and sulphides but the protective films can be weakened or prevented from forming when the supersaturation of iron is decreased. This can happen by for example continuous water condensation, partial inhibition or ingress of seawater. The environment was sensitive to changes in experimental parameters, and this section describes experimental challenges with hydrogen measurements in the corrosive environment that were not elaborated in Paper II. A sketch of the test rig for electrochemical hydrogen permeation experiments with a corrosive environment on the hydrogen entry side is shown in Figure 5.4.

The electrolyte in the corrosion compartment of the permeation cell consisted of modified ASTM D1141-90 electrolyte (no NaF, $CaCl_2$ and KBr) bubbled with different ratios of N_2, CO_2 and H_2S at 25°C and ambient pressure. The gas flow into the corrosion

compartment was ca. 600 mL h^{-1}. The electrolyte was continuously pumped in and out of the compartment at flow rate 25-35 mL h^{-1}, to keep the iron concentration in the cell low. The corrosion rate (with LPR), OCP, pH and iron content in the solution were recorded, and the details for these measurements are given in Paper II. In addition to the tests presented in Paper II, several trial tests were conducted to find a suitable test program for the wire materials. The trial tests were conducted with other gas compositions than the program used in Paper II and the corrosion rate, OCP, pH and iron content were not recorded for the trial tests.

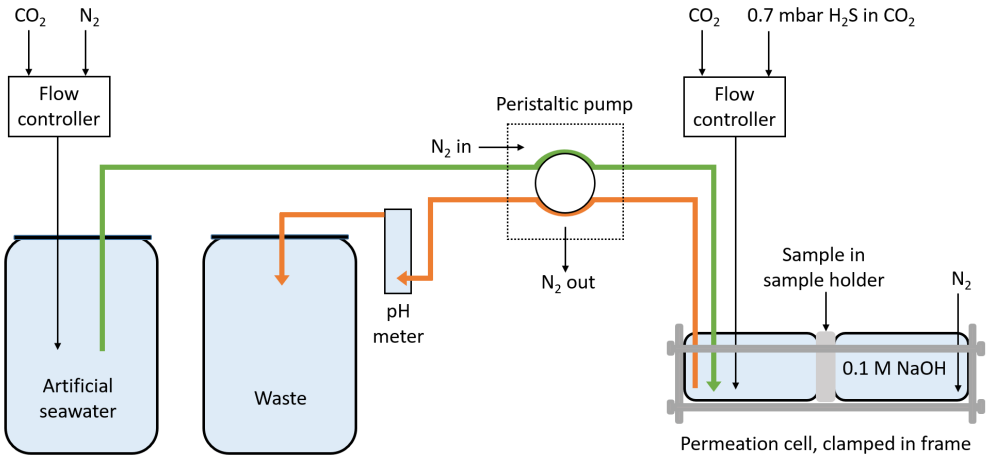

Figure 5.4: Sketch of the electrochemical hydrogen permeation tests used in Paper II.

The first challenge was related to the observation that the current created by the hydrogen permeation flux in pure CO_2 environment was in the same order of magnitude as the stabilization current. As mentioned, the passive current on the hydrogen exit side must be stabilized before the hydrogen permeation flux can be introduced so a correct subtraction of baseline current can be conducted. It is common to start the hydrogen charging when the stabilisation current has decreased beneath a certain value. The decided value should be much lower than the expected steady-state current during hydrogen charging. Hence, if the passive current decreases during the permeation test, it will not affect the test results significantly. For the tests in Paper I, where hydrogen was introduced by cathodic polarisation, one day of stabilisation was sufficient to reach an acceptable stabilisation current. For tests with lower current induced by the hydrogen permeation flux, a further decrease in stabilisation current during the experiment can give erroneous results. Figure 5.5 shows two tests conducted for Material B, which have not been published and are not included in any draft papers. In the first test, drawn in blue, the current appears to be stable after 15 h and the corrosive environment is added on the hydrogen entry side after about 18 h. In a second test for the same material, drawn in red, the stabilisation time was increased to about 72 h. The current

appeared to be stable after 15 h, but it decreased by more than 0.5 µA cm^{-2} over the next 20 h. If the electrolyte was added after 15 h, the baseline current subtraction would have been too high, and the hydrogen permeation flux underestimated. This may have happened for the test drawn in blue. To reduce the risk of subtracting a too high baseline, the stabilization period was increased to 72 h for the permeation tests with hydrogen introduced by corrosion.

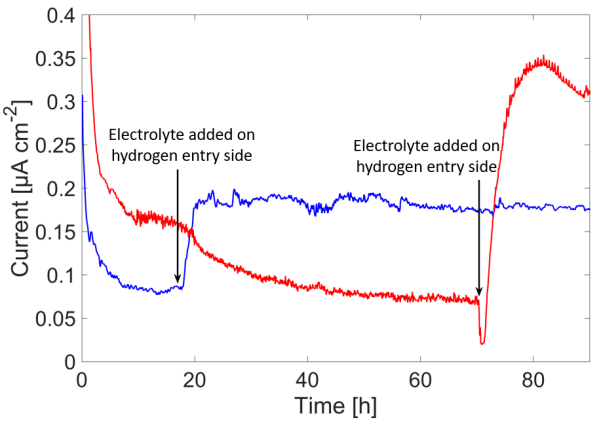

Figure 5.5: Effect of stabilisation time on hydrogen permeation results, illustrated by two permeation curves with different stabilization times for the same material.

The second challenge was related to small stops in gas inlet. The gas pressures of the tests presented in Paper II were adjusted without stopping the flow of gas into the corrosion compartment. In the initial trial tests, the gas was briefly stopped (seconds to minutes) when the H_2S gas composition was altered. For steps with H_2S exposure, the hydrogen permeation current decreased immediately in response to these short stops. Figure 5.6 shows a trial test for Material E, where the gas supply was briefly stopped, and the test published in Paper II without stops. For the test with short stops, the time lag from H_2S was added until the permeation current increased was several hours longer than it was for the test without short stops, and the permeation current was on several occasions decreasing due to short stops. The test without the short stops exhibited a smoother permeation curve. The short stops were avoided after the H_2S pressure was set to 0.4 mbar, and the permeation curve reached a higher current after this than the test exposed without stops in gas supply. Interestingly, the temporary plateau currents reached when the H_2S pressure was reduced are relatively similar for the two tests. This indicates that the surfaces of the two samples have similar effect on hydrogen permeation, and that the short stops in gas supply are mainly affecting the hydrogen profile in the sample, i.e. resulting in longer time to reach a steady state permeation current, as discussed in [142]. The observation described above is the reason why the tests were executed without stopping the gas before a change in gas composition. The

effect of gas changes was also seen in a clogging incident that happened during the test for Material D. This incident is described in detail in Paper II.

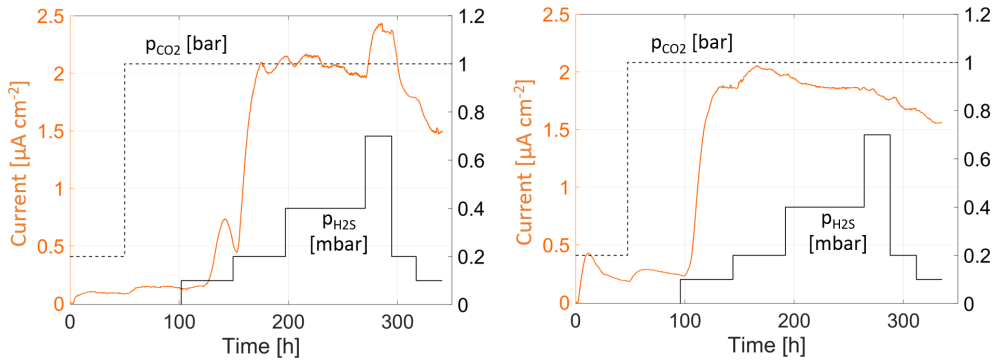

(a) Short stops in gas supply

(b) No stops in gas supply

Figure 5.6: Electrochemical hydrogen permeation tests with and without short stops in the gas supply (Material E).

5.2 Macro-scale slow strain rate tensile test

To evaluate the hydrogen embrittlement susceptibility of the wire materials, SSRT was conducted with basis in ASTM G129 [143] and NACE TM0198 [134]. In SSRT, the sample is slowly stretched at a constant strain rate until it fails. This can be executed by calculating the nominal elongation rate corresponding to the strain rate and pulling one end of the sample at this elongation rate. The tests are conducted in the environment of interest, in which hydrogen may enter the sample, and in an environment where hydrogen may not enter the sample for comparison. The tests are conducted at strain rates that typically gives failure within a few days, and the method is considered quick and simple for comparing the EAC susceptibility of materials. In the work conducted for this thesis, the SSRT method was used to investigate HE susceptibility in particular. Tests were conducted for samples exposed to a 3.5 % NaCl solution while cathodically polarised to -1.1 or -1.4 V vs. Ag/AgCl, sat. KCl. Reference tests were conducted in air.

For tests in electrolyte, an environmental chamber can be attached to the sample or be attached to the loading frame, and hence enclose the sample holder parts. A schematic and photograph of a sample with an environmental chamber is shown in Figure 5.7. For samples with a stress-concentrator, e.g. notch or fatigue-induced pre-crack, the fracture initiation point will be near the stress-concentrator and an environmental chamber can be placed around the defect. This allows the gripping mechanism to consist of parts that are not inert to the environment. For a smooth sample, the entire gauge section should

be exposed to the environment and a chamber attached to the load frame may be more suitable. This gives a higher exposed area than in a small chamber, and consequently a higher absolute current required for polarisation.
The SSRT method is sometimes critized due to the destructive and accelerated nature of the test. Some go as far as claiming that "If we believe the results of slow strain rate tests, we would never cathodically protect steel" [45]. It is therefore stressed that the results are not necessarily representing the service performance of the material, but can be used for detection of environmental interactions with a material, and for screening and comparative evaluation of the effects of metallurgical and environmental variables on sensitivity to environmental cracking [143].

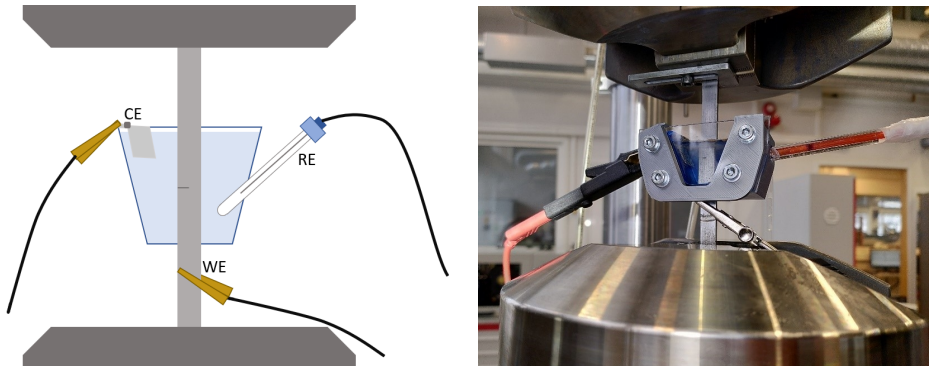

Figure 5.7: Sketch and photograph of a notched sample installed in the tensile rig with the environmental chamber attached.

The HE susceptibility can be evaluated by comparing parameters measured for tests in the environment of interest and for tests in inert environment, e.g. air. Parameters that are commonly compared in the two environments include:

- Strain-to-failure or elongation-to-failure
- Reduction in area, estimated by examination of the fracture surfaces
- Maximum stress
- Area bounded by nominal stress-elongation curve representing the fracture energy

In addition to quantitative parameters, the EAC susceptibility can also be evaluated qualitatively by comparing the fracture surfaces produced under exposure to the test environment with fracture surfaces produced in inert environment, and the formation of secondary cracks.

For notched samples, the notch tensile strength, NTS, plane strain threshold stress intensity, K_I, and threshold stress intensity, K, can also be measured. Measurements of

K_I and K are most suitable when the onset of cracking can be determined. For tests under cathodic polarisation, the crack initiation point can be difficult to detect due to the bubble formation on the surface. The crack initiation point can also be challenging to determine when the cracking starts internally. If the test is imaged at a high frequency, the displacement of material may be calculated by digital image correlation (DIC). This requires features on the surface that an algorithm can recognize and track from image to image. If the displacement data has sufficient quality, it can be used for analysing the deformation of the material. A simpler and more practical approach to investigating the displacement is to measure the crack mouth opening displacement (CMOD) by a gauge clip, and calculate the crack tip opening displacement (CTOD), but this is usually not possible for tests conducted in an electrolyte. In Paper III, the CMOD and CTOD were estimated from images of the tensile tests which were analysed by DIC. An image from a tensile test is shown in Figure 5.8. Some attempts were conducted with painted dots on the surface, but the paint was usually damaged during testing under cathodic polarisation. The surfaces were instead scratched up to create a pattern that could be followed by DIC. However, a challenge was the formation of bubbles on the surface of the sample and attaching to the glass of the environmental chamber. By imaging at the highest rate possible with the equipment available (10 images per second) and merging several images together, the effect of bubble formation and movement could sometimes be mitigated. For other tests, the bubble formation was too severe and DIC could not be applied. The image in Figure 5.8 is merged from several images.

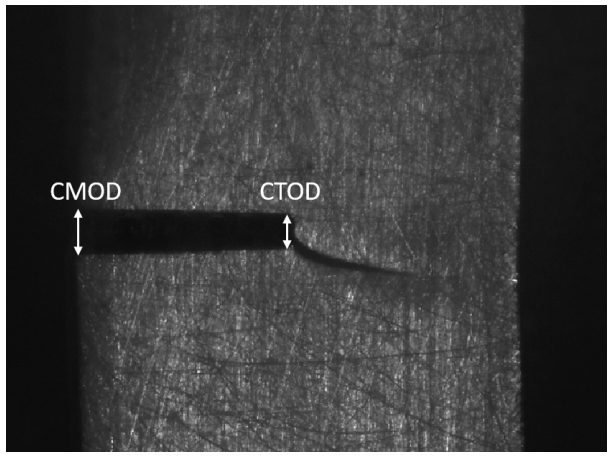

Figure 5.8: Image of crack from a tensile test. The crack mouth opening and crack tip opening are indicated by the arrows.

An interesting difference between the two standards is the calculation of plastic elongation in ASTM G129 [143] and plastic strain to failure in NACE TM0198 [134]. The difference is illustrated in two fictional curves in Figure 5.9. In ASTM G129, the plastic elongation is approximated to be the difference in crosshead displacement from the onset of specimen

yielding to crosshead displacement at specimen fracture. The plastic strain-to-failure is measured by extrapolating a line with the same slope as the linear stress-strain region from the fracture strain to zero stress, and subtract the interception of the linear stress-strain region to zero stress. For the two curves in Figure 5.9, the plastic elongation ratio calculated according to ASTM G129 [143] is the same, while the plastic strain-to-failure calculated according to NACE TM0198 [134] is higher for the curve that fractured at a lower stress. In Paper IV, the the plastic elongation ratio was used to evaluate the hydrogen embrittlement susceptibility, but since the elastic region was affected by different sample holders, the plastic strain-to-failure parameter would have been more suitable. In Section 4.3 and Paper I-III, the plastic strain-to-failure was used to describe the ductility of the samples.

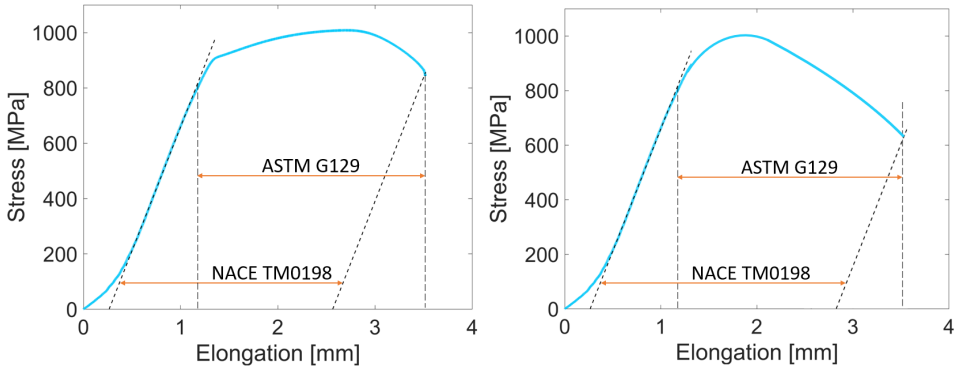

Figure 5.9: Reduction of ductility in ASTM G129 [143] and NACE TM0198 [134].

6 Summary of papers

Four scientific papers have been written about the investigation of hydrogen uptake, corrosion and EAC for the six armour wires. Paper I-III are journal papers while Paper IV is a conference paper. Electrochemical hydrogen permeation experiments were discussed in Paper I and II, while SSRT was discussed in Paper III and IV. Summaries of the papers are given in the sections below.

6.1 Paper I

Hydrogen uptake and diffusivity in steel armor wires with different chemical composition, carbide distribution, grain size, and degree of deformation

The main objective of Paper I was to find the diffusion coefficients of the tensile armour wires and measure the diffusible hydrogen uptake in the wires during cathodic polarisation by electrochemical hydrogen permeation experiments, and find correlations between these properties and the microstructure. All the six tensile armour wires were included in this study.

A metallographic study was conducted where the number of ferrite-cementite interfaces per length was measured and used to estimate the ferrite-cementite interfacial area, mean free path between cementite particles and the mean true spacing for lamellar materials.

Electrochemical permeation tests were conducted with 0.1 M NaOH on both the hydrogen entry and hydrogen exit side of the samples. Hydrogen charging was conducted galvanostatically at -12 mA cm^{-2} and two rising transients and decay transients were measured. The anodic side was polarised to +340 mV vs. Ag/AgCl, sat. KCl, and the cathodic side was also polarised to this potenital during the initial stabilization of the anodic side and during the decay transients. The wire materials were embedded in a resin to form disc-shaped samples.

The rising hydrogen permeation transients were impeded by oxide formed on the hydrogen entry side, but the decay transients were relatively reproducible and used for estimating the hydrogen diffusion coefficients. The hydrogen diffusion coefficients tended to decrease with the ferrite-cementite interfacial area, but the trend was not completely consistent. The correlation between ferrite-cementite interfacial area and diffusivity indicates significant hydrogen trapping on the ferrite-cementite interfaces. The hydrogen permeation flux tended to be higher for materials with smaller grain size, but this trend was not reflected in the diffusion coefficients. The most significant trend in the hydrogen uptakes was that the materials with least deformation had the lowest hydrogen uptakes, which can be related to hydrogen trapping on dislocations and vacancies formed

by deformation.

6.2 Paper II

Hydrogen uptake during active CO_2-H_2S corrosion of carbon steel wires in simulated annulus fluid

The purpose of Paper II was to estimate the hydrogen uptake of the steel armour wires in a corrosive CO_2/H_2S environment where protective film formation was not favourable. All materials were tested, but only results for Materials A-E were included in the paper.

The hydrogen permeation flux was measured in an electrochemical permeation cell where the sample was exposed to the corrosive environment on the hydrogen entry side while the hydrogen detection side was exposed to deaerated 0.1 M NaOH and polarised to +340 mV vs. Ag/AgCl, sat. KCl. The electrolyte on the hydrogen entry side was modified artificial seawater (ASTM D1141-90) bubbled with CO_2 and H_2S at OCP. The experiments consisted of several steps with different gas compositions, which gave several hydrogen permeation transients that showed how changes in surface condition influence the hydrogen uptake. Material F was also tested, but the tortuous nature of the hydrogen diffusion path in this material prevented steady-state permeation within the time frame of each step and the results were therefore inconclusive.

In step 1 of the test program, the gas consisted of 0.2 bar CO_2 in N_2. After $\sim$ 48 h, the partial pressure of CO_2 was increased to 1 bar and the N_2 bubbling stopped. In the third step, H_2S was added, and the rest of the steps had between 0.1 and 0.7 mbar H_2S in 1 bar CO_2. The electrolyte was continuously refreshed to maintain a low dissolved iron concentration in the electrolyte ($<$ 10 ppmw). The corrosion products on the sample surface were characterized by SEM, XRD and energy-dispersive X-ray spectroscopy, and the weight of corrosion products attached to the surfaces was measured by stripping the samples. The tests were conducted at ambient pressure and temperature 25°C.

Reversible hydrogen uptakes below 0.2 ppmw were measured under pure CO_2 corrosion for materials A, C and E, and below 0.6 ppmw for Material B. Ferrite was dissolved preferentially during pure CO_2 corrosion, while carbides were retained. XRD did not detect $FeCO_3$. For the lamellar materials, D and F, the hydrogen uptake during pure CO_2 corrosion could not be determined. This is most likely due to the high tortuosity of the hydrogen diffusion path in these materials, which decreases the permeation flux. The hydrogen concentration on the hydrogen entry side will cause a smaller permeation flux in a tortuous material than a material without tortuosity. The absence of a defined increase in permeation flux during exposure to CO_2 for materials D and F is therefore considered to be caused by insufficient accuracy in the test method, and not the absence of a hydrogen permeation flux. Under exposure to CO_2 and H_2S, the hydrogen uptakes ranged from $\sim$0.2-1.4 ppmw, but the hydrogen

uptake measured for Material F is slightly uncertain since the hydrogen permeation flux was still increasing when the partial pressure of H_2S was lowered towards the end of the experiment. This is the main reason why Material F was not included in the paper.

For most of the materials, the hydrogen uptakes decreased as retained carbide accumulated on the surface, even though the corrosion rates were increasing. Cementite is mainly a site for cathodic reactions in steels, and the hydrogen diffusivity and solubility in cementite are low. Based on this, it was proposed that the hydrogen uptakes are reduced with increasing area of retained carbide because the hydrogen adsorbed on carbides located far from ferritic grains has limited opportunities for absorption into the steel. This positive effect of retained carbides on hydrogen uptake was observed during pure CO_2 corrosion, and appeared to still be relevant when small amounts of H_2S was added. Material B was one of the materials with highest hydrogen uptake, and had the lowest and most stable corrosion rate during CO_2 corrosion. Since Material B has the lowest carbon content and the carbide is in the form of fine round particles, the area of retained carbides is expected to be smaller for Material B than the other materials. The XRD measurements confirmed that all materials formed retained carbides, but Material B had a much lower film weight, which suggests that Material B had a lower ability to retain carbide than the other materials. Apart from Material B, the results indicated higher hydrogen uptake with higher carbon content, which can be related to hydrogen trapping on ferrite-cementite interfaces. The hydrogen uptake decreased with time towards the end of each step for most of the materials, showing that the surfaces became less penetrable for hydrogen during exposure to the test environment. When the H_2S partial pressure was reduced towards the end of the test, the hydrogen uptakes decreased substantially, indicating that the hydrogen recombination poison effect of H_2S was occurring simultaneously with the hydrogen barrier effect.

6.3 Paper III

Correlation between microstructure and hydrogen embrittlement susceptibility of flexible pipe steel armor wires measured by slow strain rate testing of notched samples

In Paper III, the correlation between carbon steel armor wire microstructure and hydrogen embrittlement was investigated by tensile slow strain rate tests of notched samples in air and 3.5 % NaCl solution while polarised to -1.4 V vs. Ag/AgCl, sat. KCl. All the six tensile armour wires were included in this study. In addition to notched samples, fatigue pre-cracked samples were tested for materials C and D. Finite element simulations were conducted in ABAQUS standard code using the stress and strain measured for smooth samples in Paper IV as input to predict the mechanical behaviour of the notched samples. Potentiodynamic polarisation curves were measured in 3.5 % NaCl to examine any differences between the cathodic current densities of the materials during cathodic polarisation to -1.4 V vs. Ag/AgCl, sat. KCl.

Samples with a 180 μm notch were tested under strain rate 10^{-6} s^{-1}. The samples were pre-charged with hydrogen in two steps and in-situ. The first pre-charging step was conducted in a separate container for three days. After the first pre-charging step, the samples were stored at -21 °C until the second pre-charging step, which was conducted in the load frame for six hours immediately before straining. The samples were imaged at rate 1-10 images per second during tests and the images were post-analysed in MATLAB to find the CMOD and CTOD. The sample surface facing the camera was scratched to create a pattern that could be analysed by DIC. The fracture surfaces were inspected by SEM. The susceptibility to hydrogen embrittlement was expressed by the notch tensile strength ratio, RNTS, i.e. NTS measured in hydrogen environment divided by the NTS measured in air, and the ratio of CTOD measured at maximum force in hydrogen environment divided by the CTOD measured at maximum force for tests in air.

The 3D plane strain FE model fitted the CTOD-force relationship of the experiments relatively well. The samples fractured before the predicted UTS but followed the trajectory obtained from the 3D models well until maximum force was reached.

Apart from Material B, all materials exhibited a certain degree of susceptibility to hydrogen embrittlement. Material B has the lowest carbon content and is the most ductile of the six tensile armour wires investigated. Although the mechanical properties of Material B was not affected by hydrogen in the tests, the fracture surfaces of the hydrogen-charged samples featured brittle cracks near the notch that were not observed for samples tested in air. Generally, the fracture surfaces of samples tested in air displayed dimples from microvoid coalescence, while the samples tested in hydrogen environment had crack formation near ferrite-cementite interfaces.

The RNTS increased with the plastic strain-to-failure and decreased with UTS. The CTOD measured at maximum force was lowered in the presence of hydrogen, and the strongest and least ductile materials were most affected. However, the trend was not as consistent as the trends observed for the RNTS. Material D had the highest sensitivity to hydrogen embrittlement. The CTOD at maximum force and NTS measured for hydrogen-charged samples of Material D were about a third of the magnitude measured for samples tested in air.

The difference between pre-cracked and notched samples tested in air was more significant for Material D, the lamellar material with high strength and carbon content, than it was for Material C, which has lower strength and carbon content, and globular cementite. For hydrogen-charged samples, no significant difference in mechanical behaviour was observed between notched and pre-cracked samples.

6.4 Paper IV

Hydrogen embrittlement susceptibility of steel armor wires for flexible pipes

Paper IV investigated the hydrogen embrittlement susceptibility of the six wire materials by SSRT. The hydrogen-charged samples were exposed to a 3.5 % NaCl solution while cathodically polarised to -1.1 and -1.4 V vs. Ag/AgCl, sat. KCl, at room temperature. The reference tests were conducted in air. The samples were in-situ charged and pre-charged both in a separate container (for three days) and in the load frame before straining (for six hours). The stain rate was 10^{-6} s^{-1}. The samples were pinned and the elastic part of the tensile tests were affected by the sample holders and pins used for that particular test. The plastic part was however unaffected. The fracture surface area, plastic elongation and fracture surfaces were compared for the two environments.

The fracture surfaces displayed cracks in the longitudinal direction. For samples tested in air, they were fewer and deeper, while hydrogen-charged samples formed more cracks which did not extend as far into the materials. For all materials except Material C, smaller smooth groves ($\leq$ 40 µm) were also observed along the same direction. These were referred to as micro-delamination cracks. For materials E and F, these were less numerous and shallower for hydrogen-charged samples compared to air-tested samples. For material B, the micro-delamination cracks appeared sharper, yet not deeper, for hydrogen-charged samples compared to the samples tested in air. Some small areas ($\leq$ 40 µm) on the fracture surfaces of hydrogen-charged samples of materials A and D displayed cleavage-like fractures.

Both the stress-strain curves and the fracture surfaces showed that hydrogen affects the mechanical properties and fracture mechanism in the wire materials. The UTS was not lowered by the presence of hydrogen, but the plastic elongation at fracture was. Based on the plastic elongation and fracture surface area, the HE susceptibility tended to increase with the carbon content, hardness and strength. It was also observed that the materials tended to be more brittle when charged to -1.4 V vs. Ag/AgCl than -1.1 V vs. Ag/AgCl.

7 Conclusions and further work

7.1 Conclusions

This work investigated the corrosion, hydrogen uptake and HE susceptibility of tensile armour wires for flexible pipes, and in particular the effect of microstructure. The experimental work was conducted for six types of steel armour wire which were characterized to distinguish their different microstructures.

The following conclusions were drawn after investigating the hydrogen uptake of the wires under cathodic polarisation, and in a corrosive CO_2 environment (0.2 or 1 bar) with low iron concentration ($<$ 10 ppmw) and either small amounts of H_2S ($\leq$ 0.7 mbar) or no H_2S:

- The effective hydrogen diffusion coefficients of the wires, measured during cathodic polarisation to -12 mA cm^{-2} in 0.1 M NaOH, were decreasing with increasing ferrite-cementite interfacial area. Hydrogen trapping on these interfaces is considered to be the reason.
- The reversible hydrogen uptakes measured for the wire materials during cathodic polarisation were about twice as high for the more deformed microstructures (materials B, D, E and F) than the less deformed microstructures (materials A and C).
- Reversible hydrogen uptakes below 0.6 ppmw were measured under pure CO_2 corrosion for the materials with globular cementite (materials A, B, C and E). For the lamellar materials (D and F), the hydrogen uptake could not be determined within the limited exposure period.
- Under exposure to CO_2 and H_2S, the hydrogen uptakes ranged from $\sim$ 0.2 to 1.4 ppmw. The highest hydrogen uptake was measured for Material D, but the hydrogen uptake measured for Material F was slightly uncertain and may have been slightly higher than 1.4 ppmw.
- Under exposure to CO_2, the materials that created a network of retained carbides got increasing corrosion rates and decreasing hydrogen uptakes with time. This is suggested to be related to the noble nature of cementite compared to ferrite, and the low diffusivity of hydrogen in cementite, which gives an increasing average distance between hydrogen adsorption site (retained cementite) and ferrite (uncorroded steel surface).
- The hydrogen uptakes were heavily influenced by the hydrogen recombination poison effect from H_2S when corroding in a solution with low iron content.

The following conclusions were drawn after investigating the effect of hydrogen on mechanical properties, measured for both smooth, notched (R = 180 μm) and fatigue pre-cracked samples:

- Generally, the effect of hydrogen on mechanical properties tended to increase in severity with the strength of the material, and decrease in severity with the ductility.
- The notch tensile strength and crack tip opening displacement at maximum force for hydrogen-charged samples were reduced by up to two thirds of the magnitude measured for samples not charged with hydrogen.
- The notch tensile strength ratio was decreasing with UTS and increasing with the plastic strain-to-failure. The crack-tip opening displacement measured at maximum force was also more affected by hydrogen for the strongest and least ductile materials. However, the trend was not as consistent as the trends observed for the notch tensile strength ratio.
- For the two lamellar carbon steels, Materials D and F, the material with higher carbon content, finer lamellas and higher extent of deformation, i.e. Material D, was more susceptible to hydrogen embrittlement.
- For notched and precracked samples exposed to hydrogen, crack formation occurred near ferrite-cementite interfaces, which confirms the importance of hydrogen interactions with the ferrite-cementite interfaces in the wire materials.
- No significant difference in mechanical behaviour for hydrogen-charged notched and pre-cracked samples was detected, even though the pre-cracked samples displayed inferior mechanical properties when tested in air compared to the mechanical properties of notched samples tested in air.

An interesting observation from this work is that the reversible hydrogen uptakes measured for the wire materials during cathodic polarisation were about twice as high for the more deformed microstructures (materials B, D, E and F) than the less deformed microstructures (materials A and C). This shows the importance of deformation as a source of hydrogen trapping sites in the wire materials. However, the HE susceptibility observed in tensile tests did not follow the same trend. The dislocation density is changed during tensile tests by dislocation movement, formation and annihilation. The trend of higher hydrogen uptake with higher deformation from production may therefore be more important for hydrogen damage mechanisms during the absence of applied stress (e.g. HIC) and less important for the HSC of the materials.

7.2 Further Work

The experiments conducted in this work have addressed a limited set of conditions relevant for the flexible pipes. The tests were only conducted in room temperature or at 25°C, and both hydrogen uptake, diffusion and corrosion processes are highly dependent on temperature. The iron concentration in the corrosive environment was kept low (< 10 ppmw), and the effect of varying iron concentration on corrosion mechanism and hydrogen uptake was not investigated. The work did not address all the possible failure mechanisms for flexible pipes. Fatigue testing, CF and HIC are all relevant for the steel wires and were not addressed. A study with complete information about the microstructural parameters would give further knowledge about the effect of grain size and heat treatments on trapping and HE susceptibility. The mechanical testing was conducted at the same strain rate, 10^{-6} s^{-1}, and since the results of tensile tests are sensitive to the strain rate, it would be interesting to investigate the effect of hydrogen at a slower strain rate, especially since the results of notched tests for Material B did not show any reduction of mechanical properties due to hydrogen.

For a broader investigation of EAC of flexible pipe steel armour wire, the following topics are of interest:

- Hydrogen uptake during corrosion in solutions with higher iron saturation and the effect of different corrosion products on hydrogen uptake both at open circuit potential and during cathodic polarisation.
- The effect of small amounts of hydrogen on embrittlement. An important question is whether the amount of hydrogen absorbed during CO_2 corrosion is enough to trigger hydrogen embrittlement, and whether the presence of pits alters the amount of hydrogen necessary to induce HE.
- The effect of residual stresses from production on the hydrogen uptake and diffusion.
- The sensitivity to H_2S related failure when the armour wires have been forming protective corrosion products in CO_2 environment for a long time. This topic is especially relevant for mature oil fields where the flexible pipes have been in use for years and the H_2S content in the well-fluid is increasing.
- The effects of corrosion and hydrogen uptake on the fatigue resistance of the armour wires.

Bibliography

[1] J. Muren, J. Eide, K. I. Engelbreth, H. Christensen, and C. Nilsen-Aas. Lifetime extension of flexible risers based on field experiences. *Offshore Technology Conference*, May 2016.

[2] E. Remita, F. Ropital, J. Kittel, B. Tribollet, E. Sutter, C. Taravel-Condat, and N. Desamais. Experimental and theoretical investigatoin of the uniform corrosion in the annulus of offshore flexible pipelines. NACE - International Corrosion Conference Series, March 2008. Paper no. 08538.

[3] Adam Rubin, Marie H. Haarh, Sten Overby, Torben S. Nielsen, and Jonas Gudme. Corrosion Rates of Carbon Steel in Confined Environments. 2012. Paper no. C2012-0001495.

[4] Aubry, J. C., Saas, J. N., Taravel-Condat, C., Benjelloun-Dabaghi, Z., and De Hemptinne, J. C. Moldi(tm): a Fluid Permeation Model to Calculate the Annulus Composition in Flexible Pipes. *Oil & Gas Science and Technology - Rev. IFP*, 57(2):177–192, 2002.

[5] Peter Barnes and Tom McLaughlin. Corrosion fatigue behaviour of high strength steel wire in various aqueous environments. NACE - International Corrosion Conference Series, 2015. Paper no, 5605.

[6] N. Désamais and C. Taravel-Condat. On the Beneficial Influence of a Very Low Supply of H_2S on the Hydrogen Embrittlement Resistance of Carbon Steel Wires in Flexible Pipe Annulus. Offshore Technology Conference, May 2009.

[7] A. Dugstad, L. Børvik, S. Palencsar, and P. A. Eikrem. Corrosion testing of steel armour wires in flexible pipes – a parametric study. NACE - International Corrosion Conference Series, March 2015. Paper no. 5829.

[8] 4 subsea. Un-bonded flexible risers – recent field experience and actions for increased robustness, 2013. Technical report. Doc.no. 0389-26583-U-0032.

[9] F. Dupoiron and C. Taravel-Condat. High strength metallic materials for flexible pipes. specific environments and corrosion behaviour. NACE - International Corrosion Conference Series, 2003. Paper no. 03113.

[10] Arne Dugstad, Simona Palencsar, Linda Børvik, and Tonje Berntsen. Corrosion of Steel Armor Wires in Flexible Pipes–Effect of Small Amount of H_2S. NACE - International Corrosion Conference Series, June 2020. Paper no. C2020-14876.

[11] Arne Dugstad, Simona Palencsar, Gaute Svenningsen, Jan Muren, Morten Eriksen, Benjamin Thoppil, John Melville, and Kushang Sanghavi. The Combined Effect of O_2 and CO_2 on Corrosion of Flexible Armour Wires. NACE - International Corrosion Conference Series, June 2020. Paper no. C2020-14790.

[12] J. Eide and J. Muren. Lifetime assessment of flexible pipes. *International Conference on Offshore Mechanics and Arctic Engineering*, 6B: Pipeline and Riser Technology, 2014.

[13] D. Pipa, S. Morikawa, G. Pires, C. Camerini, and J.M. Santos. Flexible riser monitoring using hybrid magnetic/optical strain gage techniques through rls adaptive filtering. *EURASIP Journal on Advances in Signal Processing*, 2010.

[14] Adam Rubin and Jonas Gudme. Qualification of Steel Wire for Flexible Pipes. NACE - International Corrosion Conference Series, 2006. Paper no. 06149.

[15] W. Sun and S. Nešić. Kinetics of corrosion layer formation: Part 1—iron carbonate layers in carbon dioxide corrosion. *Corrosion*, 64(4):334–346, 2008.

[16] Srdjan Nešić, Aage Stangeland, Rolf Nyborg, and Magnus Nordsveen. A mechanistic model for CO_2 corrosion with protective iron carbonate films. NACE - International Corrosion Conference Series, March 2001. Paper no. 01040.

[17] Srdjan Nešić. Key issues related to modelling of internal corrosion of oil and gas pipelines – A review. *Corrosion Science*, 49(12):4308–4338, 2007.

[18] Aria Kahyarian, Bruce Brown, and Srdjan Nesic. Mechanism of CO_2 Corrosion of Mild Steel: A New Narrative. NACE - International Corrosion Conference Series, April 2018. Paper no. C2018-11232.

[19] Richard Barker, Daniel Burkle, Thibaut Charpentier, Harvey Thompson, and Anne Neville. A review of iron carbonate ($FeCO_3$) formation in the oil and gas industry. *Corrosion Science*, 142:312–341, 2018.

[20] Janet Greenberg and Mason Tomson. Precipitation and dissolution kinetics and equilibria of aqueous ferrous carbonate vs temperature. *Applied Geochemistry*, 7(2):185–190, 1992.

[21] Wei Sun. *Kinetics of Iron Carbonate and Iron Sulfide Scale Formation in CO_2/H_2S Corrosion*. PhD thesis, Ohio University, 2006.

[22] F. Farelas, M. Galicia, B. Brown, S. Nesic, and H. Castaneda. Evolution of dissolution processes at the interface of carbon steel corroding in a CO_2 environment studied by EIS. *Corrosion Science*, 52(2):509–517, 2010.

[23] Arne Dugstad. Mechanism of Protective Film Formation During CO_2 Corrosion of Carbon Steel. NACE - International Corrosion Conference Series, March 1998. Paper no. 98031.

[24] Samara Cruz da Silva, Eduardo Alencar de Souza, Frederick Pessu, Yong Hua, Richard Barker, Anne Neville, and José Antônio da Cunha Ponciano Gomes. Cracking mechanism in API 5L X65 steel in a CO_2-saturated environment. *Engineering Failure Analysis*, 99:273–291, 2019.

[25] Chengshuang Zhou, Bei Fang, Jing Wang, Shiyin Hu, Baoguo Ye, Yanming He, Jinyang Zheng, and Lin Zhang. Effect of interaction between corrosion film and H_2S/CO_2 partial pressure ratio on the hydrogen permeation in X80 pipeline steel. *Corrosion Engineering, Science and Technology*, 55(5):392–399, 2020.

[26] M.B. Kermani and A. Morshed. Carbon Dioxide Corrosion in Oil and Gas Production - A Compendium. *Corrosion*, 59(8):659–683, 2003.

[27] F. Farelas, B. Brown, and S. Nesic. Iron Carbide and its Influence on the Formation of Protective Iron Carbonate in CO_2 Corrosion of Mild Steel. NACE - International Corrosion Conference Series, March 2013. Paper no. 2291.

[28] J.L. Crolet, N. Thevenot, and S. Nesic. Role of Conductive Corrosion Products in the Protectiveness of Corrosion Layers. *Corrosion*, 54(3), 1998.

[29] Masakatsu Ueda and Akio Ikeda. Effect of Microstructure and Cr Content in Steel on CO_2 Corrosion. NACE - International Corrosion Conference Series, March 1996. Paper no. 96013.

[30] J.L. Mora-Mendoza and S. Turgoose. Fe_3C influence on the corrosion rate of mild steel in aqueous CO_2 systems under turbulent flow conditions. *Corrosion Science*, 44(6):1223–1246, 2002.

[31] Tatiane Campos, Marion Seiersten, Simona Palencsár, Arne Dugstad, and José A. Ponciano Gomes. Corrosion of High-Strength Carbon Steels in Siderite Supersaturated Water at Near Neutral pH. *Corrosion*, 77(6):632–645, 2021.

[32] D. Burkle, R. De Motte, W. Taleb, A. Kleppe, T. Comyn, S.M. Vargas, A. Neville, and R. Barker. In situ SR-XRD study of $FeCO_3$ precipitation kinetics onto carbon steel in CO_2 -containing environments: The influence of brine pH. *Electrochimica Acta*, 255:127–144, 2017.

[33] Arne Dugstad. Fundamental Aspects of CO_2 Metal Loss Corrosion, Part I: Mechanism. NACE - International Corrosion Conference Series, 2015. Paper no. 5826.

[34] F. Yu, K.W. Gao, Y.J. Su, J.X. Li, L.J. Qiao, W.Y. Chu, and M.X. Lu. The fracture toughness of CO_2 corrosion scale in pipeline steel. *Materials Letters*, 59(14-15):1709–1713, 2005.

[35] Saba Navabzadeh Esmaeely, Yoon-Seok Choi, David Young, and Srdjan Nešić. Effect of Calcium on the Formation and Protectiveness of Iron Carbonate Layer in CO_2 Corrosion. *Corrosion*, 69(9):912–920, 2013.

[36] Lisiane Morfeo Tavares, Eleani Maria da Costa, Jairo José de Oliveira Andrade, Roberto Hubler, and Bruno Huet. Effect of calcium carbonate on low carbon steel corrosion behavior in saline CO_2 high pressure environments. *Applied Surface Science*, 359:143–152, 2015.

[37] Frederick Pessu, Richard Barker, and Anne Neville. The Influence of pH on Localized Corrosion Behavior of X65 Carbon steel in CO_2-Saturated Brines. *Corrosion*, 71(12):1452–1466, 2015.

[38] A. Dugstad, S. Palencsár, T. Berntsen, and L. Børvik. Corrosion of Steel Armour Wires in Flexible Pipes - History Effects. SPE International Oilfield Corrosion Conference and Exhibition, June 2018.

[39] Nor Roslina Rosli, Yoon-Seok Choi, and David Young. Impact of Oxygen Ingress in CO_2 Corrosion of Mild Steel. NACE - International Corrosion Conference Series, March 2014. Paper no. 4299.

[40] S. Al-Hassan, B. Mishra, D.L. Olson, and M.M. Salama. Effect of Microstructure on Corrosion of Steels in Aqueous Solutions Containing Carbon Dioxide. *Corrosion*, 54(6), 1998.

[41] P. E. Yudin, T. M. Pugacheva, L. A. Kondratyeva, and M. V. Bogatov. Investigation of the influence of the steel 20 microstructure on the carbon dioxide corrosion rate. *Metal Science and Heat Treatment*, 62:415–419, 2020.

[42] D.A López, W.H Schreiner, S.R de Sánchez, and S.N Simison. The influence of carbon steel microstructure on corrosion layers: An XPS and SEM characterization. *Applied Surface Science*, 207(1):69–85, 2003.

[43] Nathalie Ochoa, Carlos Vega, Nadine Pébère, Jacques Lacaze, and Joaquín L. Brito. CO_2 corrosion resistance of carbon steel in relation with microstructure changes. *Materials Chemistry and Physics*, 156:198–205, 2015.

[44] G.A. Zhang, Y. Zeng, X.P. Guo, F. Jiang, D.Y. Shi, and Z.Y. Chen. Electrochemical corrosion behavior of carbon steel under dynamic high pressure H_2S/CO_2 environment. *Corrosion Science*, 65:37–47, 2012.

[45] L.L Shreir and R.A Cottis. Corrosion in liquids, corrosion evaluation. In Bob Cottis, Mike Graham, Rob Lindsay, Stuart Lyon, Tony Richardson, David Scantlebury, and Howard Scott, editors, *Shreir's corrosion*, volume 2, pages 725–1692. Elsevier, Amsterdam, 4th ed. edition, 2010.

[46] Xiangli Wen, Pengpeng Bai, Bingwei Luo, Shuqi Zheng, and Changfeng Chen. Review of recent progress in the study of corrosion products of steels in a hydrogen sulphide environment. *Corrosion Science*, 139:124–140, 2018.

[47] Yougui Zheng, Bruce Brown, and Srdjan Nešić. Electrochemical Study and Modeling of H_2S Corrosion of Mild Steel. *Corrosion*, 70(4):351–365, 2013.

[48] X. L. Cheng, H. Y. Ma, J. P. Zhang, X. Chen, S. H. Chen, and H. Q. Yang. Corrosion of Iron in Acid Solutions with Hydrogen Sulfide. *Corrosion*, 54(5):369–376, 1998.

[49] Pengpeng Bai, Shuqi Zheng, Changfeng Chen, and Hui Zhao. Investigation of the iron–sulfide phase transformation in nanoscale. *Crystal Growth and Design*, 14(9):4295–4302, 2014.

[50] Wei Sun and Srdjan Nesic. A Mechanistic Model of H_2S Corrosion of Mild Steel. NACE - International Corrosion Conference Series, March 2007. Paper no. 07655.

[51] David Rickard and George W. Luther. Chemistry of iron sulfides. *Chemical Reviews*, 107(2):514–562, 2007.

[52] David Rickard, A. Griffith, A. Oldroyd, I.B. Butler, E. Lopez-Capel, D.A.C. Manning, and D.C. Apperley. The composition of nanoparticulate mackinawite, tetragonal iron(II) monosulfide. *Chemical Geology*, 235(3):286–298, 2006.

[53] Jon Kvarekvål and Jeremy Moloney. 6 - sour corrosion. In A.M. El-Sherik, editor, *Trends in Oil and Gas Corrosion Research and Technologies*, Woodhead Publishing Series in Energy, pages 113–147. Woodhead Publishing, Boston, 2017.

[54] Meng Liu, Jianqiu Wang, Wei Ke, and En-Hou Han. Corrosion behavior of X52 anti-H_2S pipeline steel exposed to high H_2S concentration solutions at 90 °C. *Journal of Materials Science and Technology*, 30(5):504–510, 2014.

[55] Elien Wallaert, Tom Depover, Iris De Graeve, and Kim Verbeken. FeS Corrosion Products Formation and Hydrogen Uptake in a Sour Environment for Quenched and Tempered Steel. *Metals*, 8(1), 2018.

[56] Yougui Zheng, Jing Ning, Bruce Brown, David Young, and Srdjan Nesic. Mechanistic Study of the Effect of Iron Sulfide Layers on Hydrogen Sulfide Corrosion of Carbon Steel. NACE - International Corrosion Conference Series, March 2015. Paper no. 5933.

[57] Stephen N. Smith and Jorge L. Pacheco. Prediction of Corrosion in Slightly Sour Environments. NACE - International Corrosion Conference Series, April 2002. Paper no. 02241.

[58] Jon Kvarekval, Rolf Nyborg, and Marion Seiersten. Corrosion Product Films on Carbon Steel in Semi-Sour CO_2/H_2S Environments. NACE - International Corrosion Conference Series, April 2002. Paper no. 02296.

[59] Frederick Pessu, Richard Barker, and Anne Neville. Pitting and Uniform Corrosion of X65 Carbon Steel in Sour Corrosion Environments: The Influence of CO_2, H_2S, and Temperature. *Corrosion*, 73(9):1168–1183, 2017.

[60] Saba Navabzadeh Esmaeely, Wei Zhang, Bruce Brown, Marc Singer, and Srdjan Nesic. Localized Corrosion of Mild Steel in Marginally Sour Environments. NACE - International Corrosion Conference Series, April 2018. Paper no. 10548.

[61] Sijm Last, Steve Groves, Jean Rigaud, Carol Taravel-Condat, Jakob Wedel-Heinen, Richard Clements, and Stefan Buchner. Comparison of models to predict the annulus conditions of flexible pipe. *Offshore Technology Conference*, 2002.

[62] Z. Benjelloun-Dabaghi1, J.-C. de Hemptinne, J. Jarrin, J.-M. Leroy1, J.-C. Aubry, J.N. Saas, and C. Taravel-Condat. A fluid permeation model to calculate the annulus composition in flexible pipes. *Oil and Gas Science and Technology*, 75:177–192, 2002.

[63] NACE/ASTM G193-20a. Standard Terminology and Acronyms Relating to Corrosion, 2020.

[64] Stan Lynch. Understanding mechanisms and kinetics of environmentally assisted cracking. *Berg- und Hüttenmännische Monatshefte*, 161(1):3–18, 2016.

[65] Sridhar Ramamurthy and Andrej Atrens. Stress corrosion cracking of high-strength steels. *Corrosion Reviews*, 31(1):1–31, 2013.

[66] ANSI/NACE. Standard test method: Laboratory testing of metals for resistance to sulfide stress cracking and stress corrosion cracking in h_2s environments, 1997.

[67] Khlefa A. Esaklul. 13 - Hydrogen damage. In A.M. El-Sherik, editor, *Trends in Oil and Gas Corrosion Research and Technologies*, Woodhead Publishing Series in Energy, pages 315–340. Woodhead Publishing, Boston, 2017.

[68] C.A. Zapffe and C.E. Sims. Hydrogen embrittlement, internal stress and defects in steel. *Trans. AIME*, 145:225–261, 1941.

[69] D.G. Westlake. A generalized model for hydrogen embrittlement. *Trans. ASM.*, 62:1000 – 1006, 1969.

[70] Piotr Kedzierzawski. Hydrogen trapping in iron and iron alloys. In Richard A. Oriani, John P. Hirth, and Michael Smialowski, editors, *Hydrogen Degradation of Ferrous Alloys*, pages 271–288. William Andrew Publishing/Noyes, 4th ed. edition, 1985.

[71] T.P. Radhakrishnan and L.L. Shreir. Permeation of hydrogen through steel by electrochemical transfer—i. influence of catalytic poisons. *Electrochimica Acta*, 11(8):1007–1021, 1966.

[72] C.D. Beachem. A new model for hydrogen-assisted cracking (hydrogen "embrittlement"). *Metallurgical and Materials Transactions B*, 3:441–455, 1972.

[73] H.K. Birnbaum and P. Sofronis. Hydrogen-enhanced localized plasticity—a mechanism for hydrogen-related fracture. *Materials Science and Engineering: A*, 176(1):191–202, 1994.

[74] A.R. Troiano. The role of hydrogen and other interstitials in the mechanical behavior of metals (1959 edward de mille campbell memorial lecture). *Transactions of American Society for Metals*, 52:54–80, 1960.

[75] S.P. Lynch. Environmentally assisted cracking: Overview of evidence for an adsorption-induced localised-slip process. *Acta Metallurgica*, 36(10):2639–2661, 1988.

[76] M. Nagumo. Hydrogen related failure of steels – a new aspect. *Materials Science and Technology*, 20(8):940–950, 2004.

[77] Reiner Kirchheim. Revisiting hydrogen embrittlement models and hydrogen-induced homogeneous nucleation of dislocations. *Scripta Materialia*, 62(2):67–70, 2010.

[78] S. Lynch. Hydrogen embrittlement phenomena and mechanisms. *Corrosion reviews*, 30:105–123, 2012.

[79] Daniel P. Abraham and Carl J. Altstetter. Hydrogen-enhanced localization of plasticity in an austenitic stainless steel. *Metallurgical and Materials Transactions A*, 26A:2859–2871, 1995.

[80] T. Depover and K. Verbeken. The detrimental effect of hydrogen at dislocations on the hydrogen embrittlement susceptibility of Fe-C-X alloys: An experimental proof of the HELP mechanism. *International Journal of Hydrogen Energy*, 43(5):3050–3061, 2018.

[81] S.P. Lynch. Progress Towards Understanding Mechanisms Of Hydrogen Embrittlement And Stress Corrosion Cracking. NACE - International Corrosion Conference Series, March 2007. Paper no. 07493.

[82] R. G. Hoagland and H. L. Heinisch. An atomic simulation of the influence of hydrogen on the fracture behavior of nickel. *Journal of Materials Research*, 7:2080–2088, 1992.

[83] D.E. Jiang and Emily A. Carter. First principles assessment of ideal fracture energies of materials with mobile impurities: implications for hydrogen embrittlement of metals. *Acta Materialia*, 52(16):4801–4807, 2004.

[84] Murray S. Daw and Michael I. Baskes. Application of the embedded atom method to hydrogen embrittlement. In R. M. Latanision and R. H. Jones, editors, *Chemistry and Physics of Fracture*, pages 196–218. Springer Netherlands, Dordrecht, 1987.

[85] James A. Clum. The role of hydrogen in dislocation generation in iron alloys. *Scripta Metallurgica*, 9(1):51–58, 1975.

[86] H.K. Birnbaum, C. Buckley, F. Zeides, E. Sirois, P. Rozenak, S. Spooner, and J.S. Lin. Hydrogen in aluminum. *Journal of Alloys and Compounds*, 253-254:260–264, 1997.

[87] Yuk Fukai and Nobuyuki Ōkuma. Formation of superabundant vacancies in pd hydride under high hydrogen pressures. *Phys. Rev. Lett.*, 73:1640–1643, Sep 1994.

[88] John P. Hirth. Effects of hydrogen on the properties of iron and steel. *Metallurgical Transactions A*, 11:861–890, 1980.

[89] Robert Baboian. Hydrogen damage. In *Corrosion Tests and Standards: Application and Interpretation: (MNL 20)*, chapter 27, pages 322–340. ASTM International, 2005.

[90] W. Beck, J. O'M. Bockris, J. McBreen, and L. Nanis. Hydrogen permeation in metals as a function of stress, temperature and dissolved hydrogen concentration. *Proceedings of the Royal Society of London. Series A, Mathematical and Physical Sciences*, 290:220–235, 1966.

[91] D. Hardie and Su'e Liu. The effect of stress concentration on hydrogen embrittlement of a low alloy steel. *Corrosion Science*, 38(5):721–733, 1996.

[92] J. Toribio, V. Kharin, D. Vergara, and M. Lorenzo. Optimization of the simulation of stress-assisted hydrogen diffusion for studies of hydrogen embrittlement of notched bars. *Materials Science*, 46:819–833, 2011.

[93] J. Toribio. Role of hydrostatic stress in hydrogen diffusion in pearlitic steel. *Journal of Materials Science*, 28:2289–2298, 1993.

[94] International Organization for Standardization. ISO 17081 Method of measurement of hydrogen permeation and determination of hydrogen uptake and transport in metals by an electrochemical technique, June 2014.

[95] K. O. Findley, M. K. O'Brien, and H. Nako. Critical assessment 17: Mechanisms of hydrogen induced cracking in pipeline steels. *Materials Science and Technology*, 31(14):1673–1680, 2015.

[96] Kenichi Takai and Ryu Watanuki. Hydrogen in trapping states innocuous to environmental degradation of high-strength steels. *ISIJ International*, 43(4):520–526, 2003.

[97] A. Turnbull. Perspectives on hydrogen uptake, diffusion and trapping. *International Journal of Hydrogen Energy*, 40(47):16961 – 16970, 2015. Special issue on 1st International Conference on Hydrogen Storage, Embrittlement and Applications (Hy-SEA 2014), 26-30 October 2014, Rio de Janeiro, Brazil.

[98] J. L. Lee and Jai Young Lee. Hydrogen trapping in aisi 4340 steel. *Metal Science*, 17(9):426–432, 1983.

[99] I. Maroef, D. L. Olson, M. Eberhart, and G. R. Edwards. Hydrogen trapping in ferritic steel weld metal. *International Materials Reviews*, 47(4):191–223, 2002.

[100] M. F. Stevens and I. M. Bernstein. Microstructural trapping effects on hydrogen induced cracking of a microalloyed steel. *Metallurgical Transactions A*, 20(5):909–919, May 1989.

[101] R. Valentini, A. Solina, S. Matera, and P. De Gregorio. Influence of titanium and carbon contents on the hydrogen trapping of microalloyed steels. *Metallurgical and Materials Transactions A*, 27(12):3773–3780, Dec 1996.

[102] T. Depover, D. Pérez Escobar, E. Wallaert, Z. Zermout, and K. Verbeken. Effect of hydrogen charging on the mechanical properties of advanced high strength steels. *International Journal of Hydrogen Energy*, 39(9):4647–4656, 2014.

[103] G.M. Pressouyre and I.M. Bernstein. A quantitative analysis of hydrogen trapping. *Metallurgical Transactions A*, 9:1571–1580, 1978.

[104] Xiaomin Yuan. Precipitates and hydrogen permeation behavior in ultra-low carbon steel. *Materials Science and Engineering: A*, 452-453:116 – 120, 2007.

[105] M. Nagumo, K. Ohta, and H. Saitoh. Deformation induced defects in iron revealed by thermal desorption spectroscopy of tritium. *Scripta Materialia*, 40(3):313–319, 1999.

[106] A.H. Bott, D.S. Dos Santos, and P.E.V. De Miranda. Influence of cementite morphology on the hydrogen permeation parameters of low-carbon steel. *Journal of Materials Science Letters*, 12:390–393, 1993.

[107] C.P. Ju and J.M. Rigsbee. Interfacial coherency and hydrogen damage in plain carbon steel. *Materials Science and Engineering: A*, 102(2):281–288, 1988.

[108] Gye Won Hong and Jai-Young Lee. The interaction of hydrogen and the cementite-ferrite interface in carbon steel. *Journal of Materials Science*, 18:271–277, 1983.

[109] Maoqiu Wang, Eiji Akiyama, and Kaneaki Tsuzaki. Effect of hydrogen on the fracture behavior of high strength steel during slow strain rate test. *Corrosion Science*, 49(11):4081–4097, 2007.

[110] Kazuto Kawakami and Tooru Matsumiya. *Ab-initio* Investigation of Hydrogen Trap State by Cementite in bcc-Fe. *ISIJ International*, 53(4):709–713, 2013.

[111] K. Kiuchi and R.B. McLellan. The solubility and diffusivity of hydrogen in well-annealed and deformed iron. *Acta Metallurgica*, 31(7):961 – 984, 1983.

[112] ASTM G148-97. Standard practice for evaluation of hydrogen uptake, permeation, and transport in metals by an electrochemical technique, 2018.

[113] W. Dietzel, M. Pfuff, and G.G. Juilfs. Hydrogen permeation in plastically deformed steel membranes. *Materials Science*, 42:78–84, 2006.

[114] Tom Depover, Aurélie Laureys, Diana Pérez Escobar, Emilie Van den Eeckhout, Elien Wallaert, and Kim Verbeken. Understanding the interaction between a steel microstructure and hydrogen. *Materials*, 11(5), 2018.

[115] M. Hashimoto and R. M. Latanision. Experimental study of hydrogen transport during plastic deformation in iron. *Metallurgical Transactions A*, 19:2789–2798, 1988.

[116] Sung Jin Kim, Dae Won Yun, Dong Woo Suh, and Kyoo Young Kim. Electrochemical hydrogen permeation measurement through trip steel under loading condition of phase transition. *Electrochemistry Communications*, 24:112–115, 2012.

[117] A.-M. Brass and J. Chêne. Influence of tensile straining on the permeation of hydrogen in low alloy Cr–Mo steels. *Corrosion Science*, 48(2):481–497, 2006.

[118] C. Zheng and C. Wang. Effect of stress on hydrogen permeation for x70 carbon steel in seawater. *Materials Performance*, 56:54–58, 2017.

[119] M. Cabrini, S. Maffi, and G. Razzini. Evaluation of the hydrogen embrittlement behaviour by means of the permeation current measure in slow strain rate conditions of a micro-alloyed steel. In *Electrochemical Methods in Corrosion Research VI*, volume 289 of *Materials Science Forum*, pages 1245–1256. Trans Tech Publications Ltd, 8 1998.

[120] F. Bolzoni, M. Cabrini, and C. Spinelli. Hydrogen diffusion and hydrogen embrittlement behaviour of two high strength pipeline steels. Eurocorr, 2001.

[121] A. Turnbull and R.B. Hutchings. Analysis of hydrogen atom transport in a two-phase alloy. *Materials Science and Engineering: A*, 177(1):161 – 171, 1994.

[122] Andrej Turk, Shengda Pu, David Bombač, Pedro E.J. Rivera-Díaz del Castillo, and Enrique I. Galindo-Nava. Quantification of hydrogen trapping in multiphase steels: Part II – Effect of austenite morphology. *Acta Materialia*, 197:253–268, 2020.

[123] L. Tau and S.L.I. Chan. Effects of ferrite/pearlite alignment on the hydrogen permeation in a AISI 4130 steel. *Materials Letters*, 29(1):143–147, 1996.

[124] C. Forot, E Legrand, E. Roguet, J. Creus, J. Kittel, and Xavier Feaugas. Impact of cementite tortuosity on hydrogen diffusion in pearlitic steels. In *Eurocorr 2015*, September 2015.

[125] G. M. Pressouyre. Hydrogen traps, repellers, and obstacles in steel; consequences on hydrogen diffusion, solubility, and embrittlement. *Metallurgical Transactions A*, 14:2189–2193, 1983.

[126] W.C. Luu and J.K. Wu. The influence of microstructure on hydrogen transport in carbon steels. *Corrosion Science*, 38(2):239–245, 1996. cited By 79.

[127] S. L. I. Chan and J. A. Charles. Effect of carbon content on hydrogen occlusivity and embrittlement of ferrite–pearlite steels. *Materials Science and Technology*, 2(9):956–962, 1986.

[128] Nayef M. Alanazi and Abdullah A. Al-Enezi. The Effect of the Partial Pressure of H_2S and CO_2 on the Permeation of Hydrogen in Carbon Steel by Using Pressure Buildup Techniques. *Corrosion*, 75(10):1207–1215, 2019.

[129] Wenhui Hao, Lei Zhang, Jianwei Yang, Han Li, Jinhui Ding, and Minxu Lu. Effect of H_2S/CO_2 Corrosion Scale On Hydrogen Permeation. NACE - International Corrosion Conference Series, 2011. Paper no. 11293.

[130] F. Huang, P. Cheng, X.Y. Zhao, J. Liu, Q. Hu, and Y. Frank Cheng. Effect of sulfide films formed on X65 steel surface on hydrogen permeation in H_2S environments. *International Journal of Hydrogen Energy*, 42(7):4561–4570, 2017.

[131] Jianwei Yang, Lei Zhang, Lining Xu, and Minxu Lu. Influence of H_2S and CO_2 corrosion scales on hydrogen permeation in X65 steel. NACE - International Corrosion Conference Series, 2008. Paper No. 08412.

[132] HORIBA Ltd. Instrument Introduction. Accessed January 2022. `https://www.horiba.com/en_en/technology/surface-science-techniques0/glow-discharge-optical-emission-spectroscopy-gd-oes/instrument-introduction/`.

[133] Struers. Technical data - Silicon Carbide Grinding Foils and Papers. Accessed January 2022. `https://publications.struers.com/brochures/english/technical-data-sheet/consumables/sic-foil-paper/?_ga=2.170408292.597204764.1636987844-1482010801.1636987844`.

[134] NACE Standard TM0198 Slow Strain Rate Test Method for Screening Corrosion-Resistant Alloys for Stress Corrosion Cracking in Sour Oilfield Service, 2016.

[135] D. Johnson and G. Krauss. Correlation of microstructural parameters and hydrogen permeation in carbon steel. *Metallurgical Transactions A*, 18 A:717–721, 1987.

[136] M. A. V. Devanathan and Z. Stachurski. The adsorption and diffusion of electrolytic hydrogen in palladium. *Proceedings of the Royal Society of London. Series A, Mathematical and Physical Sciences*, 270(1340):90–102, 1962.

[137] Hans Husby. *Effect of nickel in solid solution on the hydrogen embrittlement resistance of low alloy steels*. PhD thesis, Norwegian University of Science and Technology, 2018. ISBN: 978-82-326-3253-4.

[138] P. Bruzzoni and R. Garavaglia. Anodic iron oxide films and their effect on the hydrogen permeation through steel. *Corrosion Science*, 33(11):1797 – 1807, 1992.

[139] T. Zakroczymski and Z. Szklarska-Smialowska. Activation of the iron surface to hydrogen absorption resulting from a long cathodic treatment in NaOH solution. *Journal of The Electrochemical Society*, 132(11):2548–2552, nov 1985.

[140] Pablo Bruzzoni. *Efectos de superficie en la difusión de hidrógeno en hierro y aleaciones ferrosas*. PhD thesis, Universidad de Buenos Aires, 2003.

[141] Hans Husby, Mariano Iannuzzi, Roy Johnsen, Mariano Kappes, and Afrooz Barnoush. Effect of nickel on hydrogen permeation in ferritic/pearlitic low alloy steels. *International Journal of Hydrogen Energy*, 43(7):3845 – 3861, 2018.

[142] T. Zakroczymski. Permeability of iron to hydrogen cathodically generated in 0.1 M NaOH. *Scripta Metallurgica*, 19(4):521 – 524, 1985.

[143] ASTM G129-00. Standard practice for slow strain rate testing to evaluate the susceptibility of metallic materials to environmentally assisted cracking, 2013.

Appended papers

Paper I

E.S. Skilbred, M. Kappes, M.Iannuzzi, R. Johnsen

Hydrogen uptake and diffusivity in steel armor wires with different chemical composition, carbide distribution, grain size, and degree of deformation

Materials and corrosion (2021), 1-20. DOI: 10.1002/maco.202112615

Received: 20 June 2021 | Accepted: 25 October 2021

DOI: 10.1002/maco.202112615

ARTICLE

Materials and Corrosion

Hydrogen uptake and diffusivity in steel armor wires with different chemical composition, carbide distribution, grain size, and degree of deformation

Ellen S. Skilbred[1] | **Mariano Kappes**[2] | **Mariano Iannuzzi**[1,3] | **Roy Johnsen**[1]

[1]Department of Mechanical and Industrial Engineering, Norwegian University of Science and Technology, Trondheim, Norway

[2]Instituto Sabato, San Martín, Buenos Aires, Argentina

[3]Curtin Corrosion Centre, Curtin University, Perth, Western Australia, Australia

Correspondence
Ellen S. Skilbred, Department of Mechanical and Industrial Engineering, Norwegian University of Science and Technology, 7034 Trondheim, Norway.
Email: ellen.s.skilbred@ntnu.no

Funding information
The Research Council of Norway, Grant/Award Number: 280760

Abstract

In this study, six flexible pipe steel armor wires used in oil and gas transportation are characterized, and their hydrogen diffusion coefficients and hydrogen uptakes are measured using an electrochemical hydrogen permeation technique. The wires have ferritic–pearlitic microstructures with round, lamellar, or partially lamellar carbides and the shape and orientation of the grains indicate that the microstructures were plastically deformed to different degrees. It was assumed that hydrogen was transported through the ferrite, so the presence of cementite in the steel armor wires leads to longer hydrogen diffusion paths through the ferrite, which was quantified with a tortuosity factor. After compensating for tortuosity, the normalized steady-state flux shows a tendency to increase as the grain size decreases. The effective diffusion coefficients increase with a decrease of the ferrite–cementite interface area, suggesting trapping on the ferrite–cementite interfaces. The uptake of diffusible hydrogen was lowest for the least plastically deformed materials and about twice as high for the more plastically deformed materials.

KEYWORDS
carbide distribution, deformation, diffusivity, hydrogen, steel armor wires

1 | INTRODUCTION

Flexible pipes are frequently used for oil and gas transportation. Each pipe consists of several layers with specific purposes that combined give the desired mechanical and chemical resistance required for the designed operating conditions. Many designs are possible, but usually, the pipes comprise five main unbonded layers: a carcass made of a corrosion-resistant alloy closest to the bore, a polymer sheath, a pressure armor layer made of steel, a tensile armor layer made of high strength steel wires, and an outer polymer sheath.[1,2] The annulus around the tensile armor wires is dry under normal operating conditions but can be flooded with condensed water containing corrosive species like CO_2, H_2S, or both, which permeate from the bore, and seawater when there are damages in the outer polymer sheath. The resulting exposure to corrosive media can lead to corrosion and hydrogen embrittlement (HE) of the tensile wires.[1–4] In this regard, both corrosion and cathodic protection (when the outer shielding is damaged) may introduce atomic hydrogen to the wires.

Several incidents of brittle fractures and severe corrosion attacks of flexible pipe steel armor wires have been reported[5–7] and the failure mechanism can be complex. Understanding the relationship between hydrogen uptake and microstructure in the armor wires is a crucial step towards understanding the complex failure mechanisms of flexible pipes and improving flexible pipe design.

HE is caused by the presence of hydrogen within an alloy or metal.[8] In carbon and low alloy steels, the presence of atomic hydrogen can induce premature failures by interactions with dislocation formation and movement, decreasing the cohesion between atoms in the lattice, and interaction with local stress and strain fields.[9] Some microstructural sites have a higher affinity to hydrogen than the interstitial lattice sites and serve as hydrogen traps. Hydrogen traps are often divided into reversible and irreversible, according to the hydrogen desorption probability at room temperature.

Given the very low probability of hydrogen desorption from irreversible traps, they can be saturated even when the hydrogen concentration in the material is low, whereas reversible traps can reach dynamic equilibrium with the hydrogen in the lattice. Grain and phase boundaries, vacancies, inclusions, and dislocations are all examples of typical trapping sites in steels.[10] Findley et al.[11] summarized the binding energy of several types of traps from 18 references and reported that the binding energy of dislocations was 18–59.9 kJ mol^{-1}, grain boundaries 8.8–58.9 kJ mol^{-1}, voids 29.1 kJ mol^{-1}, and ferrite–cementite interface 8.4–15.7 kJ mol^{-1}. These are all considered reversible traps. The hydrogen in lattice and reversible traps—also referred to as diffusible hydrogen—has a more severe impact on mechanical properties than the irreversibly trapped hydrogen since the diffusible hydrogen can accumulate in regions with high stress and facilitate crack initiation and propagation.[9,12]

There is a substantial body of research on the effect of different parameters on the HE susceptibility of steels where the microstructures were carefully controlled to investigate the effect of changing one parameter at a time.[13–21] However, there is limited work on the interplay between armor wire steel microstructure and hydrogen to date. In this paper, the HE susceptibility of materials with complex microstructures is investigated, and the difference in hydrogen diffusivity, permeation flux, and uptake is discussed based on several differences in microstructural features. Six types of flexible pipe armor steel wire were tested using electrochemical hydrogen permeation experiments. The work focuses on estimating the diffusible hydrogen content since this is the most detrimental in cases where there is a constant supply of hydrogen, like during a corrosion process or cathodic protection of a flooded flexible pipe annulus. A detailed metallographic study was conducted to compare the microstructures of the wires and to distinguish between the effect of hydrogen trapping and tortuous hydrogen diffusion paths on the effective diffusion coefficients. The wires tested were qualified according to the API 17J Specification for Unbonded Flexible Pipe[22] for different operating conditions, as discussed below. The outcome of this investigation will support future considerations regarding the replacement and lifetime extension of flexible pipes.

2 | EXPERIMENTAL

2.1 | Materials

Six types of flexible pipe wires qualified for different operating conditions were provided and are identified by letters A–F. The wire materials complied with API 17J and were delivered in their service thermo-mechanical condition. Samples were taken from coils, and some pieces were straightened using a roller straightener to fit the required dimensions of the electrochemical permeation cell. The thickness of the wires was 3 mm, and the widths ranged from 9 to 12 mm. The chemical compositions of the wires are given in Table 1. Scanning electron microscopy (SEM) images of the center of the cross-sections of the six materials are given in Figure 1. The surfaces in the images were prepared as described in Section 2.2. Images at a higher magnification can be consulted in Figure 2 for Materials D and E. All the wires had features associated with rolled microstructures, with grains being narrower through-thickness than in the width and length directions. The exact thermo-mechanical fabrication route of these materials was not available, but the size and shape of ferrite provided insight on whether the wires were subjected to long heat treatments after the rolling process. The wires' extent of plastic deformation, the estimated grain size, and the cementite morphology are described in Table 2 with the hardness, yield strength, ultimate tensile strength, and plastic strain-to-failure (Ep). The Ep was calculated according to NACE Standard TM0198-2016.[23] The materials have complex microstructures with many unclear grain boundaries and the grain size is therefore described by the largest well-defined grains observed instead of average grain size. The ferrite and cementite grains were of different sizes and are therefore evaluated separately.

TABLE 1 Cementite fractions (f) and chemical compositions of the wire materials

Material	f	C (wt%)	Si (wt%)	S (wt%)	P (wt%)	Mn (wt%)	Ni (wt%)	Cr (wt%)	Al (wt%)
A	0.077	0.501	0.247	0.002	0.003	0.604	0.001	0.011	0.031
B	0.043	0.282	0.223	0.010	0.006	0.733	0.010	0.003	0.035
C	0.054	0.353	0.194	0.007	0.009	0.678	0.013	0.003	0.042
D	0.127	0.830	0.331	0.005	0.005	0.683	0.005	0.002	0.041
E	0.095	0.618	0.225	0.002	0.007	0.729	0.009	0.032	0.037
F	0.100	0.651	0.240	0.009	0.002	0.630	0.060	0.025	0.003

Material	V (wt%)	Pb (wt%)	N (wt%)	Ti (wt%)	Sn (wt%)	Cu (wt%)	Co (wt%)	Mo (wt%)	B (wt%)
A	0.036	0.050	0.009	$<10^{-4}$	N.D.	N.D.	N.D.	0.001	$<10^{-4}$
B	0.001	0.065	0.020	0.002	N.D.	$<10^{-4}$	$<10^{-4}$	0.001	$<10^{-4}$
C	0.002	0.065	0.219	0.002	$<10^{-3}$	0.001	N.D.	0.001	$<10^{-4}$
D	0.050	0.065	0.099	0.004	0.001	$<10^{-4}$	N.D.	0.002	$<10^{-3}$
E	0.001	0.050	0.014	$<10^{-4}$	N.D.	N.D.	N.D.	$<10^{-3}$	$<10^{-4}$
F	0.001	0.040	0.009	N.D.	N.D.	$<10^{-3}$	0.001	$<10^{-4}$	$<10^{-4}$

Note: Elements that were not detected for a particular material are labeled with N.D.

Abbreviations: Ep, plastic strain-to-failure; UTS, ultimate tensile strength; YS, yield strength.

2.2 | Metallographic preparation and analysis

The microstructure of the materials was examined using SEM images. Before SEM imaging, the surfaces were ground to European grit P4000, polished to 1 μm diamond suspension, and etched in 2 vol% Nital solution for 5–6 s. The Nital solution was prepared by adding 2 ml of 67–70 wt% HNO_3 into 100 ml of ethanol.

The ferrite–cementite interfacial area, S_v, the mean free path between cementite particles, λ_p, and the mean true spacing for lamellar materials, σ_0, were calculated as described by Johnson and Krauss;[13] $S_v = 4N$ where N is the number of particles or platelets intercepted per unit of length of a test line, $\lambda_p = (1-f)/N$, where f is the volume fraction of cementite, calculated with the lever rule and assuming all C is located in cementite, Fe_3C, and $\sigma_0 = 2/S_v$. For each material, N was determined from four images of the middle of cross-sections and four images in the middle of the wires in the width-length plane. Five horizontal and five vertical test lines were measured for each image, that is, 20 lines were used to find the average number of cementite interceptions on the test lines in the thickness and length directions while 40 lines were used to find the average number of cementite interceptions in the width direction. SEM images with magnifications varying from ×5000 to ×50 000 were used, depending on the grain size and size of lamellas or cementite particles. All materials were evaluated at ×20 000 and at least one other magnification.

The tortuosity of the hydrogen diffusion path in the electrochemical hydrogen permeation experiments was determined by examining cross-section micrographs. In the electrochemical hydrogen permeation experiments, hydrogen diffuses in the direction of the thickness, and the tortuosity was therefore only studied in through-thickness. Image analyses were first conducted by examining micrographs from three positions in the cross-sections at ×10 000. One to three images were analyzed for each position. For each image, a red line was drawn from side to side, in the direction of diffusion during electrochemical permeation tests, and the number of red pixels was divided by the number of pixels between the two sides of the image. An example is shown in Figure 3. The red line was chosen to start at a point where it was clear that the shortest path of diffusion was seen inside the image. Each line was drawn straight until it reached a particle or lamella, then the necessary steps were taken to avoid the obstacle and before it continued in a straight line. The number of pixels in a line was then equal to the number of pixels from one side of the image to the other plus the number of extra pixels drawn to overcome obstacles. For some images, especially the ones with spheroidized carbides, several lines could be drawn without the lines going through the same grains. The same

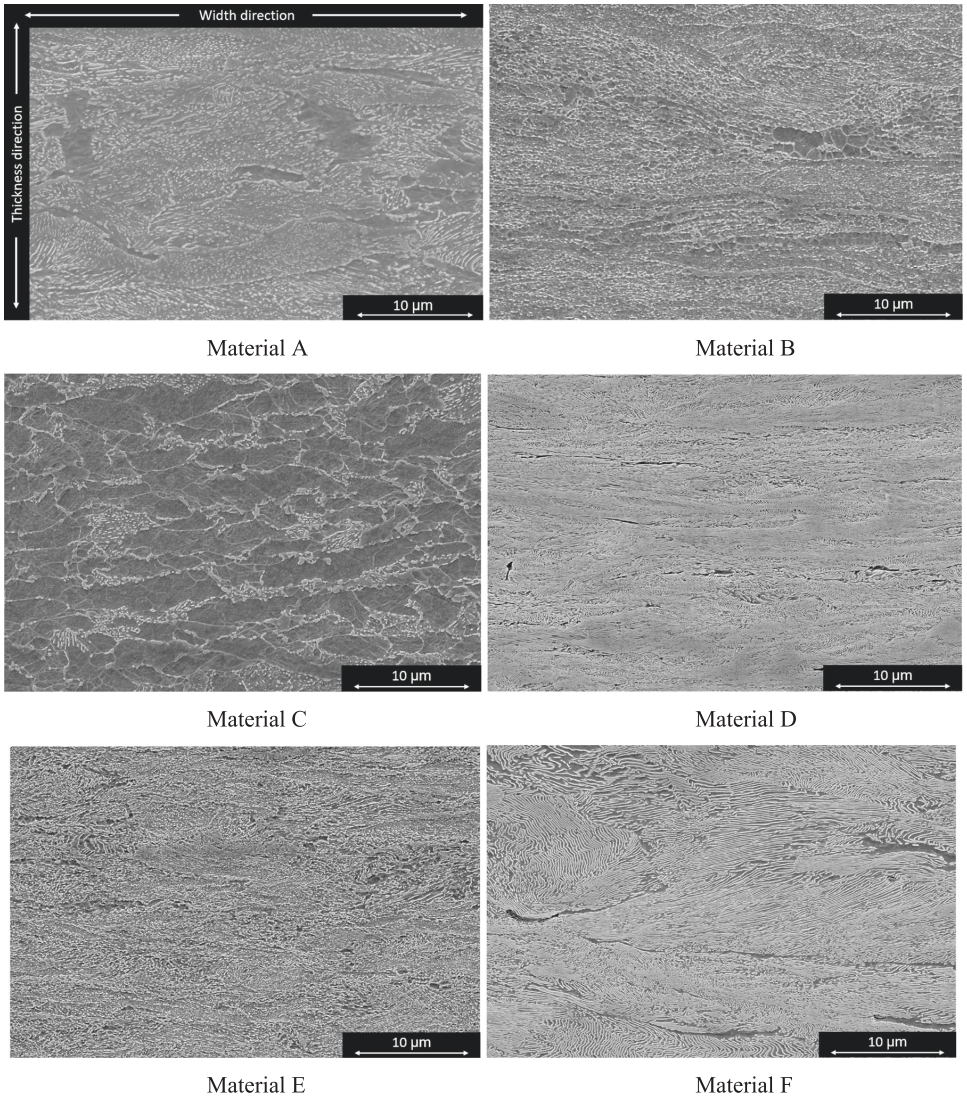

FIGURE 1 Scanning electron microscopy images illustrating the microstructure of the wires, as indicated. The orientation of the images is indicated in the image of Material A

image was then sometimes used to find two lines. All the materials had at least two lines drawn for each of the three positions. More images were analyzed for the materials with the highest data variance. This method has been shown sensitive to the image resolution, and the first screening was therefore conducted with images in the same magnification for all the materials. A second screening was conducted for Materials D and F, where Material D was evaluated at ×20 000 and Material F at ×5000. The images were distributed more evenly around the cross-section in the second screening.

2.3 | Electrochemical hydrogen permeation experiments

The hydrogen uptake and diffusion coefficients of the materials were determined by electrochemical hydrogen permeation experiments, similar to the experimental configuration described by Devanathan and Stachurski.[24] The cell consisted of two compartments separated by the steel specimen in the middle. The principle behind the method is to charge the sample with hydrogen on one side and detect

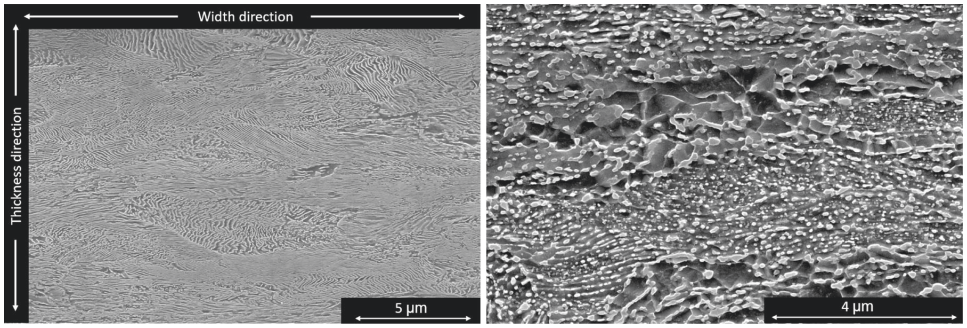

FIGURE 2 Scanning electron microscopy images of Materials D and E

TABLE 2 Mechanical and microstructural properties of the wire materials

Material	Extent of plastic deformation	Cementite morphology
A	Some deformation	Globular, partly lamellar
B	Pearlite deformed. Some banding of ferrite	Globular
C	Some banding and deformation	Globular
D	Highly deformed grains	Lamellar
E	Pearlite deformed. Some banding of ferrite	Globular, partly lamellar
F	Some deformation of pearlite. Ferrite heavily deformed	Lamellar

	Estimated grain size					
Material	Ferrite (µm)	Cementite (µm)	Hardness (HV_{10})	YS (MPa)	UTS (MPa)	Ep
A	≤14	≤36	331 ± 14	871	1009	0.115
B	≤10	≤28	290 ± 10	805	847	0.157
C	≤20	≤14	257 ± 4	616	744	0.152
D	≤7	≤24	453 ± 16	1408	1622	0.094
E	≤3	≤22	386 ± 8	1097	1260	0.108
F	≤20	≤32	384 ± 6	1252	1408	0.099

Abbreviations: Ep, plastic strain-to-failure; UTS, ultimate tensile strength; YS, yield strength.

electrochemically the hydrogen that has diffused through the specimen on the opposing side, Figure 4.

2.3.1 | Sample preparation

Since the microstructures of the wires were anisotropic, it was decided to keep the materials in their original thickness, although some material was lost due to grinding. The sample thicknesses ranged from 2.54 to 2.85 mm, ideally leading to a circular exposed area of 28.5 mm radius to fulfill the desired minimum 10:1 radius-to-thickness ratio, as recommended by ISO 17081[25] and ASTM G148[26] to guarantee one- dimensional (1D) diffusion through the thickness. Maintaining the preferred radius was not possible since the width of the wire was 12 mm or smaller. Thus, the wires were embedded in a light-curing resin (Technovit® LC 2000) mixed with its optional additive "Inside Cure" to maximize the exposed area. An embedded sample is shown in Figure 5. All sample sides were ground with SiC paper, washed in acetone, and sonicated in ethanol before mounting. The two sides exposed in the permeation cell were ground to European grit P1200 SiC paper before the samples were heated to 120°C in a heating cabinet overnight, to reveal sites with bad adhesion between the steel and embedding. Any sites with poor adhesion between the polymer and steel were visible after heating and only defect-free samples were used in the tests. Before exposure in the test cell, the samples were coated

with palladium on one side by electrodeposition according to the procedure proposed by Bruzzoni[27] and described in detail by Husby et al.[14] After the samples were coated with Pd, they were heated to 120°C in a heating cabinet for at least 16 h to remove any hydrogen that may have been absorbed by the samples during the Pd-coating process and diffused to irreversible traps. This procedure was used by Rivera et al.[28] who exposed the samples to 110°C. In the absence of a palladium coating on the hydrogen exit side (i.e., anodic side), the steady-state permeation current can decrease with time.[29–31] This drop in steady-state permeation current may be acceptable for experiments expected to last a few hours, but for the thick samples used in this study, a palladium coating on the hydrogen exit side was considered necessary. The hydrogen entry side was left uncoated and re-ground with European grit P1200 SiC paper, rinsed in distilled water, and dried with hot air just minutes before the electrochemical hydrogen permeation experiments.

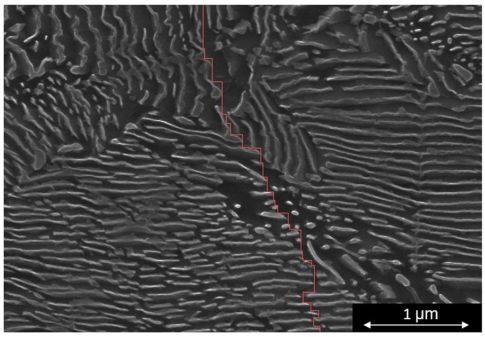

FIGURE 3 Example of a line drawn to estimate the tortuosity of the hydrogen diffusion path in Material F. The image is shown here is cropped and magnified to improve the visibility [Color figure can be viewed at wileyonlinelibrary.com]

2.3.2 | Measurement of hydrogen permeation transients

The sample was placed in the sample holder and the screw was inserted to make electrical contact, as shown in Figure 4. Gaskets were placed on both sides of the sample before the glass compartments and the clamping system was mounted around the sample. Both compartments of the cell were filled with 0.1 M NaOH and constantly purged with nitrogen gas to remove oxygen, as recommended for carbon steels in ISO 17081.[25] Each compartment had mercury–mercurous electrode (MME) ($Hg/Hg_2SO_4/SO_4^{2-}$) in saturated K_2SO_4 solution as a reference and a platinum wire as a counter electrode. The potential of the MME electrode is +650 mV versus the normal hydrogen electrode. Hydrogen was introduced by galvanostatic polarization using an applied

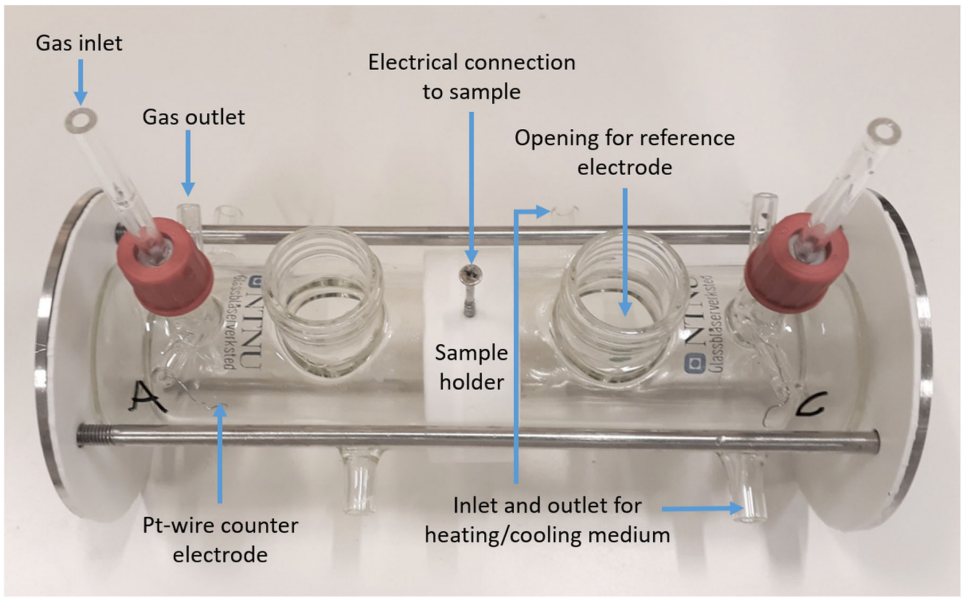

FIGURE 4 Electrochemical hydrogen permeation cell [Color figure can be viewed at wileyonlinelibrary.com]

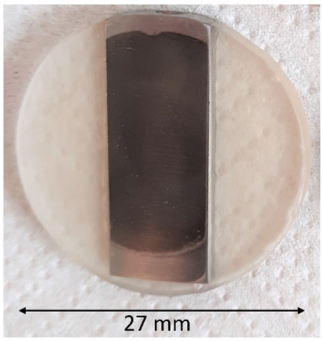

FIGURE 5 Electrochemical hydrogen permeation sample. The translucent part of the sample is the embedding. The dark area of the sample was coated with Pd and exposed facing the anodic side of the hydrogen permeation cell [Color figure can be viewed at wileyonlinelibrary.com]

current, $i_{app} = -12$ mA cm^{-2}. This compartment will be described as the cathodic compartment and the corresponding side of the sample as the cathodic side. In the other compartment, that is, the exit or anodic compartment, the sample was anodically polarized to −110 mV versus MME (+300 mV vs. SCE or +340 mV vs. Ag/AgCl sat. KCl). The experiments started with stabilizing the surfaces in both compartments to −110 mV versus MME until the current on the anodic side was lower than 0.1 μA cm^{-2}. Then, galvanostatic charging started on the cathodic side. When hydrogen reached the anodic side, the current increased until steady-state diffusion was reached and the current on the anodic side stabilized. The galvanostatic charging was then stopped and hydrogen removed from the test sample by anodic polarization at −110 mV vs. MME on both sides, which is referred to as discharging or decay transient. When the anodic side reached a current density below 0.1 μA cm^{-2}, the galvanostatic charging was re-started and the new hydrogen charging transient was measured. A second decay transient was recorded after steady-state diffusion was reached. Water at 25 ± 1°C was circulated through the jacket of the anodic and cathodic compartments of the cell.

2.3.3 | Analysis of the results

The electrochemical hydrogen permeation experiment is designed to have 1D hydrogen diffusion, a linear gradient of lattice hydrogen concentration in the material at a steady state, and a diffusible hydrogen concentration equal to zero on the anodic side.[25,26] It is assumed that during steady-state permeation, the hydrogen traps are occupied and in equilibrium with the lattice concentration so that lattice hydrogen diffusion dominates. There may be obstacles to hydrogen diffusion through which hydrogen cannot diffuse.[32] Cementite is considered to be an example of this kind of obstacle for hydrogen diffusion, besides contributing to increased hydrogen uptake by trapping on the cementite–ferrite interfaces.[13,33] Hydrogen diffusion inside any cementite phase in ferritic–pearlitic steels can therefore be neglected. Thus, hydrogen diffusion in the lattice during steady-state is expected to be governed by the theoretical diffusion coefficient of ferrite, D_l. The permeation flux at steady-state, J_{SS}, depends on the length of the hydrogen pathway through the sample, L, and the subsurface concentration of hydrogen in lattice sites at the entry side, C_0. Since the lattice hydrogen is expected to be present mainly in ferrite and the materials contain both ferrite and cementite, the subsurface concentration of hydrogen is denoted C_0^{av} here, to emphasize that the concentration is based on the assumption of equal distribution of lattice hydrogen over the hydrogen entry surface.[34]

$$J_{SS} = \frac{D_l C_0^{av}}{L}. \quad (1)$$

C_0^{av} must be divided by the volume fraction of ferrite to find the subsurface concentration of lattice hydrogen in the ferrite phase, C_0^{Fe}.[34]

$$C_0^{Fe} = \frac{C_0^{av}}{1\text{-}f} \quad (2)$$

Similarly, J_{SS} reflects the average flux of hydrogen while J_{SS}^{Fe} is introduced to quantify the flux of hydrogen in the ferrite phase, assuming no hydrogen flux in the cementite

$$J_{SS}^{Fe} = \frac{D_l C_0^{Fe}}{L} = \frac{J_{SS}^{av}}{1-f}. \quad (3)$$

In the range −40°C to 80°C, D_l for ferrite is given by[35]

$$D_l = 7.23 \times 10^{-8} \exp\left(\frac{-Q}{RT}\right) \text{m}^2\text{s}^{-1} \quad (4)$$

where $Q = 5.69$ kJ mol^{-1} and R is the gas constant 8.314 J K^{-1} mol^{-1}. This gives $D_l = 7.28 \times 10^{-5}$ cm^2 s^{-1} at 25°C. When only reversible trapping sites are present and the trap occupancy is low, the concentration of hydrogen in lattice and reversible trapping sites, C_{0R}, can be estimated by reformulating Equation (1) and using the effective diffusion coefficient, D_{eff}, which accounts for the effect of trapping on diffusivity.[25]

$$C_{0R} = \frac{J_{SS}L}{D_{eff}} = \frac{I_{SS}L}{A_{surface}FD_{eff}}. \quad (5)$$

Here, I_{SS} is the steady-state permeation current measured on the anode side, $A_{surface}$ is the exposed surface area, and F is Faraday's constant equal to 96485 C mol^{-1}. D_{eff} can be determined in several ways. One way is to use the breakthrough time, t_b, which is determined by extrapolating the linear portion of the rising permeation transient to zero permeation flux. The breakthrough method gives the following relationship[36]

$$D_{eff} = \frac{L^2}{19.8t_b}. \quad (6)$$

The so-called time-lag method is another approach where D_{eff} is obtained based on the time elapsed when the permeation flux J(t) has reached $0.63 \times J_{SS}$. This time is defined as t_{lag} and D_{eff} follows:

$$D_{eff} = \frac{L^2}{6t_{lag}}. \quad (7)$$

Another approach involves estimating D_{eff} by plotting $-\ln((J_{SS} - J(t))/J_{SS})$ versus t, which should have a gradient of $1/t_0$ where $t_0 = L^2/(\mu^2 D_{eff})$.[24] The same slope should be obtained for the decay transient when plotting $-\ln(J(t)/J_0)$ versus t, where J_0 is the current at the start of the decay transient, that is, the J_{SS} of the rising transient. Inside the materials, there may be traps with such high binding energy that the hydrogen trapped is unlikely to escape during the permeation test.[12] These traps are considered irreversible and the hydrogen trapped will not be part of the diffusible hydrogen. During the first transient, t_b and t_{lag} can be increased by the presence of irreversible traps and therefore the second transients will be used in the breakthrough and time-lag methods.

Zakroczymski[37] derived the following equation for the permeation flux on the anodic side during decay transients when both the cathodic and anodic sides of the permeation cell are under anodic polarization,

$$\frac{J(t)}{J_\infty} = 1 - \frac{2L}{(\mu D_{eff}t)^{1/2}} \sum_{n=0}^{\infty} \exp\left(-\frac{(2n+1)^2L^2}{4D_{eff}t}\right). \quad (8)$$

D_{eff} was obtained as the value that minimized the sum of the squared error between Equation (8) and the experimental points. The first 100 terms in the series in Equation (8) were calculated. Normally, L is assumed equal to the sample thickness,[25,26] but for materials where the diffusion path of hydrogen is tortuous, a tortuosity factor can be added which relates the real diffusion distance L to the sample thickness L_0. Here, the tortuosity factor, τ, is defined as in[38]

$$\tau = \frac{L}{L_0}. \quad (9)$$

An alternative definition of tortuosity is $\omega = D_{eff}/D_\alpha$.[34] The multiple definitions can lead to confusion since a tortuous diffusion path gives $\tau > 1$ and $\omega < 1$. Using τ is more practical than ω when finding the tortuosity factor from images and was therefore chosen for this study.

3 | RESULTS

3.1 | Microstructure

The ferrite–cementite interfacial area, S_v, mean free path between particles, λ_p, and mean true spacing between lamellae, σ_0, are given in Table 3. The standard deviations of S_v, λ_p, and σ_0 depend on the standard deviation of N which was calculated assuming no

TABLE 3 Tortuosity factors, ferrite–cementite interfacial area, mean free path between cementite particles, and mean true spacing for lamellar materials, found by image analyses

Material	τ	S_v (μm^{-1})	λ_p (μm)	σ_0 (μm)
A	1.122 ± 0.036	8.521 ± 1.901	0.434 ± 0.097	N.A.
B	1.055 ± 0.010	8.022 ± 2.975	0.480 ± 0.178	N.A.
C	1.056 ± 0.022	3.066 ± 2.176	1.239 ± 0.879	N.A.
D	1.669 ± 0.266	30.761 ± 2.421	N.A.	0.065 ± 0.005
E	1.158 ± 0.015	15.237 ± 1.345	0.240 ± 0.021	N.A.
F	2.035 ± 0.344	16.758 ± 3.316	N.A.	0.119 ± 0.024

Note: Error was estimated as the standard deviation.

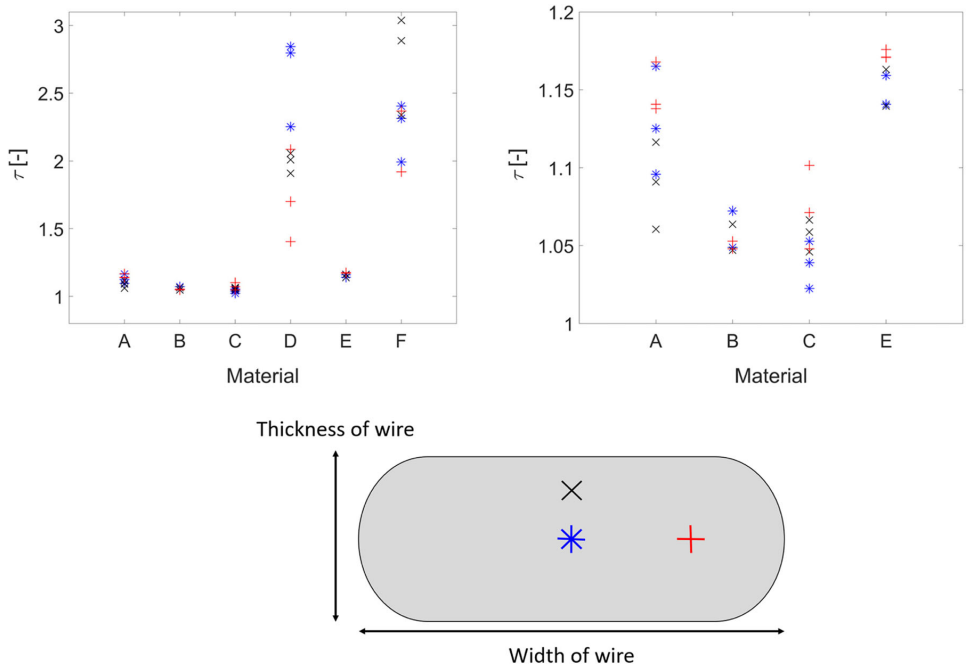

FIGURE 6 First estimation of tortuosity factors from images of ×10 000 in three different areas of the cross-sections. The areas are indicated in the lower illustration [Color figure can be viewed at wileyonlinelibrary.com]

covariance between the number of intercepts in the length, width, and thickness directions. Materials A and B had similar S_v and λ_p values despite having very different microstructures: The carbon content of A was almost twice as high as that of Material B, and Material A had ferrite grains distributed more evenly around the pearlite grains than Material B. Material C had the lowest S_v and highest λ_p while Material D had the highest S_v. Materials E and F had similar S_v, but otherwise substantially different microstructures. Material F had lamellar carbides, and ferrite grains in lines extending over 20 μm whereas Material E had a very fine microstructure with mainly small round carbides and smaller ferrite grains than Material F.

Figure 6 shows the tortuosity factors estimated for all materials with ×10 000 magnification images. The materials appeared relatively equiaxed in the width-length plane and a hydrogen diffusion obstacle was therefore considered to be equally difficult to overcome in the length as the width dimension. Hence, the 2D diffusion paths found in the images were considered representative of the 3D diffusion paths in the wire materials. The tortuosity was highest for the lamellar materials, D and F, and lowest for the materials with the lowest carbon contents and roundest carbides, B and C. The tortuosity measurements were highly scattered for Materials D and F, while they were least scattered for the materials with the finest carbide distribution, Materials B and E. For Material D, the lamellas were often blurred at ×10 000 and the evaluation of the diffusion path at this magnification was difficult. A second screening was therefore

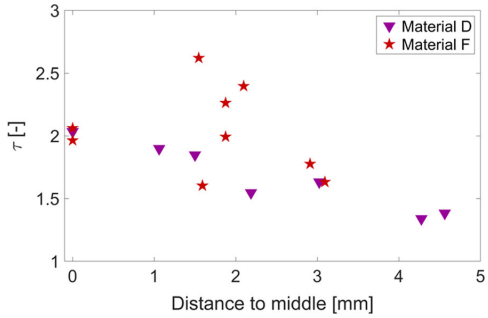

FIGURE 7 Second estimation of tortuosity factors for Materials D and F. Images of ×20 000 were used for Material D while images of ×5000 were used for Material F [Color figure can be viewed at wileyonlinelibrary.com]

conducted for Material D with images taken at a higher magnification. Due to the large grain size of Material F, few grains were visible in each image taken at ×10 000 magnification and the tortuosity evaluated from these images was more sensitive to grains of tortuous orientation than the evaluation of images with a higher number of grains. The tortuosity of Material F was therefore investigated again at a lower magnification. The second time the tortuosity of Materials D and F was investigated, the images were captured in several positions distributed over the cross-section at a ×20 000 magnification for Material D and ×5000 for Material F. The graph in Figure 7 displays the measured tortuosity factor versus the approximate distance to the middle of the cross-section. Notice that the distance to the middle does not represent the distance to the outer surface, since the wires have rectangular shapes with rounded corners. Material D was wider than Material F and had therefore some measurements further from the middle than Material F. At both ×10 000 and ×20 000, the tortuosity in Material D was the highest in the middle and decreased as the distance to the middle increased. For both materials, the tortuosity factor decreased when the magnifications were optimized for each of them separately. The tortuosity factors of the materials are given in Table 3.

3.2 | Electrochemical hydrogen permeation experiments

Using 0.1 M NaOH in the cathodic compartment of the hydrogen permeation cell was not ideal for the measurement of hydrogen diffusivity and hydrogen uptake in the wire materials. Before the first transient and between the first and second transients, the samples were anodically polarized on both sides and since the cathodic sides of the samples were not coated with Pd, an oxide layer can be formed on the surface, influencing diffusion.[39,40] The rising transients observed when charging carbon steel samples in 0.1 M NaOH are usually shallower than Fick's law, and this environment is therefore advised against carbon steels. More advice on charging environments for electrochemical hydrogen permeation tests can be consulted in the appendix of ISO 17081[25] and ASTM G148.[26]

The hydrogen permeation transients and decays are given in Figures 8–13. Irreversible trapping of hydrogen will give a slower diffusion during the first transient than the second transient, but the steady-state permeation currents are expected to be the same. The current of the second transients was however smaller than that of the first transients, probably as a result of oxide formation during anodic polarization on the cathode side. In this study, the oxide formation was expected to be more apparent for the second rising transient than the first, as the stabilization time before the first transient was around 24 h while the decay between the first and second transient lasted at least 3 days. The steady-state currents were estimated from the first transients since these were expected to be less affected by oxide formation on the cathodic side. However, since the current did not fully stabilize for most of the materials, the steady-state currents were defined as the current of the first transient after 93 h of exposure.

Logarithmic plots of normalized rising and decay transients are shown in Figure 14. For the rising transients, the normalized hydrogen permeation flux is $A = (J_{SS} - J(t))/J_{SS}$. For the decay transients, the normalized permeation flux of the decay transients is $A = J(t)/J_0$, where the current at the start of a decay transient, J_0, is equal to the J_{SS} of the preceding rising transient. According to Devanathan and Stachurski,[24] D_{eff} can be determined from the slope of the normalized transient:

$$\ln A = \ln 2 - \frac{\mu^2 D}{L^2} t. \tag{10}$$

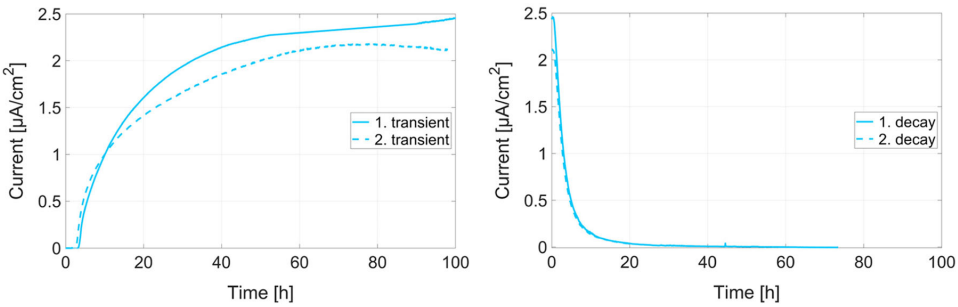

FIGURE 8 Electrochemical hydrogen permeation curves of Material A [Color figure can be viewed at wileyonlinelibrary.com]

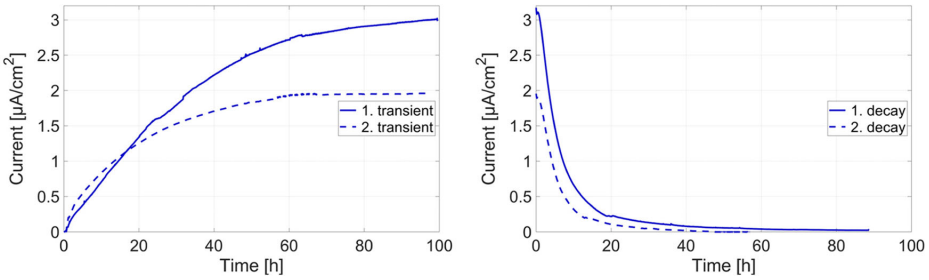

FIGURE 9 Electrochemical hydrogen permeation curves of Material B [Color figure can be viewed at wileyonlinelibrary.com]

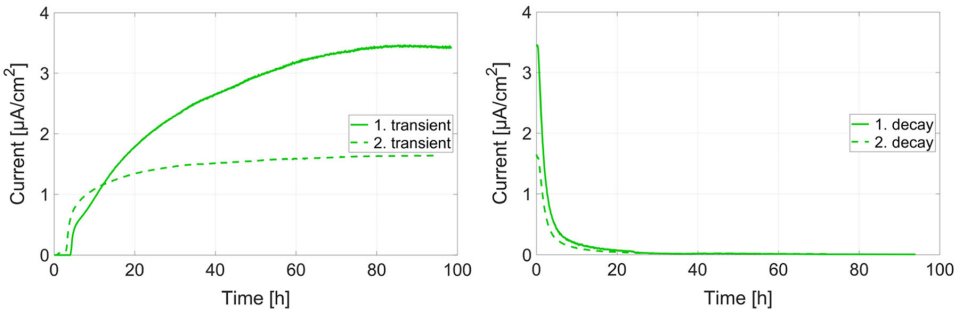

FIGURE 10 Electrochemical hydrogen permeation curves of Material C [Color figure can be viewed at wileyonlinelibrary.com]

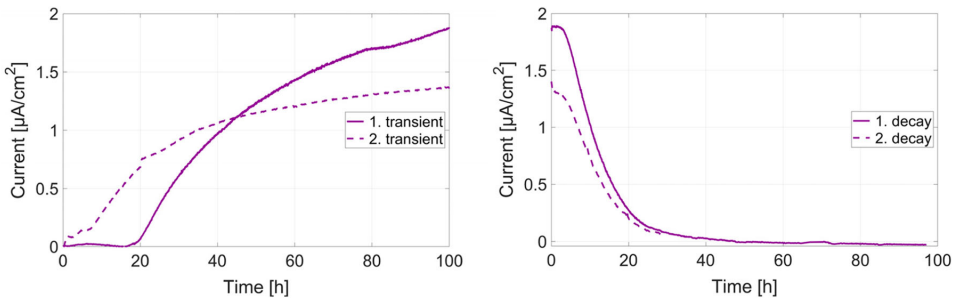

FIGURE 11 Electrochemical hydrogen permeation curves of Material D [Color figure can be viewed at wileyonlinelibrary.com]

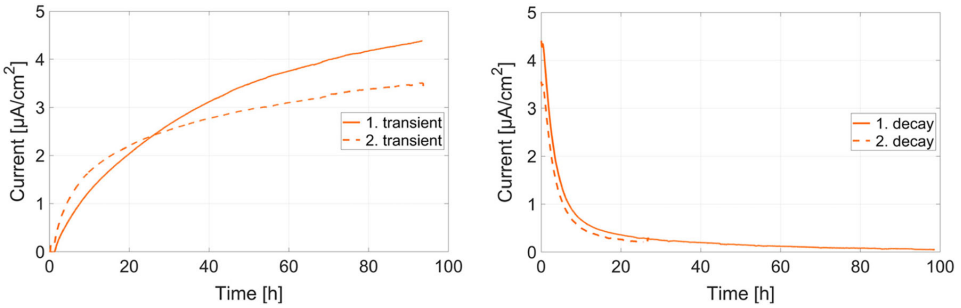

FIGURE 12 Electrochemical hydrogen permeation curves of Material E [Color figure can be viewed at wileyonlinelibrary.com]

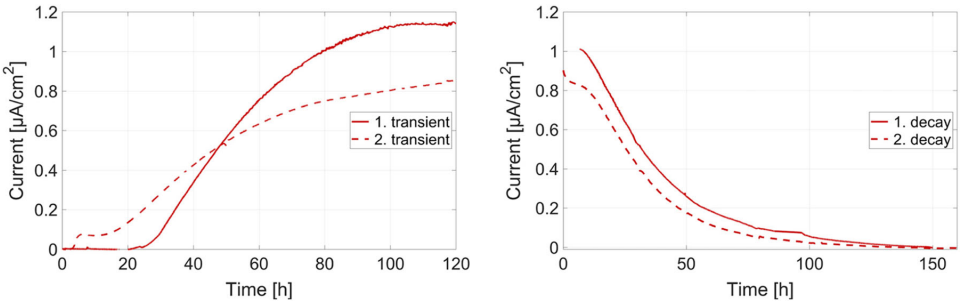

FIGURE 13 Electrochemical hydrogen permeation curves of Material F. A noisy signal was observed during the first 8 h of the first decay—these data have been removed [Color figure can be viewed at wileyonlinelibrary.com]

Notice that the decay rates in Figure 14 departed from linearity for long exposure times. The deviation from linearity could be due to the additional hydrogen diffusion out from the originally cathodic sides.[15] The diffusion coefficients were therefore estimated in the linear regions closer to the start of the decays. For Materials A, B, C, and E the linear portion of the decay occurred before 10 h, whereas the corresponding region for Material D was 10–24 h and 20–60 h for Material F. For each material, D_{eff} was calculated by several methods and the results are given in Table 4. The D_{eff} values calculated by t_{lag}, t_{b}, and slope method from the second transients differed and the reasons for this will be further elaborated in Section 4. The D_{eff} values found using the slope method on the two decay transients were consistent. An acceptable agreement was also found for D_{eff} values calculated by fitting Equation (8) to decay transients 1 and 2, and unlike the slope method, this model fitted the entire decay transient, Figure 15. The D_{eff} values calculated from the decays tended to decrease with increasing S_{v} as displayed in Figure 16.

The diffusion coefficients, D_{eff}, estimated using Equation (8) on both decay transients were used to calculate the trapped $C_{0\text{R}}$ and lattice hydrogen (C_0^{Fe}) concentrations. Equation (8) was chosen for D_{eff} calculations because the boundary conditions used in the slope method were valid only for short times while Equation (8) considers that hydrogen is removed from both sides of the sample during the decay transients and is, thus, valid throughout the duration of the decay transients, Figure 15. Lattice and reversible hydrogen concentrations are given in Table 5 along with I_{SS}, which was estimated from the current after 93 h of charging, and the normalized steady-state permeation flux $J_{\text{SS}}L$. The subsurface concentration of lattice hydrogen showed a small difference between the C_0^{av} and C_0^{Fe} values, because the volume fractions of cementite were low, Tables 1 and 5. The choice of C_0^{av} or C_0^{Fe} does not affect the ranking in lattice hydrogen concentration. $J_{\text{SS}}L$ is plotted versus λ_{p}, and σ_0 in Figure 17, showing a lack of a clear trend between permeability and cementite or platelet distance, and hence, no indication of uncompensated tortuosity effects.

4 | DISCUSSION

4.1 | Tortuosity

The effect of cementite increasing the hydrogen diffusion path in steels is often neglected in electrochemical hydrogen permeation experiments; nonetheless, several studies, especially for steels with both ferritic and austenitic phases, have shown the need to evaluate tortuosity effects of secondary phases.[12,32,34,38,41–44] For simpler, homogenous materials, the effect of tortuosity can be modeled using the grain size and shape, and orientation of the secondary phases. For example, Turnbull and Hutchings[34] estimated the tortuosity of the diffusion path by using equations originally developed in thermal transport models,[45,46] but found a 16% difference in the tortuosity factor depending on which model they used. The complexity of the microstructures in this study made it difficult to find reasonable assumptions for tortuosity models. Thus, image analyses were the preferred method, although they were affected by the choice of image magnification and the possible over or under etching of the surfaces.

The tortuosity factors found by image analyses were the lowest for Materials B and C, which had the lowest carbon contents. The tortuosity factors were about 10% higher for Materials A and E, and more than 50% higher for the lamellar materials D and F. The tortuosity of pearlitic steels has been addressed in many studies.[38,43,47] Forot et al.[38] defined the tortuosity factor as given in Equation (9) and found a tortuosity factor between 20 and 35 for fully pearlitic steel by analyzing transmission electron microscopy (TEM) micrographs. This is much higher than the tortuosity factors found for Materials D and F in this study (i.e., 1.669 and

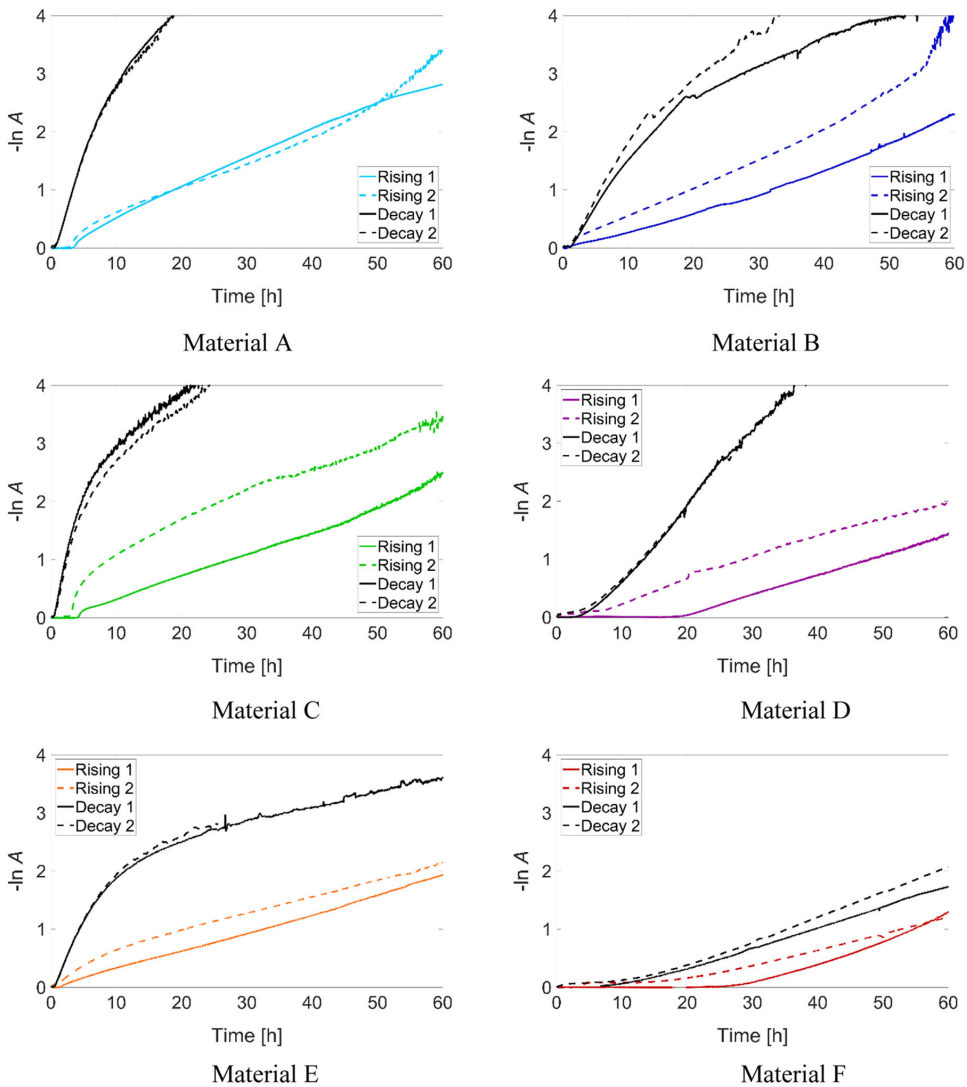

FIGURE 14 Logarithmic rise and decay plots for the electrochemical permeation tests. For the rising transient, $A = (J_{SS} - J(t))/J_{SS}$. For the decays $A = J(t)/J_0$ [Color figure can be viewed at wileyonlinelibrary.com]

2.035, respectively). Several grains in Materials D and F had discontinuous lamellas and this, in addition to the presence of ferritic grains, reduced tortuosity significantly. Another possible reason for low tortuosity factors in our work compared to Forot et al.,[38] is that the TEM images in Forot et al.[38] were obtained at a higher magnification than in our work. In this regard, as shown in Figures 6 and 7, the tortuosity factor is affected by the magnification. When the images were captured at a magnification where few grains are seen in each image, the perceived possible diffusion paths will mainly go through the grain interior, whereas using images of lower magnification allows for seeing diffusion paths along grain boundaries. As we will show in the discussion of the steady-state permeation flux, it is likely that diffusion is occurring on the grain boundaries, supporting the choice of using the tortuosity measured at lower magnifications as long as the discontinuities of the lamellas are still visible. The tortuosity factor of the lamellar materials had the highest standard deviations, which was expected since tortuosity measurements are strongly affected by the orientation of any lamellar grains. The lowest standard deviations were found for Materials B and E, which are the

TABLE 4 D_{eff} calculated with different methods for the second rising and the decay transients

	Using the second transient			Using decays			
Material	D_{eff} (tb) ($cm^2\ s^{-1}$)	D_{eff} (tlag) ($cm^2\ s^{-1}$)	D_{eff} (slope) ($cm^2\ s^{-1}$)	D_{eff} (slope, decay 1) ($cm^2\ s^{-1}$)	D_{eff} (slope, decay 2) ($cm^2\ s^{-1}$)	D_{eff} (Equation 8, decay 1) ($cm^2\ s^{-1}$)	D_{eff} (Equation 8, decay 2) ($cm^2 s^{-1}$)
A	4.20×10^{-7}	2.11×10^{-7}	9.17×10^{-8}	9.06×10^{-7}	9.11×10^{-7}	1.19×10^{-6}	1.16×10^{-6}
B	2.15×10^{-6}	2.23×10^{-7}	1.25×10^{-7}	4.93×10^{-7}	5.22×10^{-7}	7.55×10^{-7}	7.42×10^{-7}
C	3.99×10^{-7}	4.46×10^{-7}	1.33×10^{-7}	1.28×10^{-6}	1.22×10^{-6}	1.81×10^{-6}	1.59×10^{-6}
D	6.48×10^{-7}	3.02×10^{-7}	1.56×10^{-7}	5.94×10^{-7}	6.17×10^{-7}	6.62×10^{-7}	6.59×10^{-7}
E	1.51×10^{-6}	2.01×10^{-7}	7.27×10^{-8}	6.61×10^{-7}	6.92×10^{-7}	9.73×10^{-7}	1.09×10^{-6}
F	3.99×10^{-7}	3.10×10^{-7}	2.60×10^{-7}	2.64×10^{-7}	2.75×10^{-7}	4.01×10^{-7}	4.29×10^{-7}

Note: The tortuosity factors in Table 3 were used to estimate the real hydrogen diffusion distance required for D_{eff} calculations.

materials with the finest carbides and the most homogenous carbide distribution. In the following discussion, the tortuosity factor is used for all materials unless otherwise stated.

4.2 | Diffusion coefficient

The D_{eff} values calculated using the decay transients gave relatively reproducible results. The use of the decay transients for estimating the diffusion coefficient is less common than using the second rising transients since the boundary conditions are harder to define during the decay.[48] However, the hydrogen concentration at the previous entry side is fixed to zero by applying an anodic potential on the previous hydrogen entry side during decay transients.[25,26,48] The hydrogen entry side was not coated with Pd, which can lead to less efficient desorption of hydrogen there compared to the hydrogen exit side and a gentler slope than Equation (8) predicts. A gentler slope is observed for the materials with globular carbides, see Figure 15, and less efficient hydrogen desorption on the hydrogen entry side may have caused this. It is, however, interesting that this has not affected Material D which was charged with hydrogen for as long as Materials A and B. When using the rising transients for calculating D_{eff} (the breakthrough, time lag, and slope methods) the results were inconsistent and often one order of magnitude lower than the diffusion coefficients calculated by the slope method for the decays. The time lag method is dependent on the steady-state current and the D_{eff} will be erroneous if the steady-state current is not achieved. This may have happened to the materials that did not reach steady state during the rising transients. A difference in D_{eff} calculated by different methods can indicate that D_{eff} is dependent on the hydrogen concentration, but the difference can also be related to oxide formation on the cathodic side of the sample when this side is anodically polarized. Zakroczymski[39] explained how the oxide formed on the cathode side of a permeation test sample during exposure to 0.1 M NaOH impedes diffusion, leading to erroneous results. The thickness of the oxide will decrease during charging, and the D_{eff} calculated by the breakthrough method is, therefore, likely to be more affected than the D_{eff} calculated by the time-lag method.[49] Zakroczymski and Szklarska-Smialowska[40] showed that the oxide effect can be reduced by charging the sample for 90 h before partial permeation decay and rising transients to estimate D_{eff}. In our work, the steel surfaces were charged for a minimum of 93 h before the decay, but instead of doing a series of partial decay and rising transients, the decay was kept until a steady state was reached. The first decays were kept for a minimum of 73 h before a new transient was measured. During the decay, the surface changes, and the longer the decay lasts, the longer it will take for the current to reach a steady state again.[39] This can explain why Material A, which had the shortest first decay, was the material where the second transient was closest to reaching the same current density as the first transient. The other materials had at least 96 h of decay between the two transients. The current densities in the second transients did not reach the same magnitude as the current densities in the first transients, but this does not appear to affect the diffusion coefficients calculated with the decays. The second decays gave D_{eff} values with less than 14% deviation from those calculated from the first decays. Materials A, B, and D had the lowest deviations, below 3%.

All the equations for D_{eff} used in this paper are based on the assumption that Fick's second law is applicable. For the rising transients, it appears that the oxide formation interferes with the hydrogen flux and makes the

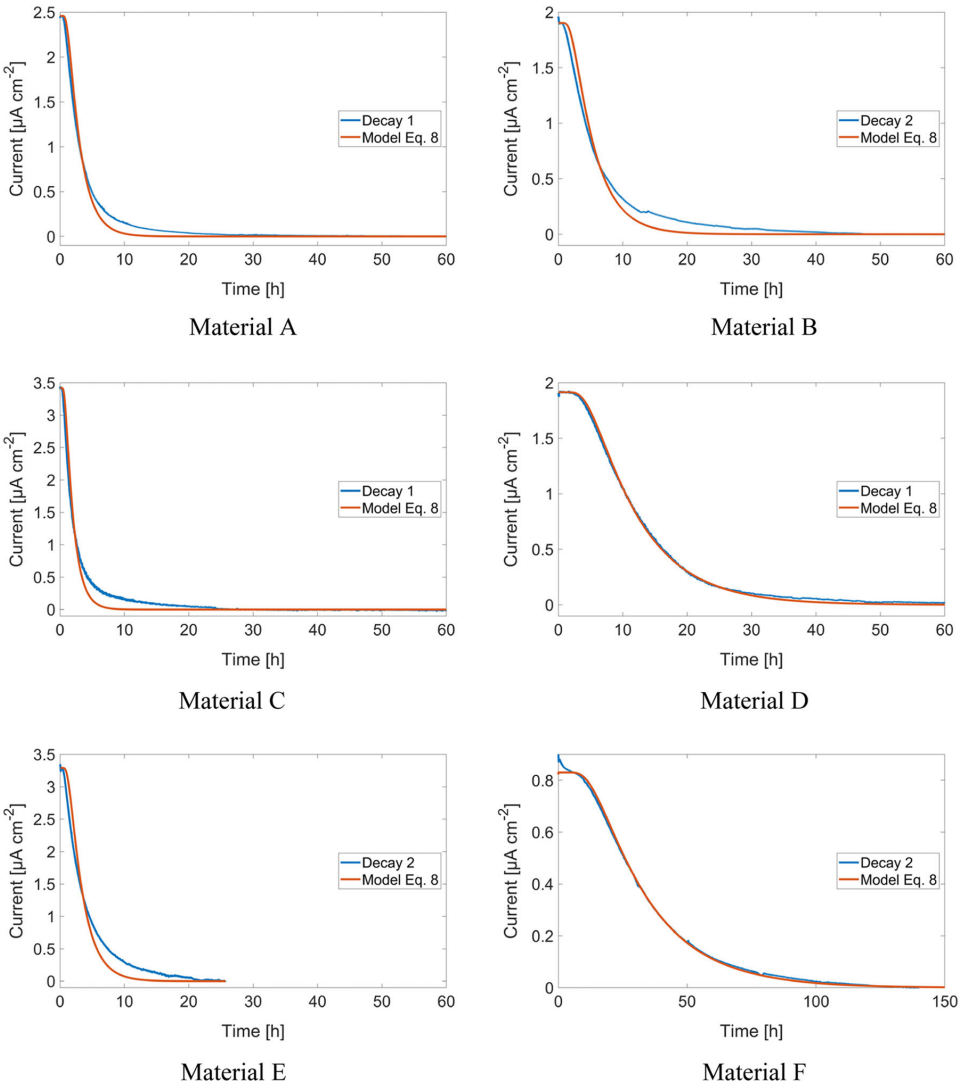

FIGURE 15 Hydrogen permeation decay transients and fitted Equation (8). For each material, the decay with the best fit is displayed [Color figure can be viewed at wileyonlinelibrary.com]

D_{eff} calculations invalid. For the decays, the models fitted using Equation (8) showed a good fit with most of the decay transients, Figure 15. The fit was best for Materials D and F, and least good for Materials B and E which had slightly less steep transients than what Equation (8) predicts. This indicates that oxides on the hydrogen entry side were slightly affecting the permeation during the decay transients for these two materials. The relatively good fit between decay transients and the fitted models indicates that D_{eff} is not dependent on the hydrogen concentration in the material and that Fick's second law is applicable for the decays. When D_{eff} is dependent on trap occupancy, it will increase as the trap occupancy increases and the transients will show a steeper transient than the fitted models.[12] The trap occupancy decreases with time during the decay transients, meaning that the hydrogen trap occupancy is higher for the data used in the slope method for decays than it is for the datasets fitted to Equation (8). The D_{eff} values found using the slope method on the decays were 6%–37% lower than the

D_{eff} values found by curve fitting, which shows that D_{eff} was increasing with decreasing trap occupancy. This is an indication of unsteady surface conditions,[26] and can be related to the oxides on the cathodic side, although the relatively good fit with Equation (8) shows that unsteady state conditions do not appear to have decreased the fit so strongly. Despite the uncertainty of the D_{eff} values, it is considered useful to compare the D_{eff} of different materials when the D_{eff} values have been calculated in the same manner.[12] When different methods give different D_{eff} values, it can be reasonable to choose the highest D_{eff} since the permeation transients cannot outrun the diffusion.[14,50] D_{eff} found by model fitting to Equation (8) is therefore considered most reliable to use for C_{OR} calculations and for comparing the diffusivity of the materials.

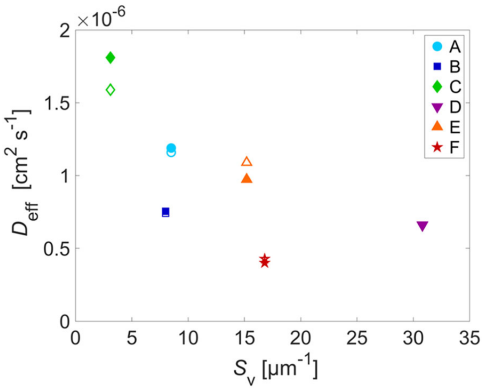

FIGURE 16 D_{eff} of the various wire materials calculated by fitting Equation (8) to the hydrogen permeation decay transients versus the estimated ferrite–cementite interfacial area. D_{eff} values from the first decay transients are shown as filled symbols while D_{eff} values from the second decay transients are shown as unfilled symbols. The tortuosity factor was used for all materials [Color figure can be viewed at wileyonlinelibrary.com]

The D_{eff} values calculated from fitting Equation (8) to the decay transients were plotted against the estimated ferrite–cementite interfacial area in Figure 16. The graphs show that D_{eff} decreased as S_v increased, which is expected to increase hydrogen trapping on ferrite–cementite interfaces.[15] In contrast, Materials B and F had relatively low D_{eff} values compared to the wire materials with similar S_v. Bott et al.[51] discussed the influence of coherency between the ferrite and cementite for the hydrogen trapping in the ferrite–cementite interfaces by conducting hydrogen permeation tests on low-carbon steel heat-treated in three different ways to form a sample consisting of ferrite and pearlite, a sample with spheroidized cementite, and an aged sample with very fine carbide particles. The ferritic–pearlitic steel sample had the highest hydrogen diffusivity, the spheroidized sample showed an intermediate value, and the aged microstructure had the lowest hydrogen diffusivity. The low diffusivity of the steel in the aged condition was attributed to the compressive stress fields surrounding the dispersed particles, which were about 20 nm in diameter and had high coherency to the ferrite matrix. The globular cementite exhibited mainly incoherent carbide–cementite interfaces which gave a lower hydrogen diffusivity and higher hydrogen uptake than the pearlitic microstructure. Both small particles of size approximately 20 nm and larger globular particles were seen for Materials A, B, C, and E studied in this study, but the size distribution of the carbides has not been characterized. Bott et al.[51] suggested that the high diffusivity in the ferritic–pearlitic microstructure indicated that the proeutectoid ferrite on the grain boundaries is the preferential hydrogen diffusion path. This hypothesis is consistent with the observed diffusion coefficients for the lamellar materials in our work: The grain size of Material F was larger than that of Material D and the D_{eff} of Material F lower than that of Material D. The estimation of the tortuosity factors conducted herein considered only what appears to be the shortest diffusion path and did not take into consideration whether some

TABLE 5 Results from the electrochemical hydrogen permeation tests

Material	$J_{SS}L$ (mol cm^{-1} s^{-1})	$J_{SS}^{Fe}L$ (mol cm^{-1} s^{-1})	C_{0R} (using D_{eff} from Equation 8, decay 1) (ppmw)	C_{0R} (using D_{eff} from Equation 8, decay 2) (ppmw)	C_0^{av} (Equation 1) (ppmw)	C_0^{Fe} (Equation 2) (ppmw)
A	7.25×10^{-12}	7.85×10^{-12}	0.69	0.71	0.0127	0.0138
B	9.41×10^{-12}	9.83×10^{-12}	1.59	1.62	0.0165	0.0171
C	1.03×10^{-11}	1.09×10^{-11}	0.73	0.83	0.0181	0.0191
D	7.99×10^{-12}	9.15×10^{-12}	1.54	1.55	0.0140	0.0157
E	1.33×10^{-11}	1.47×10^{-11}	1.74	1.55	0.0233	0.0255
F	6.59×10^{-12}	7.32×10^{-12}	2.09	1.96	0.0115	0.0126

Note: The tortuosity factors in Table 3 were used in the calculations to estimate the real hydrogen diffusion distance.

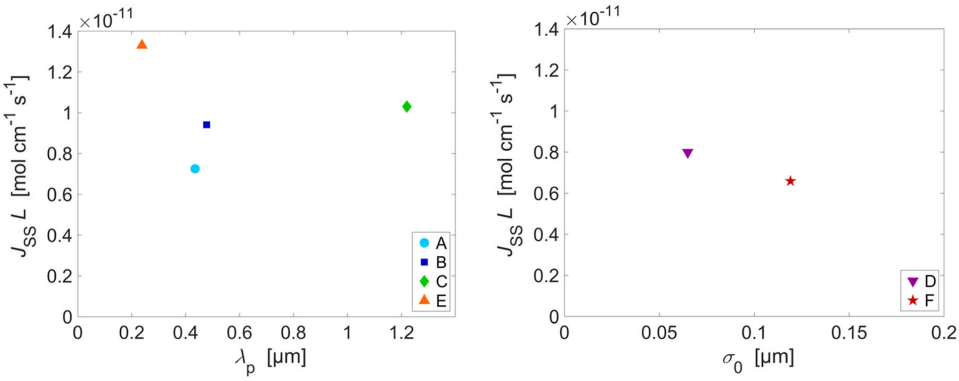

FIGURE 17 Steady-state hydrogen permeation flux versus mean free path between cementite particles for the microstructures with round carbides and versus true mean spacing for the lamellar materials. The tortuosity factor was used in the calculations [Color figure can be viewed at wileyonlinelibrary.com]

paths, for example, grain boundaries, might be preferential for diffusion. The relation between the D_{eff} values and grain sizes of Materials D and F suggested that the estimated tortuosity factor did not correlate with the shortest hydrogen diffusion path in the lamellar materials, but other factors might also affect D_{eff}.

Plastic deformation can affect D_{eff}, as the increased number of dislocations, and hence trapping sites, results in a lower diffusion coefficient.[16–19,52] All the wire materials have grain shapes that indicate plastic deformation, but Materials A and C appeared to be less deformed than the rest. This agrees with the higher D_{eff} values displayed by these materials in comparison with the other materials.

4.3 | Normalized steady-state permeation flux and lattice hydrogen uptake

The normalized steady-state permeation fluxes measured for the materials tended to increase as the grain size decreased. Materials A and F had the largest grain sizes and the lowest $J_{SS}L$ values, while the material with the smallest ferrite grains, that is, Material E, had the highest $J_{SS}L$ value. This can indicate hydrogen trapping on the grain boundaries, but this is questionable since the diffusion coefficients did not decrease with the grain size. Another possibility is that the proeutectoid ferrite is a preferential diffusion path, leading to a tortuosity effect that has not been compensated for.

The steady-state permeation flux is also known to be affected by cold work. Riecke[53] measured the steady-state permeation flux of iron and several steels in recrystallized and cold-worked conditions. For ferrite, the steady-state permeation flux for recrystallized microstructure was the same as 80% cold-worked ferrite. This is in line with the models that consider that trapping should not affect the steady-state permeation flux.[25,26] For fine pearlite, the steady-state flux was not affected by 15% cold work, but 37% cold work led to a decrease in the steady-state permeation flux.[53] Jeng et al.[20] compared the electrochemical hydrogen permeation parameters for pearlitic steels with the same composition and grain size, but different interlamellar spacing. The steady-state flux was the highest for a coarse pearlite microstructure, intermediate for medium pearlite, and the lowest for fine pearlite steel. The observations of both Riecke[53] and Jeng et al.[20] may be related to an increased tortuosity of the hydrogen diffusion path, due to an increased number of obstacles or due to lamellas orienting themselves in the rolling direction. Such a preferential lamella orientation is seen for Material D in our work, Figure 2, and is also indirectly displayed in how the tortuosity of Material D is highest in the middle of the wire, see Figure 7. This trend was not evident for Material F, which had a lower plastic deformation than Material D (i.e., compare the grains in Figure 1) and had a coarser pearlite phase.

There are several studies on how heat treatments affect the steady-state permeation flux. The studies by Luu and Wu[33] on the hydrogen permeation through medium carbon steel with different heat treatments showed that normalized, annealed, and spheroidized microstructures had similar steady-state permeation rates, while the steady-state permeation rate of a quenched martensitic microstructure

was about 50% lower. Similar observations were found by Johnson and Wu.[15] When comparing microstructures, the authors found that the steels with spheroidized carbides had the highest hydrogen permeation flux, while the quenched and tempered microstructure had the lowest one. The same authors found that the hydrogen permeation flux increased with increasing interparticle spacing and decreased as the carbide volume fraction increased by studying annealed steels in more detail. The increase in hydrogen permeation flux with pearlite spacing can be related to increased tortuosity, as discussed above.

Johnson and Krauss[13] found that the steady-state permeation flux increased linearly with the interparticle spacing for austenitized, quenched, and spheroidized AISI 1050 steel samples where only the spheroidizing time varied from sample to sample. However, when testing a sample of the same alloy without the quenching step, the permeation flux was reduced in half. Both microstructures were described as spheroidized carbides and ferrite, and the interparticle spacing, particle radius, and interfacial carbide area were similar for the two materials. Thus, quenching in itself appears to reduce the steady-state hydrogen permeation flux, but a subsequent spheroidizing step increases the steady-state permeation. Possibly, the high permeation rate of the quenched and spheroidized material observed by Johnson and Krauss[13] is related to a smaller grain size associated with additional quenching steps in the production. However, this could not be confirmed since the authors provided no information about the grain sizes of the two materials. In this study, the hydrogen permeation flux did not increase with increasing interparticle spacing and interlamellar spacing, as is shown in Figure 17. In Figure 17, the tortuosity factor was taken into consideration, but even without this factor, there was no clear trend between permeation flux and interparticle or interlamellar spacing. There was no trend between $J_{SS}^{Fe}L$ and the interparticle or interlamellar spacing either, Table 5. This shows that the interparticle and interlamellar spacing had no clear effect on the normalized hydrogen permeation fluxes of the carbon steels when several parameters, like thermomechanical processing and chemical composition, were varied.

4.4 | Hydrogen uptake

The hydrogen uptake in lattice and reversible sites, C_{0R}, was calculated using Equation (5) with D_{eff} from Equation (8) using both the first and second decay transients. C_{0R} is therefore directly linked to the steady-state permeation flux and diffusion coefficients discussed in the previous sections. The relationship between D_{eff} and S_v suggested considerable hydrogen trapping on ferrite–cementite grain boundaries and the $J_{SS}L$ values showed higher hydrogen uptakes as the grain size decreased; nevertheless, C_{0R} did not follow either of these trends. C_{0R} was the lowest for Materials A and C, and about twice as high for Materials B, D, E, and F. The differences in C_{0R} may be related to plastic deformation since Materials A and C appeared less deformed than the others.

The effect of plastic deformation on the HE of iron and carbon steels has been the subject of several studies.[16–19,21,28,52,54–56] Deformation is expected to affect permeation by increasing the density of trapping sites like microvoids, vacancy clusters, and dislocations.[16–18,52] Ha et al.[18] performed electrochemical permeation tests of cold-worked steels and found that the trap density increased almost 10-fold when the material was subject to 10% reduction. The results also showed that the trap density increased by rolling while the trap occupancy was not altered. Nagumo et al.[17] used thermal desorption spectroscopy to compare the hydrogen uptake of eutectoid steel and found four times higher hydrogen uptake for material with 25% drawing reduction compared to the same material with 0% drawing reduction. The microstructure of the steel consisted of fine lamellas of cementite and ferrite with a spacing of 60 nm, which is similar to the microstructure of Material D in this study. After annealing, the amount of hydrogen substantially decreased. The hydrogen uptake decreased from 8 to 3 ppmw for samples annealed at 600°C. Even at annealing temperatures where the hardness of the material was just slightly affected, the hydrogen uptake decreased by about 25%. From the microstructure images in Figure 1, Materials A and C appeared less deformed while Materials B, D, and E had a more deformed microstructure. This indicates that the deformation plays a more important role in the relative hydrogen uptakes of the steel wires than the grain size and ferrite–cementite interface area.

5 | CONCLUSION

This paper compared the electrochemical hydrogen permeation experiments of materials used in industrial components as a function of microstructure. The tortuosity of the hydrogen diffusion path in the materials was estimated by analyzing SEM micrographs. The calculated tortuosity, multiplied by the membrane thickness, yielded the real diffusion distance required for subsequent analyses.

The electrochemical permeation tests were conducted with 0.1 M NaOH in the hydrogen charging environment. This is not recommended for carbon steels, as the rising transients in this environment are usually affected by the formation of oxides on the surface. The decay transients

were less affected by the unstable surface conditions on the hydrogen entry side and were used for the estimation of effective diffusion coefficients.

Several factors affecting hydrogen transport properties were investigated, such as plastic deformation introduced by cold-work, carbide content and distribution, and heat treatments. After compensating for the tortuosity of the hydrogen diffusion path, the hydrogen permeation flux increased with decreasing grain size, but hydrogen trapping on the grain boundaries could not be confirmed by the measured diffusion coefficients. Another possible explanation for the trend between normalized hydrogen permeation flux and grain size is that proeutectoid ferrite may be a preferential hydrogen diffusion path, leading to a tortuosity effect that was not compensated for. The normalized steady-state flux ranged from 6.6 to 7.3×10^{-12} mol cm^{-1} s^{-1} for the materials with the largest grain sizes to 1.3×10^{-11} mol cm^{-1} s^{-1} for the material with the smallest ferrite grain size.

The effective diffusion coefficients were mainly affected by the hydrogen trapping on the ferrite–cementite interfaces. It was also evident that the materials with the lowest amount of plastic deformation had the highest diffusion coefficients. The effective diffusion coefficients ranged from 4.0×10^{-7} to 1.8×10^{-6} cm^2 s^{-1}.

Overall, the most deformed microstructures displayed the highest hydrogen uptake. In this regard, the two materials with less deformed microstructures had hydrogen uptakes in the order of 0.7 ppmw, while the more deformed microstructures had hydrogen uptakes ranging from 1.5 to 2.1 ppmw.

ACKNOWLEDGMENTS

This study was performed as part of the KPN project "Environmental Cracking of Flexible Pipe Armour Wires," Research Council of Norway Project No. 280760 within the PETROMAKS 2 program. The authors would like to thank the following project participants for financial and technical support: The Research Council of Norway, Equinor, Shell, Chevron, Petrobras, OKEA, TechnipFMC, NOV, Baker Hughes, and 4Subsea.

CONFLICT OF INTERESTS

The authors declare that there are no conflict of interests.

DATA AVAILABILITY STATEMENT

The data that support the findings of this study are available from the corresponding author upon reasonable request.

ORCID

Ellen S. Skilbred https://orcid.org/0000-0001-6674-3972
Roy Johnsen http://orcid.org/0000-0002-5449-7396

REFERENCES

[1] E. Remita, F. Ropital, J. Kittel, B. Tribollet, E. Sutter, C. Taravel-Condat, N. Desamais, *CORROSION* 2008, New Orleans, LA **2008**, 4737.
[2] A. Rubin, M. H. Haarh, S. Overby, T. S. Nielsen, J. Gudme, *CORROSION 2012*, Salt Lake City, Utah **2012**, 4002.
[3] A. Dugstad, S. Palencsár, T. Berntsen, L. Børvik, *SPE International Oilfield Corrosion Conference and Exhibition*, Aberdeen, Scotland **2018**, 1.
[4] Y. Makino, T. Okamoto, Y. Goto, M. Araki, *Offshore Technology Conference*, Houston, TX **1988**, 537.
[5] 4subsea/PSA-Norway Report no. 0389-26583-U-0032, *Unbonded Flexible Risers – Recent Field Experience and Actions for Increased Robustness*, 4Subsea AS, Nesbru, Norway **2013**.
[6] M. J. Al-Maslamani, *Offshore Technology Conference*, Houston, Texas **1996**, 213.
[7] D. Pipa, S. Morikawa, G. Pires, C. Camerini, J. M. Santos, *EURASIP J. Adv. Signal Process.* **2010**, *2010*, 176203.
[8] NACE/ASTM G193-20a NACE International, Houston, TX/ASTM International, West Conshohocken, PA **2020**.
[9] S. Lynch, *Corros. Rev.* **2012**, *30*, 105.
[10] P. Kedzierzawski, in *Hydrogen Degradation of Ferrous Alloys*, 4th ed. (Eds: R. A. Oriani, J. P. Hirth, M. Smialowski), William Andrew Publishing/Noyes **1985**, p.271.
[11] K. O. Findley, M. K. O'Brien, H. Nako, *Mater. Sci. Technol.* **2015**, *31*, 1673.
[12] A. Turnbull, *Int. J. Hydrogen Energy* **2015**, *40*, 16961.
[13] D. Johnson, G. Krauss, *Metall. Trans. A* **1987**, *18A*, 717.
[14] H. Husby, M. Iannuzzi, R. Johnsen, M. Kappes, A. Barnoush, *Int. J. Hydrogen Energy* **2018**, *43*, 3845.
[15] D. L. Johnson, J. K. Wu, *J. Mater. Energy Syst.* **1987**, *8*, 402.
[16] A. J. Kumnick, H. H. Johnson, *Metall. Mater. Trans. B* **1974**, *5*, 1199.
[17] M. Nagumo, K. Takai, N. Okuda, *J. Alloys Compd.* **1999**, *293–295*, 310.
[18] H. M. Ha, J.-H. Ai, J. R. Scully, *Corrosion* **2014**, *70*, 166.
[19] H.-J. Kim, H.-Y. Jung, T.-W. Kwon, Y.-D. Chung, *Mater. Trans.* **2019**, *60*, 1614.
[20] H. W. Jeng, L. H. Chiu, D. L. Johnson, J. K. Wu, *Metall. Mater. Trans. A* **1990**, *21A*, 3257.
[21] H. Izadi, M. Tavakoli, M. H. Moayed, *Mater. Chem. Phys.* **2018**, *220*, 360.
[22] API Specification 17J, *Specification for Unbonded* Flexible Pipe, American Petroleum Institute, Washington, DC **2014**.
[23] NACE Standard TM0198, NACE International, Houston, TX **2016**.
[24] M. A. V. Devanathan, Z. Stachurski, *Proc. R. Soc. London, Ser. A* **1962**, *270*, 90.
[25] ISO 17081, *Method of measurement of hydrogen permeation and determination of hydrogen uptake and transport in metals by an electrochemical technique*, International Organization for Standardization, Geneva, Switzerland **2014**.
[26] ASTM G148, Standard Practice for Evaluation of Hydrogen Uptake, Permeation, and Transport in Metals by an Electrochemical Technique, ASTM, West Conshohocken, PA **2018**.
[27] P. Bruzzoni, *Ph.D. Thesis*, Universidad de Buenos Aires, **2003**.
[28] P. C. Rivera, V. P. Ramunni, P. Bruzzoni, *Corros. Sci.* **2012**, *54*, 106.
[29] P. Bruzzoni, R. Garavaglia, *Corros. Sci.* **1992**, *33*, 1797.

[30] P. Manolatos, M. Jerome, J. Galland, *Electrochim. Acta* **1995**, *40*, 867.
[31] A. J. Haq, K. Muzaka, D. P. Dunne, A. Calka, E. V. Pereloma, *Int. J. Hydrogen Energy* **2013**, *38*, 2544.
[32] G. M. Pressouyre, *Metall. Mater. Trans. A* **1983**, *14*, 2189.
[33] W. C. Luu, J. K. Wu, *Corros. Sci.* **1996**, *38*, 239.
[34] A. Turnbull, R. B. Hutchings, *Mater. Sci. Eng., A* **1994**, *177*, 161.
[35] K. Kiuchi, R. B. McLellan, *Acta Metall.* **1983**, *31*, 961.
[36] S. Frappart, X. Feaugas, J. Creus, F. Thebault, L. Delattre, H. Marchebois, *J. Phys. Chem. Solids* **2010**, *71*, 1467.
[37] T. Zakroczymski, *J. Electroanal. Chem.* **1999**, *475*, 82.
[38] C. Forot, E. Legrand, E. Roguet, J. Creus, J. Kittel, X. Feaugas, *Eurocorr 2015*, Graz, Austria **2015**, p.107.
[39] T. Zakroczymski, *Scr. Metall.* **1985**, *19*, 521.
[40] T. Zakroczymski, Z. Szklarska-Smialowska, *J. Electrochem. Soc.* **1985**, *132*, 2548.
[41] E. Owczarek, T. Zakroczymski, *Acta Mater.* **2000**, *48*, 3059.
[42] T. Zakroczymski, E. Owczarek, *Acta Mater.* **2002**, *50*, 2701.
[43] A. Turk, S. Pu, D. Bombač, P. E. J. Rivera-Díaz-del-Castillo, E. I. Galindo-Nava, *Acta Mater.* **2020**, *197*, 253.
[44] V. Olden, C. Thaulow, R. Johnsen, *Mater. Des.* **2008**, *29*, 1934.
[45] D. P. H. Hasselman, L. F. Johnson, *J. Compos. Mater.* **1987**, *21*, 508.
[46] L. E. Nielsen, *Ind. Eng. Chem. Fundam.* **1974**, *13*, 17.
[47] L. Tau, S. L. I. Chan, *Mater. Lett.* **1996**, *29*, 143.
[48] J. McBreen, L. Nanis, W. Beck, *J. Electrochem. Soc.* **1966**, *113*, 1218.
[49] N. Boes, H. Züchner, *J. Less-Common Met.* **1976**, *49*, 223.
[50] J. P. Hirth, *Metall. Trans. A* **1980**, *11*, 861.
[51] A. H. Bott, D. S. Dos Santos, P. E. V. De Miranda, *J. Mater. Sci. Lett.* **1993**, *12*, 390.
[52] A. J. Kumnick, H. H. Johnson, *Acta Metall.* **1980**, *28*, 33.
[53] E. Riecke, *Werkst. Korros.* **1981**, *32*, 66.
[54] M. L. Hill, E. W. Johnson, *Trans. Metall. Soc. AIME* **1960**, *215*, 717.
[55] W. Dietzel, M. Pfuff, G. G. Juilfs, *Mater. Sci.* **2006**, *42*, 78.
[56] E. Van den Eeckhout, A. Laureys, Y. Van Ingelgem, K. Verbeken, *Mater. Sci. Technol.* **2017**, *33*, 1515.

How to cite this article: E. S. Skilbred, M. Kappes, M. Iannuzzi, R. Johnsen, *Mater. Corros.* **2021**, 1–20. https://doi.org/10.1002/maco.202112615

Paper II

E.S. Skilbred, S. Palencsár, A. Dugstad, R. Johnsen

Hydrogen uptake during active CO_2-H_2S corrosion of carbon steel wires in simulated annulus fluid

Corrosion Science (2022), 199, 1-13. DOI: 10.1016/j.corsci.2022.110172

Corrosion Science 199 (2022) 110172

Contents lists available at ScienceDirect

Corrosion Science

journal homepage: www.elsevier.com/locate/corsci

Hydrogen uptake during active CO_2-H_2S corrosion of carbon steel wires in simulated annulus fluid

Ellen Synnøve Skilbred [a,*], Simona Palencsár [b], Arne Dugstad [b], Roy Johnsen [a]

[a] Department of Mechanical and Industrial Engineering, Norwegian University of Science and Technology, 7034 Trondheim, Norway
[b] Institute for Energy Technology, P.O. Box 40, NO-2027, Kjeller, Norway

ARTICLE INFO

Keywords:
Carbon steel A
Hydrogen permeation B
SEM B
XRD B
Hydrogen absorption C

ABSTRACT

The hydrogen uptake of five carbon steel wires exposed to a corrosive CO_2/H_2S environment where protective film formation was not favorable was measured. The hydrogen uptakes decreased with the accumulation of retained carbide for most of the materials. It is assumed that hydrogen adsorbed on carbides at some distance from ferrite will not easily diffuse to the steel, hence giving the beneficial effect. This effect was not observed for the material with the lowest carbon content. Apart from this material, the hydrogen uptake increased with the carbon content, probably due to hydrogen trapping on ferrite-cementite interfaces.

1. Introduction

Flexible pipes have been used for oil and gas transportation since the 1970′s. They consist of several polymeric and metallic layers, such as carcass, inner liner, pressure armor wires, tensile armor wires and outer sheath. The annular space where the tensile steel armor wires are located is normally dry at start up but chemical species like CO_2, H_2S and H_2O can diffuse from the bore through the polymer layers into the annulus and create a corrosive environment. If the outer sheath is damaged, seawater may also enter the annulus. The free volume in the annulus is low compared to the area of the steel armor wires which gives rapid accumulation of dissolved corrosion products and a higher pH level than normally seen for CO_2 corrosion of carbon steel pipelines [1]. The liquid in the flexible pipe annulus is expected to become highly supersaturated with dissolved corrosion products and that will promote the formation of protective $FeCO_3$ and FeS films under normal operation. Corrosion rates below 0.01 mm y^{-1} are usually measured under such conditions [1–3]. However, upset conditions like air or seawater ingress, continuous high water condensation (backflow from vent tubes) and partial inhibition can reduce the supersaturation and prevent or weaken the protective films.

During pure CO_2 corrosion, the most likely cathodic reactions are [4,5].

$$2H^+ + 2\ e^- \rightarrow H_2 \quad (1)$$

$$2H_2CO_3 + 2\ e^- \rightarrow H_2 + 2HCO_3^- \quad (2)$$

The H^+ can be formed by water dissociation, but the rate of hydrogen evolution is enhanced by the presence of CO_2 due to the two dissociation steps of the carbonic acid [6]. When the concentrations of Fe^{2+} and CO_3^{2-} ions exceed their solubility limits they can form iron carbonate films. The dominant anodic reaction is the dissolution of iron in water and the overall reaction for CO_2 corrosion in steels is [5,7].

$$Fe + CO_2 + H_2O \rightarrow H_2 + FeCO_3 \quad (3)$$

$FeCO_3$ with good adhesion and coverage of the steel surface can retard the diffusion of species to and from the steel surface [8]. The adhesion of the $FeCO_3$ film is dependent on the presence of iron carbides, and the carbide size and distribution become important since the corrosion products are better adhering to the carbides than to the ferrite matrix [9].

Small amounts of H_2S can also diffuse into the annulus and give a mixed CO_2 and H_2S corrosion mechanism. The general equation for precipitation of ferrous sulfide can be written as [7].

$$Fe^{2+} + H_2S \rightarrow FeS + H_2 \quad (4)$$

The formation of hydrogen gas requires adsorption of H^+ on the metal or carbide surface. While adsorbed, H^+ is reduced to elemental H and may absorb into the metal and cause hydrogen embrittlement (HE). Hydrogen embrittlement is a failure mechanism that relies on the presence of elemental hydrogen and mechanical stress in a susceptible

* Corresponding author.
E-mail address: ellen.s.skilbred@ntnu.no (E.S. Skilbred).

https://doi.org/10.1016/j.corsci.2022.110172
Received 8 November 2021; Received in revised form 19 January 2022; Accepted 10 February 2022
Available online 12 February 2022

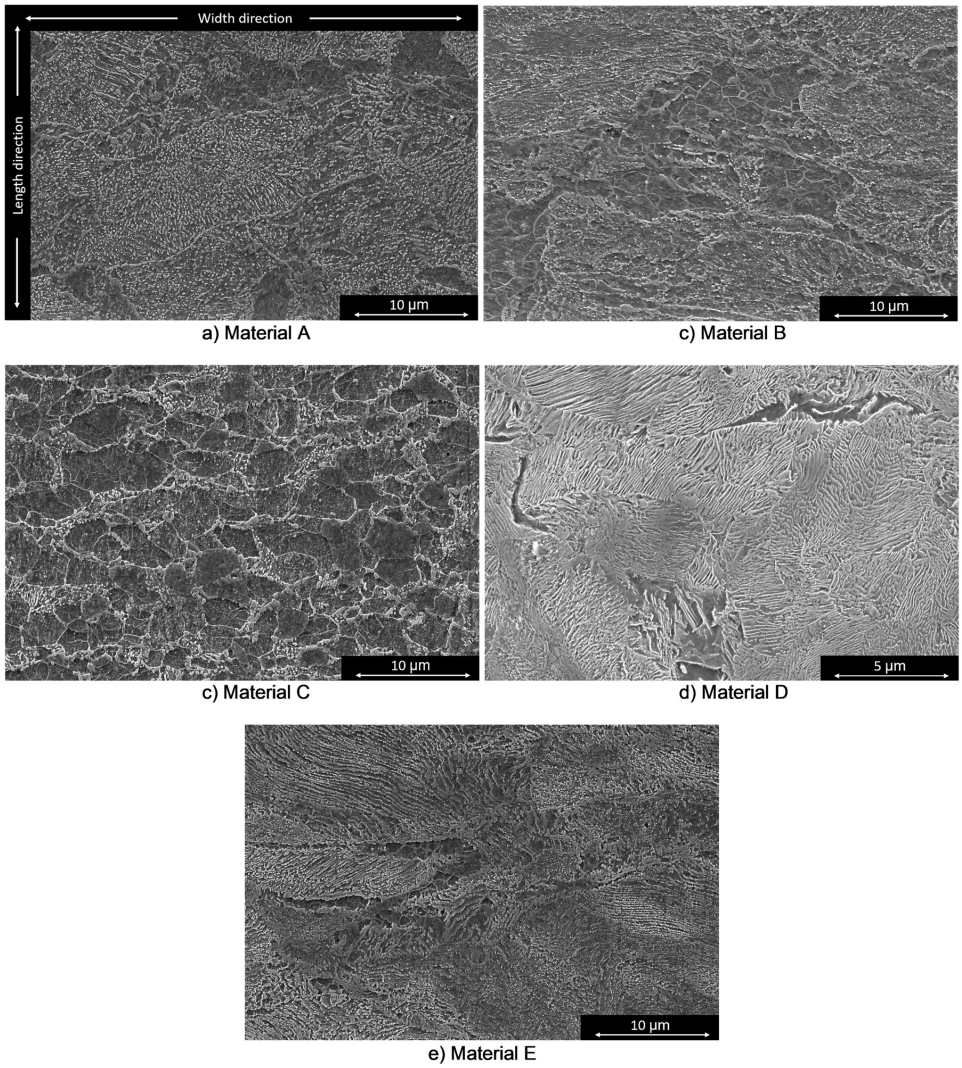

Fig. 1. SEM images in width-length plane for the materials included in the test program.

microstructure. Several theories have been proposed to explain the mechanism, including the internal pressure theory [10], hydride formation [11], hydrogen enhanced strain-induced vacancies [12], hydrogen enhanced localized plasticity [13,14], hydrogen enhanced decohesion [15] and the defactant theory [16]. The elemental hydrogen in the steel can exist in lattice and in microstructural sites with a higher affinity for hydrogen than the lattice. Voids, vacancies, interstitials, phase boundaries, grain boundaries, dislocations and some intermetallic particles like TiC and MnS are all microstructural features that can act as hydrogen traps in steels [17]. The hydrogen uptake in steels at open circuit potential (OCP) depends on both the steel microstructure, the environment, and the surface condition. The cathodic corrosion reactions and their reaction rates affect the quantity of hydrogen reacting on the surface, but the presence of hydrogen recombination poisons, for example the elements S, P and Pb, affect the rate of hydrogen recombination vs. hydrogen absorption [18]. The amount of absorbed hydrogen is also dependent on where the cathodic reaction is taking place. Pure CO_2 corrosion of steels can start with the selective dissolution of ferrite phase while the Fe_3C structure is retained [19–21]. The Fe_3C is conductive and is mainly a cathodic site during CO_2 corrosion, and as the Fe_3C surface area increases, the dissolution of ferrite accelerates [19,22]. The retained Fe_3C can form a thick porous layer, and if the pH and the concentration of dissolved iron are sufficiently high, iron carbonate can precipitate in the Fe_3C layer and significantly reduce the corrosion rate [19,20]. Silva et al. [21] conducted electrochemical hydrogen permeation tests on pre-corroded steel samples with Fe_3C or $FeCO_3$ rich layers. The sample with the $FeCO_3$ layer had twice as much hydrogen as a reference wet-ground sample without any surface layer, while the sample with a Fe_3C rich surface layer had five times more hydrogen than the wet-ground sample. The formation of a retained Fe_3C layer may also lead to an internal acidification in the layer which prevents later formation of $FeCO_3$ in contact with the metal [23]. Plennevaux et al. [24] measured the hydrogen uptake in a sour service pipe steel exposed to 0.1 mol L^{-1} potassium perchlorate ($KClO_4$) and various

Table 1
Cementite volume fractions (f) and chemical compositions of the wire materials. Elements that were not detected for a particular material are labeled with N.D.

Material	f [-]	C [wt%]	Si [wt%]	S [wt%]	P [wt%]	Mn [wt%]	Ni [wt%]	Cr [wt%]	Al [wt%]
A	0.077	0.501	0.247	0.002	0.003	0.604	0.001	0.011	0.031
B	0.043	0.282	0.223	0.010	0.006	0.733	0.010	0.003	0.035
C	0.054	0.353	0.194	0.007	0.009	0.678	0.013	0.003	0.042
D	0.127	0.830	0.331	0.005	0.005	0.683	0.005	0.002	0.041
E	0.095	0.618	0.225	0.002	0.007	0.729	0.009	0.032	0.037
Material	V [wt%]	Pb [wt%]	N [wt%]	Ti [wt%]	Sn [wt%]	Cu [wt%]	Co [wt%]	Mo [wt%]	B [wt%]
A	0.036	0.050	0.009	$< 10^{-4}$	N.D.	N.D.	N.D.	0.001	$< 10^{-4}$
B	0.001	0.065	0.020	0.002	N.D.	$< 10^{-4}$	$< 10^{-4}$	0.001	$< 10^{-4}$
C	0.002	0.065	0.219	0.002	$< 10^{-3}$	0.001	N.D.	0.001	$< 10^{-4}$
D	0.050	0.065	0.099	0.004	0.001	$< 10^{-4}$	N.D.	0.002	$< 10^{-3}$
E	0.001	0.050	0.014	$< 10^{-4}$	N.D.	N.D.	N.D.	$< 10^{-3}$	$< 10^{-4}$

partial pressures of N_2, CO_2 and H_2S while cathodically polarized. They found that the hydrogen uptake increased with the H_2S pressure and was higher for H_2S in CO_2 than H_2S in N_2. Wallaert et al. [25] measured the hydrogen content of two steels exposed to NACE test TM0284 solution A over four weeks by hot extraction. The concentration of diffusible hydrogen peaked within 5 days of exposure, then decreased to less than half of the peak value within 20 days. The corrosion currents increased with time and the decrease in hydrogen concentration was attributed to the formation of a double layer of FeS corrosion products where S^{2-} and HS^- were migrating to the steel surface to form the inner layer. Huang et al. [26] performed electrochemical permeation tests on pre-corroded steel samples in a solution containing H_2S. The results showed that crystalline FeS formed at low pH and low H_2S concentrations, while mackinawite formation was promoted with the increase of H_2S concentration (from 0.2 to 20 mM) and/or pH (from 3.5 to 5.5). The blocking effect of the surface film on hydrogen permeation increased with increasing H_2S concentration and reduced pH value. Zhou et al. [27] conducted several electrochemical hydrogen permeation tests for an X80 pipeline steel exposed to pure H_2S, pure CO_2 and several H_2S/CO_2 partial pressures to study the permeation behavior and effect of corrosion products on hydrogen permeation. They observed different hydrogen permeation behaviors and concluded that these were controlled by the mutual coupling of the hydrogen promoting effect of H_2S and CO_2, the corrosion products, and the hydrogen evolution during the corrosion reaction.

This work investigates the hydrogen uptake of carbon steels exposed under upset conditions not giving the high supersaturation of dissolved corrosion products required for protective film formation [28,29]. Five carbon steel tensile armor wires for flexible pipes with different microstructures were exposed to modified artificial seawater (ASTM D1141–90) bubbled with CO_2 and H_2S at OCP. The experiments were conducted with an electrochemical permeation cell similar to the design by Devanathan and Stachurski [30]. The wires were first exposed to 0.2 bar CO_2 and 1 bar CO_2, before H_2S was added and the partial pressure of H_2S was varied in steps. This gave several hydrogen permeation transients that showed how the changes in surface condition affect the hydrogen uptake. The electrolyte was continuously replaced to maintain a low concentration of dissolved iron in the electrolyte. The corrosion products on the sample surface were characterized by scanning electron microscopy (SEM), x-ray diffraction (XRD) and energy-dispersive spectroscopy (EDS), and the samples were stripped to measure the weight of corrosion products attached to the surfaces. To provide more insight in the interplay between steel microstructure, hydrogen uptake, corrosion rates and corrosion products, the results are compared with the hydrogen uptakes measured during cathodic polarization in previous work [31]. In [31], the hydrogen uptake of the same wire materials was investigated with hydrogen introduced by cathodic polarization to -12 mA cm^{-2} in deaerated 0.1 M NaOH at 25 °C.

2. Experimental

2.1. Materials

Five different tensile armor wire steels were tested. The wires were identified by letters A to E. The wire materials were qualified according to API 17 J Specification for Unbonded Flexible pipe [32], but are designed for different operating conditions. Not all the wires were qualified for exposure to H_2S (referred as sour service). The wires were 3 mm thick with widths from 9 to 12 mm and were taken from coil. Fig. 1 shows SEM images of the materials in the width-length plane. The microstructures of the materials consist of ferrite and pearlite. The cementite volume fraction, f, was estimated with the lever rule, assuming all C is located in cementite. The chemical compositions and f are given in Table 1. A description of the degree of plastic deformation, grain size, cementite morphologies and mechanical properties are given in Table 2. The microstructures of the materials are complex, and the positions of the grain boundaries are not always easy to find. The grain size is therefore described by the largest well-defined grains observed rather than the average grain size, and the grains of ferrite and cementite were evaluated separately. The yield strength (YS), ultimate tensile

Table 2
Mechanical and microstructural properties of the wire materials.

Material	Extent of plastic deformation			Cementite morphology		
A	Some deformation.			Globular, partly lamellar		
B	Pearlite deformed. Some banding of ferrite.			Globular		
C	Some banding and deformation.			Globular		
D	Highly deformed grains.			Lamellar		
E	Pearlite deformed. Some banding of ferrite.			Globular, partly lamellar		
Material	Estimated grain size[a]		Hardness [HV_{10}]	YS [MPa]	UTS [MPa]	Ep [-]
	Ferrite [μm]	Cementite [μm]				
A	≤ 14	≤ 36	331 ± 14	871	1009	0.115
B	≤ 10	≤ 28	290 ± 10	805	847	0.157
C	≤ 20	≤ 14	257 ± 4	616	744	0.152
D	≤ 7	≤ 24	453 ± 16	1408	1622	0.094
E	≤ 3	≤ 22	386 ± 8	1097	1260	0.108

[a] Max grain size.

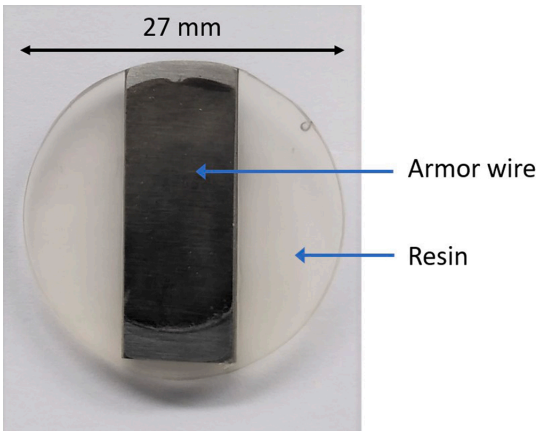

Fig. 2. Embedded sample for electrochemical hydrogen permeation experiments.

strength (UTS) and plastic strain-to-failure (Ep) were measured with tensile Slow Strain Rate Tests (SSRT) using a strain rate of 10^{-6} s^{-1}. The plastic strain-to-failure was determined in agreement with NACE Standard TM0198–2016 [33]. Hardness was measured in the cross-sections of the samples with a ZwickRoell ZHV30 Vickers hardness tester using condition HV10.

2.2. Sample preparation

The wires were coiled, and the most bent wires were straightened with a roller straightener before cutting. The wires were cut in ~2.8 cm long pieces, which were ground with SiC paper on both sides until flat, washed in acetone and sonicated in ethanol. The corners of the wire pieces were also ground so the wire pieces could fit a mounting cup with 3 cm diameter. The pieces were then embedded in a light-curing resin (Technovit® LC 2000, mixed with the additive "Inside Cure") to form a disc-shaped sample, see Fig. 2. When installed in the permeation cell, the exposed area is 1.72 cm^2 for the samples made with the narrowest wire materials and 2.26 cm^2 for the samples with the widest wire materials. Ideally, the permeation test samples should have a circular exposed area which fulfills minimum 10:1 radius-to-thickness ratio, to guarantee one-dimensional diffusion through the thickness [34,35]. However, other sample configurations are accepted if there are limitations in material form [34]. After mounting, the two sides were ground with European grit P1200 SiC paper and the sample heated in a heating cabinet overnight at 120 °C. Sites with weak adhesion between the steel and polymer were visible after heating and only the defect-free samples were tested. To ensure fast oxidation of hydrogen on the detection side of the sample, this side was coated with Pd. The coating was applied by electrodeposition with the procedure proposed by Bruzzoni [36] and further developed by Husby et al. [37]. After Pd-coating, the samples were heated to 120 °C in a heating cabinet for minimum 16 h to remove any hydrogen absorbed during the Pd-coating process. The sample surface without Pd-coating was ground with European grit P1000 SiC paper, rinsed in isopropanol and dried in air stream within an hour before the start of the electrochemical hydrogen permeation experiments. The final sample thicknesses ranged from 2.64 to 2.92 mm.

2.3. Chemicals and gases

The permeation cell consists of two compartments: one where the corrosive environment is created, and one where the hydrogen that permeates through the sample is detected. The corrosion compartment was filled with modified ASTM D1141–90 electrolyte. The electrolyte was prepared with analysis grade salts and distilled water, but without $CaCl_2$, NaF and KBr. The electrolyte in the detection compartment was 0.1 M NaOH which was made with analysis grade NaOH. CO_2 and N_2 gas with 99.999% purity were used. The H_2S gas was mixed in house from 99.999% purity CO_2 and 99.8% purity H_2S and the concentration was determined by gas chromatography. The gases were mixed to the desired composition using mass flow controllers. The gas flow into the corrosion compartment was ca. 600 mL h^{-1}.

2.4. Procedure

The steel sample was placed in the sample holder and clamped with gaskets between two glass cells, as shown in Fig. 3. A screw in the sample holder ensured electrical contact between the sample and the potentiostats used for corrosion measurements and hydrogen detection. The tests were conducted at ambient pressure and the temperature was kept at 25 °C by circulation of water through the double walls of the permeation cell. The tests started with stabilization of the detection side of the sample for ~72 h. The detection compartment contained 0.1 M NaOH bubbled with N_2 and polarized to + 540 mV vs. the normal hydrogen electrode (NHE). The corrosion chamber was fed with N_2 gas

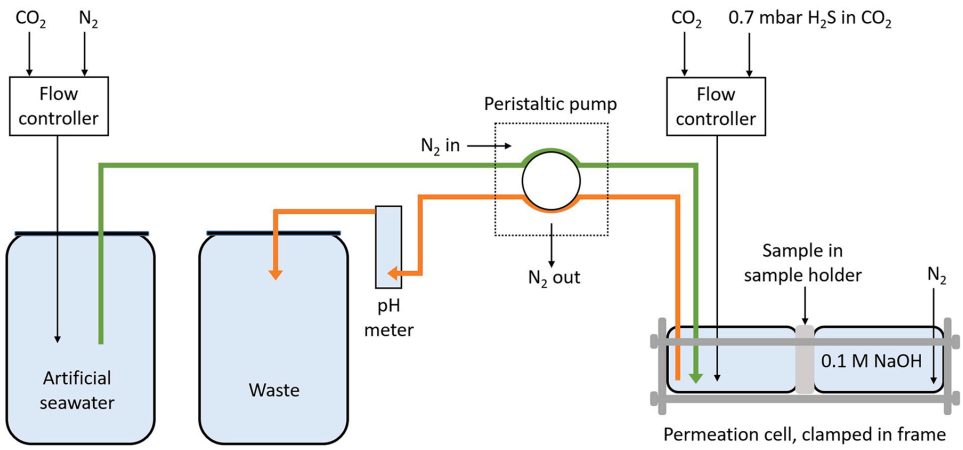

Fig. 3. Schematic of the test setup.

Table 3
Conditions in the corrosion compartment.

Step	0	1	2	3	4	5	6	7	8
Duration [h]	~ 72	~ 48	~ 48	~ 48	~ 48	~ 72	~ 24[a]	~ 24	~ 24[b]
Electrolyte	–	Yes	Yes	Yes	Yes	Yes	Yes	Yes	Yes
p_{N2} [bar]	1	0.8	–	–	–	–	–	–	–
p_{CO2} [bar]	–	0.2	1	1	1	1	1	1	1
p_{H2S} [mbar]	–	–	–	0.1	0.2	0.4	0.7	0.2	0.1

[a] For Material D, step 6 was lengthened by a day to compensate for a period of clogged liquid and gas supply in step 5.
[b] For Material A, step 8 lasted 2 days due to scheduling issues.

during the stabilization of the detection side of the sample. After ~72 h of stabilization, the electrolyte bubbled with 0.2 bar CO_2 and 0.8 bar N_2 was added to the corrosion compartment. The solution was continuously refreshed by pumping electrolyte from a feeding unit and pumping out used solution to a waste container. The flow rate of electrolyte was 25–35 mL h^{-1}. After ~48 h, the CO_2 pressure was increased to 1 bar CO_2 and kept for ~48 h before 0.1 mbar H_2S was added to the gas stream. The CO_2 pressure during the H_2S exposure was 1 bar, and the H_2S partial pressure was first increased stepwise from 0.1 mbar to 0.7 mbar, then decreased to 0.1 mbar. The gas composition in the corrosion compartment is shown in Table 3. The gas pressures were adjusted without stopping the flow of gas into the corrosion compartment. The pH was measured in the electrolyte that was pumped out of the corrosion compartment and the waste electrolyte was collected for measuring the concentration of Fe^{2+} in the solution. A controlled amount of 1 M HCl (ca. 13% of the expected waste volume) was added to the waste containers before the waste collection started to prevent oxidation and precipitation of the dissolved iron. Aliquots of the collected waste were added to a developer solution and the dissolved iron content was determined by spectrophotometric analysis. Linear polarization resistance (LPR) was measured to estimate the corrosion rate. In addition, OCP was measured.

2.5. Electrochemical measurements

The polarization of the detection side of the sample was conducted in a 3-electrode set-up with the sample as working electrode, a platinum wire as counter electrode, and a mercury-mercurous electrode (MME), $Hg/HgSO_4/SO_4^{2-}$ sat. K_2SO_4, as reference. The MME electrode has a potential of + 650 mV vs. NHE. Two Interface 1010E potentiostats (Gamry Instruments®) were used for the experiments: One for polarization of the detection side and one for running linear polarization resistance (LPR) measurements and electrochemical impedance spectroscopy (EIS) on the corrosion side of the sample. The LPR and EIS measurements were performed in a 3-electrode set-up with the sample as working electrode, a platinum wire as counter electrode, and Ag/AgCl (3 M KCl) as reference electrode. The LPR scans were conducted every 30 min at 0.1 mV s^{-1}, from − 5 to + 5 mV relative to the open circuit potential (OCP). The corrosion current density was calculated with the Stern-Geary equation:

$$i_{corr} = \frac{B}{RpA} \tag{5}$$

where A is the sample area exposed in the corrosion compartment, B is the Stern-Geary constant which was set to 20 mV (the value was empirically chosen based on previous experience and tests conducted in a similar environment), and Rp is the polarization resistance, defined by the ratio between the variation in potential (E) and current (I):

$$R_p = \frac{\Delta E}{\Delta I} \tag{6}$$

The polarization measurements were corrected for the solution resistance (R_s) which was determined by EIS. The frequency range was 0.01–10000 Hz, the AC voltage was 10 mV vs. OCP and 6 points per decade were recorded.

2.6. Surface analysis / postmortem analysis of samples

After the permeation test, the samples were retrieved from the permeation cell, cleaned in isopropanol and dried in air stream. The samples were examined by SEM and the chemical composition of the corrosion products was determined by EDS and XRD. A carbon tape was then lightly attached to the surfaces and removed in order to analyze the corrosion products that remained on the surface. The samples were weighed after the test, after attachment of carbon tape and after stripping to estimate the weight of corrosion products attached to the surface, i.e. the film weight. The stripping of corrosion products was done by exposing only the corroded side of the sample to modified Clarke's solution for ca. 1 min, then quickly rinsing with distilled water, isopropanol and drying in air stream.

2.7. Calculation of hydrogen uptake

During steady-state permeation, it is assumed that the hydrogen traps are occupied and that the reversibly trapped hydrogen is in equilibrium with the lattice hydrogen. Cementite is considered to be both an obstacle for hydrogen diffusion and a contributor to increased hydrogen uptake by trapping on the ferrite-cementite interfaces [38–40]. The diffusion of hydrogen inside the cementite phase can therefore be neglected, which means the diffusion of hydrogen in lattice during steady state is determined mainly by the theoretical diffusion coefficient of ferrite, D_l. Considering an even amount of hydrogen over the subsurface of the hydrogen entry side, the steady-state flux of hydrogen, J_{SS}, will be

$$J_{SS} = \frac{D_l C_0^{av}}{L} \tag{7}$$

where L is the length of the diffusion path and C_0^{av} is the average lattice hydrogen concentration on the subsurface of the hydrogen entry side. In the temperature range − 40–80 °C, D_l is given by [41].

$$D_l = 7.23 \times 10^{-8} \exp\left(-\frac{Q}{RT}\right) \text{ m}^2\text{s}^{-1} \tag{8}$$

where $Q = 5.69$ kJ mol^{-1} and R is the gas constant 8.314 J K^{-1} mol^{-1}. This gives $D_l = 7.28 \times 10^{-5}$ cm^2 s^{-1} at 25 °C. When any obstacles to hydrogen diffusion have negligible effect on the diffusion path, L is equal to the sample thickness. In our previous work [31], a tortuosity factor, τ, was estimated for the five materials. This factor was defined as the true length of the diffusion path divided by the sample thickness, as suggested by Forot et al. [42]. Since the hydrogen is expected to exist in traps and ferrite lattice, with a negligible amount of hydrogen inside the cementite phase, the subsurface hydrogen concentration can be adjusted to take the fraction of cementite, f, into account [43].

$$C_0^{fe} = \frac{C_0^{av}}{1-f} \tag{9}$$

To calculate the concentration of diffusible hydrogen, i.e. hydrogen in lattice and reversible sites, C_{0R}, Eq. (7) can be reformulated with the effective diffusion coefficient of hydrogen, D_{eff} [35].

$$C_{0R} = \frac{J_{SS} L}{D_{eff}} \tag{10}$$

During corrosion, the boundary conditions on the hydrogen entry side are changing over time, making the estimation of D_{eff} challenging. The hydrogen uptakes are therefore estimated using the effective diffusion coefficients determined in previous work [31] from the decay transients measured after 72 h of galvanostatic charging to

Table 4
Effective diffusion coefficients and tortuosity factors determined in previous work [31]. The tortuosity factors are given with their standard deviations.

Material	D_{eff} [cm^2 s^{-1}]	τ [-]
A	1.19×10^{-6}	1.122 ± 0.036
B	7.55×10^{-7}	1.055 ± 0.010
C	1.81×10^{-6}	1.056 ± 0.022
D	6.62×10^{-7}	1.669 ± 0.266
E	9.73×10^{-7}	1.158 ± 0.015

-12 mA cm^{-2} in 0.1 M NaOH. The effective diffusion coefficients and the tortuosity factors are given in Table 4. The estimated tortuosity factors were taken into account when calculating the effective diffusion coefficients and the difference between D_{eff} and D_l should therefore only reflect the reduction of diffusivity due to trapping of hydrogen.

The changing boundary conditions can also prevent a steady state to be reached during the tests. The equations for calculation of hydrogen uptake, (7), (9) and (10) are valid at steady state, but sometimes the permeation flux is increasing or decreasing with time instead of staying steady. In these cases, the steady state permeation flux may be replaced with a peak permeation flux [44] or the permeation flux after a certain exposure period [37].

3. Results

3.1. Corrosion parameters measured on the hydrogen entry side

3.1.1. Analysis of corroded surfaces

The XRD analyses showed peaks for Fe_3C for all materials, but iron carbonate and sulfides were not detected, see Fig. 4. Retained carbides were not easily identified in the first examination of the corroded surfaces in SEM, but after removal of the loose corrosion products by attaching and removing a carbon tape, it was evident that retained carbides were present on all the surfaces, see Fig. 5. Fe, C and O were the main elements detected by EDS in the corrosion products. Table 5 shows the film weight and the EDS analyses on the corroded surfaces after the loose corrosion products were removed with a carbon tape. The S content in the corrosion products was lowest for materials A and C, 0.4 at%. The highest S content was found for material D, 1.0 at%. The materials' rank of film weight from lowest to highest follows the rank in carbon content, B < C < A < E < D. Material B was tested twice, and the two tests are denoted B1 and B2. B1 was conducted with a sample that had been previously used in a permeation experiment whereas B2 was conducted with a fresh sample like in the other tests. For Material B, Fig. 5 shows the sample from test B2, but the sample from test B1 displayed the same characteristics.

3.2. pH and content of dissolved iron

The dissolved iron content in the collected waste and the pH measured continuously in the electrolyte pumped out of the corrosion compartment are shown in Table 6. The iron content was highest during step 2, where the sample was exposed to 1 bar CO_2. This coincides with the time of highest corrosion rate, see Fig. 6. The pH was highest during exposure to 0.2 bar CO_2 and was relatively stable during the steps with 1 bar CO_2 and varying partial pressure of H_2S.

3.2.1. Corrosion rates and OCP

The corrosion rates measured by LPR during step 1–8 of the permeation tests are given in Fig. 6. A clogging incident of the tubes supplying both liquid and gas to the corrosion compartment occurred during the test for Material D about 200 h after the electrolyte was added to in the corrosion compartment (step 5). The bubbling in the compartment stopped completely and this resulted in increased corrosion rate and decreased hydrogen permeation flux, probably due to a reducing concentration of H_2S in the cell with time. This issue was fixed around 250 h of exposure and the pH reached a similar level as before the incident. Step 6 (see Table 3) was extended by ~24 h in this test to allow a steady-state permeation flux to be reached.

In step 1, the 0.2 bar CO_2 exposure period, the corrosion rates were about 0.7 mm y^{-1} or lower, and relatively stable. The difference in corrosion rate during this step was sometimes larger for the two samples of Material B than it was for two samples of different materials. The same holds for the OCP measurements during this step, see Fig. 7. During the 1 bar CO_2 exposure, the corrosion rates increased to over 1 mm y^{-1} during all the tests except B2. For materials A, C, D and E, the corrosion rates increased with time during this step of the permeation test, but for Material B the corrosion rate was relatively stable or slightly decreasing. The corrosion rates of the lamellar material, D, increased more rapidly than the corrosion rates of materials A, C and E. The OCP level was also increasing for all the materials during the 1 bar CO_2 step of the permeation test.

H_2S exposure started ~96 h after the electrolyte was added in the corrosion compartment, and the corrosion rates decreased immediately. The increased corrosion rate for Material D during the 0.4 mbar H_2S step of the test was related to the clogging of the tubes for supplying gas and electrolyte directly into the corrosion compartment.

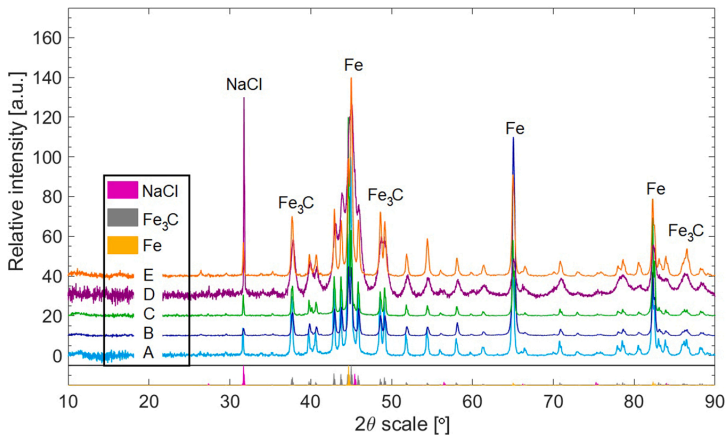

Fig. 4. Relative intensity of XRD signals from the corroded surfaces of the tested samples.

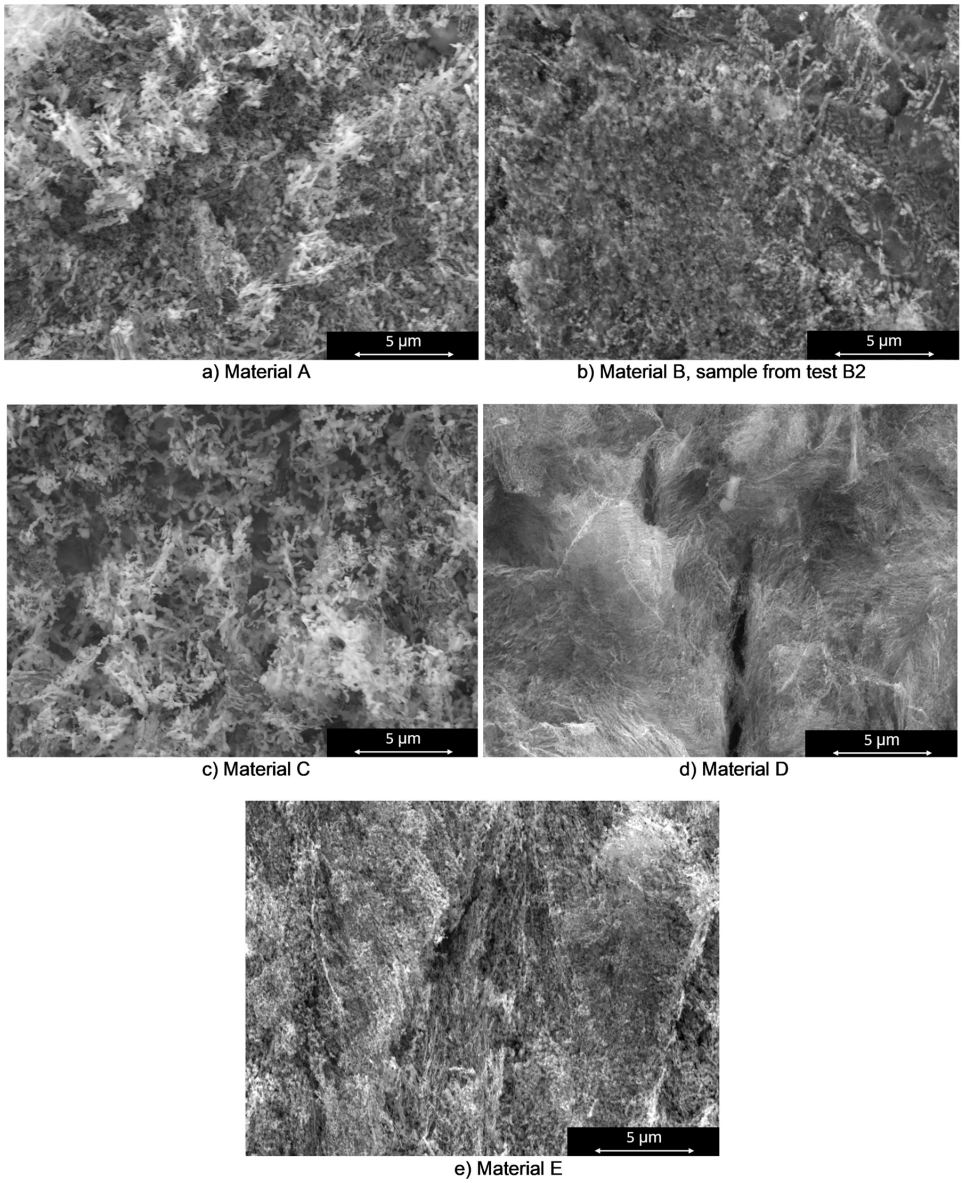

Fig. 5. Surface exposed after removal of corrosion products with carbon tape.

Table 5
EDS analyses on the corroded surfaces after removal of loose corrosion products with carbon tape and film weight measured by stripping the samples.

Material	C [at%]	O [at%]	S [at%]	Fe [at%]	Other [at%]	Film weight [mg cm^{-2}]
A	35.0 ± 9.2	9.6 ± 1.7	0.4 ± 0.1	52.2 ± 10.7	2.8	2.65
B (test B2)	27.6 ± 5.1	24.9 ± 7.2	0.8 ± 0.1	42.9 ± 7.7	3.7	0.84
C	35.3 ± 11.1	7.6 ± 3.3	0.4 ± 0.1	54.0 ± 14.2	2.7	2.27
D	33.7 ± 3.6	19.5 ± 2.5	1.0 ± 0.1	44.5 ± 5.0	1.3	4.18
E	32.5 ± 3.6	15.3 ± 1.7	0.7 ± 0.1	49.9 ± 4.0	1.6	2.74

Table 6
Dissolved iron content and pH measured in the electrolyte disposed from the corrosion compartment.

Step	1	2	3	4	5	6	7	8
pH [-]	5.6–5.9	4.9–5.2	4.9–5.2	4.9–5.2	4.9–5.2[a]	4.9–5.2	4.9–5.2	4.9–5.2
Fe^{2+} [ppm]	1.1–2.4	2.7–9.5	1.8–8.9	1.4–3.4	1.5–3.6	1.5–3.8	1.5–3.1	1.3–3.3

[a] Material D had a period of clogged liquid and gas supply in step 5 which interfered with the pH measurements during this step. The pH measurements of Material D during step 5 are therefore not included.

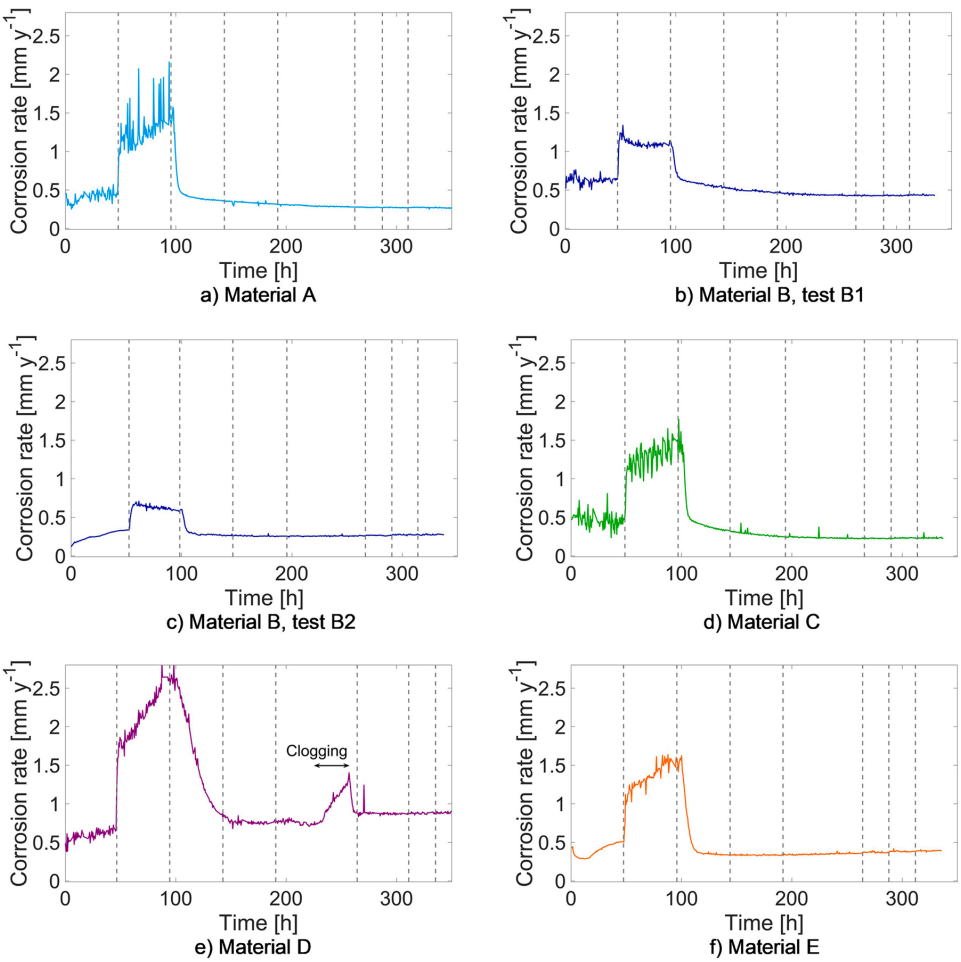

Fig. 6. LPR corrosion rates vs. time after the electrolyte was added in the corrosion compartment. The dashed lines mark the steps with different p_{CO2} and p_{H2S}, as described in Table 3.

3.3. Hydrogen permeation and uptake

The permeation current measured on the detection side of the sample while the corrosion side was exposed to the test solution is given for each material in Fig. 8. Materials A, C, D and E had a lower permeation current the second time the H_2S pressure was set to 0.1 mbar and 0.2 mbar, compared to the first time. In contrast, both tests for Material B had a higher hydrogen uptake the second time the corrosion compartment was supplied with 0.1 mbar and 0.2 mbar H_2S. When the hydrogen permeation flux increased in response to a change in CO_2 or H_2S pressure, the current increased until it reached a plateau or a peak. The time until a peak or plateau is reached depends on the real diffusion length, which is longer for materials with a high tortuosity factor. Material D has lamellar carbides and a high tortuosity factor and did not reach a plateau or peak for all the steps in the test. The plateaus and peaks were typically reached towards the end of the steps for this material if a plateau or peak was reached at all. For steps 1–6, the hydrogen uptakes were estimated for each step where a plateau or peak permeation current was reached in the test, using the permeation flux measured in the last hour of the step. For steps 7 and 8, the hydrogen uptakes were estimated from the plateau currents for the tests where a plateau was observed for these steps.

The hydrogen uptakes of the materials are shown in Figs. 9 and 10.

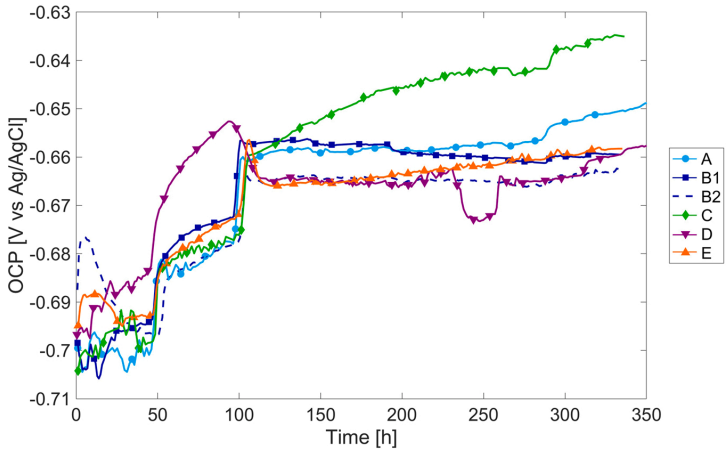

Fig. 7. OCP on the corrosion side of the sample vs. time after the electrolyte was added in the corrosion compartment.

An extra test for Material E, denoted E2, is included in the evaluation of hydrogen uptake during pure CO_2 corrosion. This test followed steps 0, 1 and 2 of the test program in Table 3, but an error occurred in the H_2S part, and those results are therefore not included. The deviation of hydrogen uptake for the two tests of Material B was 18% and 19% for the pure CO_2 steps and below 4% for the steps in H_2S environment.

During pure CO_2 corrosion, the hydrogen uptake could not be measured for the lamellar material, D. The high tortuosity of lamellar materials leads to both a lower permeation current, and a longer time-lag between a change in subsurface hydrogen concentration and corresponding change in permeation current on the hydrogen detection side. This explains the absence of a clear increase in permeation current during the CO_2 exposure for Material D. Material B had the highest C_{0R} measured during pure CO_2 corrosion (step 1 and 2 in Table 3), more than twice as high as the hydrogen uptakes of materials A, C and E. The hydrogen concentration in ferrite lattice was also higher for Material B than the other materials with globular Fe_3C. The repetition of hydrogen permeation tests for materials B and E show that the method was not accurate enough to measure the difference in hydrogen uptakes for materials A, C and E during pure CO_2 corrosion with confidence.

The hydrogen uptake in reversible traps during the H_2S exposure was highest for Material D and lowest for Material C, see Fig. 10. Materials A, E and B had the second, third and fourth lowest C_{0R} respectively. For the two last steps of the H_2S exposure, the materials had the same rank in C_0^{fe} and C_{0R}, but the hydrogen uptake was only measured for the materials with globular Fe_3C in these steps since a plateau current was not reached for the lamellar material, D.

The hydrogen uptakes measured for the same materials under exposure to 0.1 M NaOH and cathodic polarization to $-$ 12 mA cm^{-2} at 25 °C in previous work [31] are shown in Table 7. The hydrogen uptakes in Table 7 were estimated with the diffusion coefficients and tortuosity factors in Table 4. All the materials had lower hydrogen uptakes when exposed to modified artificial seawater with CO_2 and H_2S than during cathodic polarization in 0.1 M NaOH, but the difference is more significant for some materials than others.

4. Discussion

4.1. Corrosion products

The XRD results and images of the corroded surfaces in Fig. 5 show that all the surfaces have retained carbides which are exposed when iron is preferentially dissolved from the ferrite phase. $FeCO_3$ was not detected by the XRD, and the oxygen detected by EDS is therefore expected to originate mainly from oxides present on the surface before the electrolyte was added or oxygen that has reacted with the surface after the test. The selective dissolution of ferrite phase during pure CO_2 corrosion of steels is associated with an increase in corrosion rate and OCP with time due to the increasing surface area of retained Fe_3C [20,21]. This was seen for all the materials at 1 bar CO_2 exposure (step 2), except for Material B which had a relatively stable or declining corrosion rate. The surface of Material B may therefore have entered a more stable condition than the other materials at this stage. The carbides in Material B have a fine distribution and the carbide fraction is smaller than the carbide fraction of the other materials. Possibly, the amount of retained Fe_3C on the surface of Material B reached an equilibrium where the outer parts of the Fe_3C network were losing their electrical contact to the steel at the same rate as new Fe_3C was being exposed on the surface. The most rapidly increasing corrosion rates were found for the lamellar Material D, which has better foundation for increasing the Fe_3C surface area due to the continuous nature of the lamellar phase.

Small amounts of S (0.4–1.0 at%) were detected on all the corroded surfaces by EDS, but crystalline species containing S were not detected by XRD. In aqueous solutions containing H_2S, mackinawite is the major constituent of precipitated FeS. Mackinawite can precipitate as nano-sized platelets which are difficult to detect with classical XRD, since this technique relies on many repetitions of a periodic lattice. This has led to wrongful characterization of mackinawite as amorphous FeS [45]. The S detected on the corroded surfaces is therefore expected to be in the form of mackinawite, despite the lack of mackinawite XRD signal. For low H_2S concentrations ($\leq$ 340 ppm) in aqueous CO_2 environment, mackinawite has been observed to reduce the corrosion rate [46], and this was also observed in our experiments. The reduced corrosion rates in [46] were attributed to mackinawite acting as a charge-transfer barrier rather than a mass-transfer barrier.

4.2. Hydrogen uptake during pure CO_2 corrosion

During pure CO_2 corrosion, the C_{0R} of Material B was more than twice as high as the C_{0R} of Material A, C and E, and the C_0^{fe} was also significantly higher for Material B. The hydrogen uptake in Material D during pure CO_2 corrosion could not be determined and is therefore not discussed. When cathodically polarized in 0.1 M NaOH, the hydrogen uptake for materials B and E were twice as high as the hydrogen uptakes of materials A and C. The difference in hydrogen uptake under cathodic polarization and in CO_2 environment indicates that the hydrogen uptake

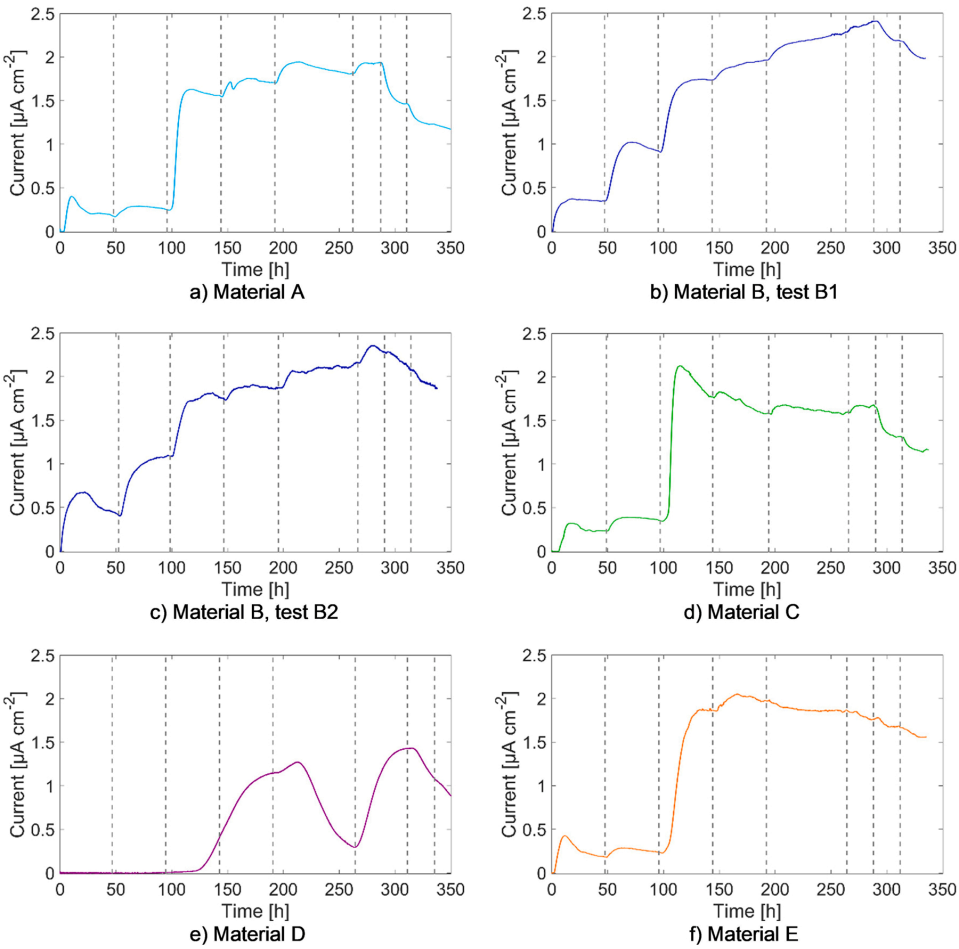

Fig. 8. Permeation current from the electrochemical hydrogen permeation tests. The dashed lines mark the steps with different p_{CO2} and p_{H2S}, as described in Table 3. The H_2S partial pressure was kept at 0.7 mbar H_2S about one day longer for Material D since the clogging of the gas supply to the corrosion compartment decreased the permeation current.

during CO_2 corrosion is strongly influenced by the corrosion mechanism. The corrosion rates and measured hydrogen uptakes increased when the CO_2 partial pressure was increased from 0.2 to 1 bar, but the permeation flux decreased after reaching a peak for all the transients observed in CO_2 environment, except the 1 bar CO_2 transient for Material B test 2 which reached a plateau. This indicates that the corroded surfaces created a barrier for hydrogen permeation under these conditions. The main change on the surfaces during CO_2 corrosion was the accumulation of retained carbides, which happened to a greater extent for the materials with low hydrogen uptakes, A, C and E, than for the material with the highest hydrogen uptake, Material B. Materials B and C have the lowest carbon contents, 0.28 and 0.35 wt% respectively, but very different hydrogen uptakes. There is a substantial difference in film weight between these materials, which cannot be explained by the difference in corrosion rate and carbon content but may be related to the carbide distribution in the metal. Material C has a microstructure with thin carbides on many of the ferrite grain boundaries, which may give a stronger adhesion between the corrosion products and steel, and thus more retained carbides and higher film weight. Overall, it appears that the presence of retained carbides reduced the hydrogen uptakes of the wire materials. The retained carbide is conductive and can therefore not limit the hydrogen uptake as a charge-transfer barrier, but possibly as a mass-transfer barrier. The increased corrosion rate of ferritic-pearlitic steels during selective dissolution of ferrite is explained by a larger active cathodic area, which means that the average distance between cathodic reaction sites and ferrite increases as well. Since cementite is considered an obstacle to hydrogen diffusion [39,40,47], the hydrogen that is adsorbed on cementite far from ferrite will have less opportunities for absorption and diffusion into the uncorroded steel compared to hydrogen adsorbed close to the ferrite. Possibly, it is only hydrogen that is reduced on ferrite or on carbides near ferrite that has a chance of being absorbed in the steel. If the retained carbide area is increasing faster than the corrosion rate, the cathodic current density will decrease, and less hydrogen will be reduced near ferrite. This is a possible mechanism for the presence of a peak hydrogen permeation flux during pure CO_2 corrosion. The proposed mechanism relies on a lower concentration of adsorbed hydrogen on and near the ferrite. The retained carbides are increasing the corrosion rate and hence the total amount of hydrogen reacting on the surface. If this effect dominates, the hydrogen uptake will increase with the amount of retained carbides rather than decrease,

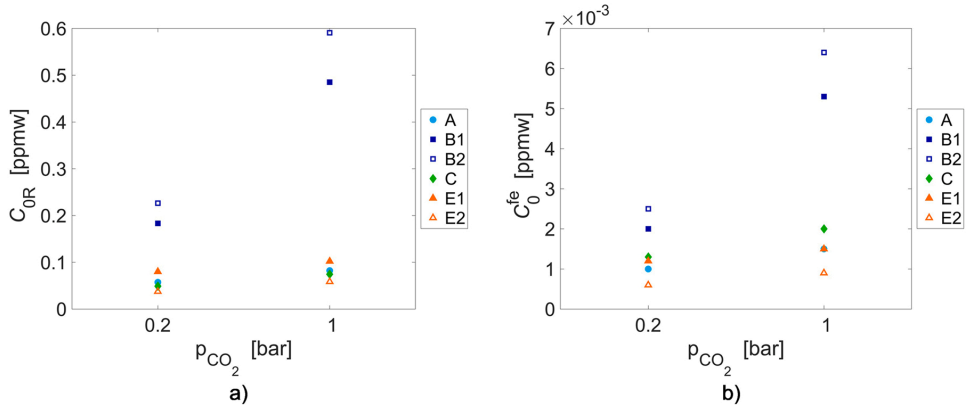

Fig. 9. Hydrogen uptakes estimated for the pure CO_2 period of the permeation tests, step 1 and 2 in Table 3. C_{0R} reflects both the lattice hydrogen and hydrogen in reversible traps whereas C_0^{fe} only describes the hydrogen in ferrite lattice.

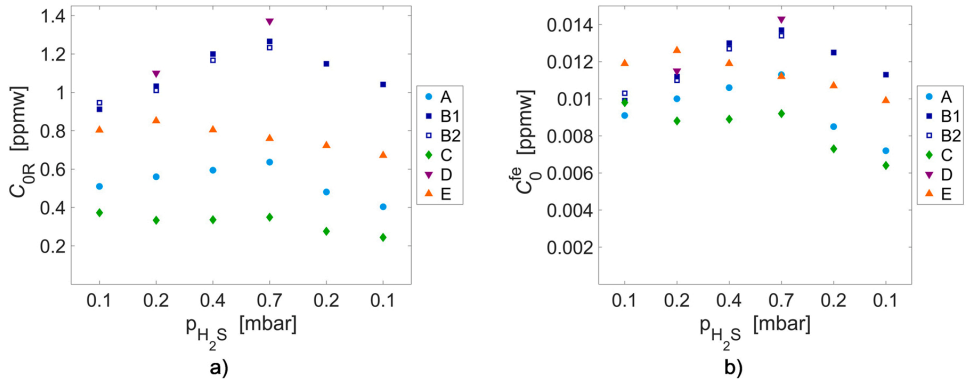

Fig. 10. Hydrogen uptakes estimated for the H_2S steps of the permeation test, step 3–8 in Table 3. C_{0R} reflects both the lattice hydrogen and hydrogen in reversible traps whereas C_0^{fe} only describes the hydrogen in lattice. The steps are placed in chronological order with the first exposure to H_2S placed to the left.

Table 7
Reversible hydrogen uptakes measured for uncorroded samples under cathodic polarization in previous work [31] and during step 6 of the permeation test (0.7 mbar H_2S).

Material	C_{0R} under cathodic polarization[a] [wt ppm]	C_{0R} during step 6[b] [wt ppm]
A	0.69	0.64
B	1.59	1.27
C	0.73	0.35
D	1.54	1.37
E	1.74	0.76

[a] 0.1 M NaOH, − 12 mA cm^{-2}, 25 °C.
[b] 0.7 mbar H_2S and 1 bar CO_2, 25 °C.

as observed by da Silva et al. [21].

4.3. Hydrogen uptake during H_2S exposure

H_2S is a hydrogen recombination poison [34,48,49] which can increase the hydrogen uptake in steels, while precipitation of FeS can both increase the hydrogen uptake by acting as a cathodic site [50] and decrease the hydrogen uptake by forming a barrier to hydrogen diffusion [25,26]. For all the materials, the hydrogen uptake decreased like a decay transient when the H_2S partial pressure was decreased in step 7 (0.2 mbar H_2S) and 8 (0.1 mbar H_2S), despite relatively stable corrosion rates, which indicates that the materials were subjected to a H_2S poison effect, even after the formation of S-containing corrosion products on the surfaces. The hydrogen recombination poison effect can also explain why the hydrogen uptakes increased when H_2S was added, despite decreased corrosion rates. A cathodic site effect may arise from the formation of mackinawite, which is expected to happen on the steel surface by reaction with the iron in metallic form [51], hence introducing new cathodic sites on the ferrite. This can give a shorter average path for hydrogen from adsorption site to ferrite matrix, compared to the path from retained carbides to ferrite matrix. However, cathodic reactions may still be occurring to a great extent on the retained carbides even during the H_2S exposure steps of the tests, especially if all the ferrite is covered with a thin FeS layer and the FeS layer has a high charge-transfer resistance. There are several indications of a barrier effect in the experiments: 1) Materials A, C and E had decreasing permeation fluxes after reaching a peak permeation flux in some of the H_2S exposure steps, 2) Materials C and E reached their highest hydrogen permeation flux before exposure to the highest H_2S partial pressure, and 3) Materials A, C, D and E had lower hydrogen permeation flux the second time the surfaces were exposed to 0.2 and 0.1 mbar H_2S compared to the first time, see Fig. 8. For Material A, C, D and E, there is

a relationship between film weight and C_{0R} during H_2S exposure. This relationship may be linked to the corrosion rate, where both the corrosion rate and film weight increases with the amount of retained carbides and the hydrogen uptake increases with the corrosion rate due to a higher amount of hydrogen being reduced at or near ferrite grains. It is also linked directly to the cementite, where the film weight increases with the amount of retained carbides on the surface and the hydrogen uptakes increase with the ferrite-cementite interfacial area due to trapping. Material B does however not follow this trend. Material B has the highest hydrogen uptake among the non-lamellar materials, both when considering only lattice hydrogen and hydrogen in reversible traps, despite having the lowest carbon content and film weight. If cathodic reactions are still occurring on the retained carbides, the same mechanism as proposed for CO_2 corrosion in Section 4.2 may be applicable for combined CO_2 and H_2S exposure. The behavior of materials A, C, D and E is consistent with the observations by Zhou et al. [27]. Under the condition of 1 MPa p_{CO2} and 0.001–0.1 MPa p_{H2S}, they found that the corrosion rate increased with the decrease of H_2S partial pressure and that the corrosion products changed from initially promoting hydrogen permeation to hindering the hydrogen permeation as the corrosion progressed. It is possible that this change from hydrogen promotion to hindrance would also be seen for Material B if the tests were conducted for longer times. Material B has a lower carbide fraction and corrosion rate than the other materials and might therefore need more time to form a well-covering FeS layer on the ferrite. This effect may be enhanced by lower adhesion between finely distributed carbides and steel surface, which keeps the ferrite fraction on the surface high through-out the CO_2 corrosion part of the test. Hence, more time may be needed for Material B to form the same barrier as the other materials, but this is questionable since the S content measured on the surfaces was not particularly low for Material B. There appears to be a trade-off between the positive and negative effects of retained carbides, where Material C has the best balance. Material B appears to have too little carbide, or too poorly connected carbide, to receive the beneficial effect of retained carbides. The materials with higher carbide contents than Material C also have higher hydrogen uptakes due to hydrogen trapping on carbide-cementite interfaces, possibly with contribution from higher corrosion rates.

5. Conclusion

Five steel armor wires were exposed to artificial seawater bubbled with N_2, CO_2 and H_2S in an electrochemical hydrogen permeation cell while the hydrogen permeation flux through the steels was measured. The electrolyte was continuously replaced to simulate an environment where protective iron carbonate film formation is not thermodynamically favorable.

- The hydrogen uptakes decreased with the accumulation of retained carbide for most of the materials, despite increasing corrosion rates. The carbide is primarily a site for cathodic reactions and the proposed mechanism for the reduced hydrogen uptakes with retained carbides is that the hydrogen adsorbed on retained carbides located far from ferrite grains will have limited opportunities for absorption into the steel since the hydrogen solubility and diffusivity in cementite is low.
- The positive effect of retained carbides was observed during pure CO_2 corrosion and when small amounts of H_2S (< 1 mbar H_2S) was introduced to the environment.
- The material with the lowest and most stable corrosion rate during CO_2 corrosion was one of the materials with highest hydrogen uptake. This material has the lowest carbon content and less continuous carbides than the other materials, and hence less retained carbides.
- Apart from this material, the results indicated higher hydrogen uptake with higher carbon content, probably due to the trapping of hydrogen on ferrite-cementite interfaces.
- Despite the reduction of hydrogen uptake with time observed for most of the materials, the hydrogen uptakes decreased substantially when the H_2S partial pressure was reduced towards the end of the tests, indicating a strong sensitivity to the H_2S poison effect even after the formation of hydrogen uptake barrier.

CRediT authorship contribution statement

Ellen Synnøve Skilbred: Conceptualization, Methodology, Investigation, Resources, Data curation, Writing – original draft, Visualization. **Simona Palencsár:** Conceptualization, Methodology, Validation, Investigation, Data curation, Writing – review & editing, Project administration. **Arne Dugstad:** Conceptualization, Methodology, Writing – review & editing, Supervision, Funding acquisition. **Roy Johnsen:** Conceptualization, Methodology, Writing – review & editing, Supervision, Funding acquisition.

Declaration of Competing Interest

The authors declare that they have no known competing financial interests or personal relationships that could have appeared to influence the work reported in this paper.

Data availability statement

The raw/processed data generated in this work are available upon request from the corresponding author.

Acknowledgements

This work was performed as part of the KPN project "Environmental Cracking of Flexible Pipe Armour Wires", Research Council of Norway project no. 280760 within the PETROMAKS 2 program. The authors would like to thank the following project participants for financial and technical support: The Research Council of Norway, Norway; Equinor, Norway; Shell, Norway; Chevron, United States of America; Petrobras, Brazil; OKEA, Norway; TechnipFMC, France; NOV, Denmark; Baker Hughes, United Kingdom; 4Subsea, Norway.

References

[1] T. Campos, J.A. Gomes, M. Seiersten, S. Palencsár, A. Dugstad, Corrosion of Armor Wire Steel in the Annulus of Flexible Pipes at Near Neutral pH, in: Corros. 2019, NACE International, Nashville, TN, 2019.
[2] A. Rubin, M.H. Haarh, S. Overby, T.S. Nielsen, J. Gudme, Corrosion Rates of Carbon Steel in Confined Environments. Corros. 2012, NACE International,, Salt Lake City, Utah, 2012, pp. 4002–4019.
[3] E. Remita, F. Ropital, J. Kittel, B. Tribollet, E. Sutter, C. Taravel-Condat, N. Desamais, Experimental and theoretical investigatoin of the uniform corrosion in the annulus of offshore flexible pipelines, in: Corros. 2008, New Orleans, Louisiana, 2008, pp. 4737–4753.
[4] W. Sun, S. Nešić, Kinetics of corrosion layer formation: part 1—iron carbonate layers in carbon dioxide corrosion, Corrosion 64 (2008) 334–346, https://doi.org/10.5006/1.3278477.
[5] S. Nešić, Key issues related to modelling of internal corrosion of oil and gas pipelines – A review, Corros. Sci. 49 (2007) 4308–4338, https://doi.org/10.1016/j.corsci.2007.06.006.
[6] S. Nesic, A. Stangeland, R. Nyborg, M. Nordsveen, A. Mechanistic Model for CO2 Corrosion with Protective Iron Carbonate Films, in: Corros. 2001, Houston, TX, 2001.
[7] L.L. Shreir, R.A. Cottis, Corrosion in liquids, corrosion evaluation, in: B. Cottis, M. Graham, R. Lindsay, S. Lyon, T. Richardson, D. Scantlebury, H. Scott (Eds.), Shreir's Corros, 4th ed..,, Elsevier, Amsterdam, 2010, pp. 725–1692.
[8] D. Burkle, R. De Motte, W. Taleb, A. Kleppe, T. Comyn, S.M. Vargas, A. Neville, R. Barker, In situ SR-XRD study of FeCO3 precipitation kinetics onto carbon steel in CO_2-containing environments: the influence of brine pH, Electrochim. Acta 255 (2017) 127–144, https://doi.org/10.1016/j.electacta.2017.09.138.
[9] D.A. López, W.H. Schreiner, S.R. de Sánchez, S.N. Simison, The influence of carbon steel microstructure on corrosion layers: an XPS and SEM characterization, Appl. Surf. Sci. 207 (2003) 69–85, https://doi.org/10.1016/S0169-4332(02)01218-7.
[10] C.A. Zapffe, C.E. Sims, Hydrogen Embrittlement, in: Internal Stress and Defects in Steel, Trans, 145, AIME, 1941, pp. 225–261.

[11] D.G. Westlake, A generalized model for hydrogen embrittlement, Trans. ASM 62 (1969) 1000–1006.

[12] M. Hatano, M. Fujinami, K. Arai, H. Fujii, M. Nagumo, Hydrogen embrittlement of austenitic stainless steels revealed by deformation microstructures and strain-induced creation of vacancies, Acta Mater. 67 (2014) 342–353, https://doi.org/10.1016/j.actamat.2013.12.039.

[13] C.D. Beachem, A new model for hydrogen-assisted cracking (hydrogen "embrittlement"), Metall. Mater. Trans. B 3 (1972) 441–455, https://doi.org/10.1007/BF02642048.

[14] H.K. Birnbaum, P. Sofronis, Hydrogen-enhanced localized plasticity—a mechanism for hydrogen-related fracture, Mater. Sci. Eng. A. 176 (1994) 191–202, https://doi.org/10.1016/0921-5093(94)90975-X.

[15] A.R. Troiano, The role of hydrogen and other interstitials in the mechanical behavior of metals (1959 Edward De Mille Campbell Memorial Lecture), Trans. Am. Soc. Met. 52 (1960) 54–80.

[16] R. Kirchheim, Revisiting hydrogen embrittlement models and hydrogen-induced homogeneous nucleation of dislocations, Scr. Mater. 62 (2010) 67–70, https://doi.org/10.1016/j.scriptamat.2009.09.037.

[17] P. Kedzierzawski, Hydrogen Trapping in Iron and Iron Alloys, in: R.A. Oriani, J. P. Hirth, M. Smialowski (Eds.), Hydrog. Degrad. Ferr. Alloy., 4th ed..,, William Andrew Publishing/Noyes, 1985, pp. 271–288.

[18] T.P. Radhakrishnan, L.L. Shreir, Permeation of hydrogen through steel by electrochemical transfer - I. Influence of catalytic poisons, Electrochim. Acta 11 (1966) 1007–1021.

[19] F. Farelas, M. Galicia, B. Brown, S. Nesic, H. Castaneda, Evolution of dissolution processes at the interface of carbon steel corroding in a CO_2 environment studied by EIS, Corros. Sci. 52 (2010) 509–517, https://doi.org/10.1016/j.corsci.2009.10.007.

[20] A. Dugstad, Mechanism of Protective Film Formation During CO_2 Corrosion of Carbon Steel, in: Corros. 1998, NACE International, 1998.

[21] S.C. da Silva, E.A. de Souza, F. Pessu, Y. Hua, R. Barker, A. Neville, J.A. da Cunha Ponciano Gomes, Cracking mechanism in API 5L X65 steel in a CO_2-saturated environment, Eng. Fail. Anal. 99 (2019) 273–291, https://doi.org/10.1016/j.engfailanal.2019.02.031.

[22] D.N. Staicopolus, The role of cementite in the acidic corrosion of steel, J. Electrochem. Soc. 110 (1963) 1121, https://doi.org/10.1149/1.2425602.

[23] J.L. Crolet, N. Thevenot, S. Nesic, Role of conductive corrosion products in the protectiveness of corrosion layers, Corrosion 54 (1998).

[24] C. Plennevaux, J. Kittel, M. Frégonèse, B. Normand, F. Ropital, F. Grosjean, T. Cassagne, Contribution of CO_2 on hydrogen evolution and hydrogen permeation in low alloy steels exposed to H2S environment, Electrochem. Commun. 26 (2013) 17–20, https://doi.org/10.1016/j.elecom.2012.10.010.

[25] E. Wallaert, T. Depover, I. De Graeve, K. Verbeken, FeS corrosion products formation and hydrogen uptake in a sour environment for quenched & tempered steel, Met 8 (2018), https://doi.org/10.3390/met8010062.

[26] F. Huang, P. Cheng, X.Y. Zhao, J. Liu, Q. Hu, Y.F. Cheng, Effect of sulfide films formed on X65 steel surface on hydrogen permeation in H2S environments, Int. J. Hydrog. Energy 42 (2017) 4561–4570, https://doi.org/10.1016/j.ijhydene.2016.10.130.

[27] C. Zhou, B. Fang, J. Wang, S. Hu, B. Ye, Y. He, J. Zheng, L. Zhang, Effect of interaction between corrosion film and H2S/CO_2 partial pressure ratio on the hydrogen permeation in X80 pipeline steel, Corros. Eng. Sci. Technol. 55 (2020) 392–399, https://doi.org/10.1080/1478422X.2020.1737384.

[28] A. Dugstad, S. Palencsár, G. Svenningsen, J. Muren, M. Eriksen, B. Thoppil, J. Melville, K. Sanghavi, The Combined Effect of O2 and CO2 on Corrosion of Flexible Armour Wires, in: Corros. 2020, 2020: p. NACE-2020–14790.

[29] A. Dugstad, S. Palencsár, T. Berntsen, L. Børvik, Corrosion of steel armour wires in flexible pipes - history effects (Aberdeen, Scotland, UK), SPE Int. Oilf. Corros. Conf. Exhib. (2018) 1–16, https://doi.org/10.2118/190907-MS.

[30] M.A.V. Devanathan, Z. Stachurski, The adsorption and diffusion of electrolytic hydrogen in palladium, Proc. R. Soc. Lond. A. Math. Phys. Sci. 270 (1962) 90–102. ⟨http://www.jstor.org/stable/2416199⟩.

[31] E.S. Skilbred, M. Kappes, M. Iannuzzi, R. Johnsen, Hydrogen uptake and diffusivity in steel armor wires with different chemical composition, carbide distribution, grain size, and degree of deformation, Mater. Corros. (2021) 1–20, https://doi.org/10.1002/maco.202112615.

[32] American Petroleum Institute, API Specification 17J: Specification for Unbonded Flexible Pipe, 4th edition, 2014.

[33] NACE Standard TM0198 Slow Strain Rate Test Method for Screening Corrosion-Resistant Alloys for Stress Corrosion Cracking in Sour Oilfield Service, (2016).

[34] ASTM G148 Standard Practice for Evaluation of Hydrogen Uptake, Permeation, and Transport in Metals by an Electrochemical Technique, (2018).

[35] ISO 17081. Method of measurement of hydrogen permeation and determination of hydrogen uptake and transport in metals by an electrochemical technique, (2014).

[36] P. Bruzzoni, Efectos de superficie en la difusión de hidrógeno en hierro y aleaciones ferrosas, Universidad de Buenos Aires, 2003.

[37] H. Husby, M. Iannuzzi, R. Johnsen, M. Kappes, A. Barnoush, Effect of nickel on hydrogen permeation in ferritic/pearlitic low alloy steels, Int. J. Hydrog. Energy 43 (2018) 3845–3861, https://doi.org/10.1016/j.ijhydene.2017.12.174.

[38] D. Johnson, G. Krauss, Correlation of microstructural parameters and hydrogen permeation in carbon steel, Metall. Trans. A. 18 A (1987) 717–721.

[39] W.C. Luu, J.K. Wu, The influence of microstructure on hydrogen transport in carbon steels, Corros. Sci. 38 (1996) 239–245, https://doi.org/10.1016/0010-938X(96)00109-6.

[40] G.M. Pressouyre, Hydrogen traps, repellers, and obstacles in steel; Consequences on hydrogen diffusion, solubility, and embrittlement, Metall. Trans. A. 14 (1983) 2189–2193, https://doi.org/10.1007/BF02662391.

[41] K. Kiuchi, R.B. McLellan, The solubility and diffusivity of hydrogen in well-annealed and deformed iron, Acta Met. 31 (1983) 961–984, https://doi.org/10.1016/0001-6160(83)90192-X.

[42] C. Forot, E. Legrand, E. Roguet, J. Creus, J. Kittel, X. Feaugas, Impact of cementite tortuosity on hydrogen diffusion in pearlitic steels, in: Eurocorr 2015, Graz, Austria, 2015, pp. 107–114. ⟨https://hal-ifp.archives-ouvertes.fr/hal-02464473⟩.

[43] A. Turnbull, R.B. Hutchings, Analysis of hydrogen atom transport in a two-phase alloy, Mater. Sci. Eng. A. 177 (1994) 161–171, https://doi.org/10.1016/0921-5093(94)90488-X.

[44] F. Thebault, S. Frappart, L. Delattre, H. Marchebois, J. Creus, X. Feaugas, Hydrogen Diffusion In a Model Molybdenum Containing Steel: A Comparison Between Hydrogen Ingress Promoted By H2S Or Cathodic Charging, in: Corros. 2011, NACE International, Houston, Texas, 2011, p. 11104 (NACE).

[45] D. Rickard, G.W. Luther, Chemistry of iron sulfides, Chem. Rev. 107 (2007) 514–562, https://doi.org/10.1021/cr0503658.

[46] K.-L. Lee, S. Nesic, The Effect of Trace Amount of H2S on CO_2 Corrosion Investigated by Using the EIS Technique, in: Corros. 2005, 2005, p. 05630 (NACE).

[47] L. Tau, S.L.I. Chan, Effects of ferrite/pearlite alignment on the hydrogen permeation in a AISI 4130 steel, Mater. Lett. 29 (1996) 143–147, https://doi.org/10.1016/S0167-577X(96)00140-1.

[48] K.A. Esaklul, 13 - Hydrogen damage, in: A.M.B.T.-T. in O. and G.C. R. and T. El-Sherik (Ed.). Woodhead Publ. Ser. Energy, Woodhead Publishing,, Boston, 2017, pp. 315–340, https://doi.org/10.1016/B978-0-08-101105-8.00013-9.

[49] X. Wen, P. Bai, B. Luo, S. Zheng, C. Chen, Review of recent progress in the study of corrosion products of steels in a hydrogen sulphide environment, Corros. Sci. 139 (2018) 124–140, https://doi.org/10.1016/j.corsci.2018.05.002.

[50] P. Bai, Y. Liang, S. Zheng, C. Chen, Effect of amorphous FeS semiconductor on the corrosion behavior of pipe steel in H2S-containing environments, Ind. Eng. Chem. Res. 55 (2016) 10932–10940, https://doi.org/10.1021/acs.iecr.6b03000.

[51] W. Sun, S. Nesic, A. Mechanistic, Model Of H2S corrosion of mild steel, Corros. 2007, Athens, Ohio (2007) 07655 (Paper No.).

Paper III

E.S. Skilbred, A.O. Myhre, L.M. Viespoli, A. Alvaro, R. Johnsen

Correlation between microstructure and hydrogen embrittlement susceptibility of flexible pipe steel armor wires measured by slow strain rate testing of notched samples

To be submitted

Paper IV

E.S. Skilbred, S.A. Lootz, R. Johnsen

Hydrogen embrittlement susceptibility of steel armor wires for flexible pipes

CORROSION 2020, June 14-18, physical event cancelled but the paper was published, paper no. C2020-14489

ISBN 978-82-326-6609-6 (printed ver.)
ISBN 978-82-326-6279-1 (electronic ver.)
ISSN 1503-8181 (printed ver.)
ISSN 2703-8084 (online ver.)

NTNU
Norwegian University of
Science and Technology